Dissertationsschrift

InP/(Al,Ga)InP Quantum Dots on GaAs- and Si-Substrates for Single-Photon Generation at Elevated Temperatures

Von der Fakultät Mathematik und Physik der Universität Stuttgart zur Erlangung der Würde eines Doktors der Naturwissenschaften (Dr. rer. nat.) genehmigte Abhandlung

Vorgelegt von
Dipl.-Phys. Moritz Bommer
geboren in Stuttgart

Hauptberichter: Prof. Dr. P. Michler
Mitberichter: Prof. Dr. H. Schweizer

Tag der mündlichen Prüfung: 12. September 2012

Institut für Halbleiteroptik und Funktionelle Grenzflächen (IHFG)
Universität Stuttgart

2013

I would like to thank my family,

my colleges,

and all my friends…

Selbstständigkeitserklärung

Hiermit erkläre ich, die vorliegende Arbeit selbstständig und ohne fremde Hilfe verfasst bzw. nur die angegebenen Literaturquellen und Hilfsmittel verwendet zu haben.

Ich habe mich anderwärts nicht um einen Doktorgrad beworben und besitze einen entsprechenden Titel nicht.

Ich erkläre die Kenntnisnahme der dem Verfahren zugrundeliegenden Promotionsordnung der Fakultät 8 (Mathematik und Physik) der Universität Stuttgart.

Stuttgart, den 11. Juli 2013

Moritz Bommer

Abstract

> Religion is an insult to human dignity. Without it you would have good people doing good things and evil people doing evil things. But for good people to do evil things, that takes religion.
>
> *(Steven Weinberg 1999)*

This work concentrates on optical investigation on single-photon generation for applications in communications, quantum cryptography, and quantum computing. Single-photon sources for commercial devices require robustness in their working conditions, e.g. temperature, pressure, etc. as well as high output rates and emission directionality. From the many possibilities of generating single-photons like single-atoms, parametric down-conversion, nitrogen vacancy centers in diamond etc., InP quantum dots have been chosen for detailed analysis in this thesis.

The InP and InAs quantum dots discussed in this work, are epitaxially fabricated by MOVPE in the STRANSKI-KRASTANOV growth-mode. In order to access a single quantum dot, different approaches of processing and pre-processing like shadow masks, mesas, micro-pillars, and site-controlled growth are employed.

The quantum dots have been fabricated on different substrates, namely miscut and exactly oriented GaAs, Si, and Ge virtual substrate on Si. The latter two might allow complementary metal oxide semiconductor (CMOS)-compatibility, which is of high interest because it allows the integration of optical elements into

the commercially well established Si based environment. Here, the influence of different substrates on the single-photon emission properties of quantum dots has been investigated.

For detailed analysis of the fabricated samples, various measurement techniques like X-ray diffraction, secondary ion mass spectrometry, scanning electron microscopy, atomic-force microscopy, photoluminescence spectroscopy on single quantum dots and ensembles of quantum dots, TCSPC, and photon statistics measurements were utilized. The main focus of this work lies on the latter, optical measurements of single quantum dots.

Extending the temperature range for InP quantum dots based single-photon sources from the current maximum temperature of 80 K towards the regime of Peltier-cooling ($\geq 150\,\mathrm{K}$) is very desirable, because it reduces the footprint of a device and its servicing costs drastically. In this work, an enhancement of the working temperature up to 110 K, with $g^{(2)}_{\mathrm{deconv.}}(\tau = 0) = 0.41$, has been shown.

Therefore, detailed temperature dependent studies on the physics of single-photon generation have been performed. The thermal activation of charge carriers into the barrier, limiting their working temperature and especially, the spectral linewidth broadening by temperature, with respect to the biexciton binding energy, has been investigated in detail.

The results of these studies have been used to build a model of the exciton-biexciton-system. The model extrapolates the temperatures of the system up to 200 K. Out of this model, the influence of a spectral biexciton-exciton-overlap and the exciton dark-state on single-photon generation has been investigated.

Übersicht

Diese Arbeit widmet sich optischen Untersuchungen zur Einzelphotonenerzeugung hinsichlich deren Anwendung im Bereich Kommunikation, Quantenkryptographie und Quantencomputing. Einzelphotonenquellen für kommerzielle Geräte erfordern einerseits Stabilität gegenüber ihren Arbeitsumgebungsparametern, wie z.B. Temperatur, Druck etc., sowie andererseits hohe Photonenerzeugungsraten und eine gerichtete Abstrahlung. Von den vielen Möglichkeiten zur Erzeugung von Einzelphotonen, wie z.B. mit einzelnen Atomen, Parametrischer Fluoreszenz, Stickstoff-Fehlstellen-Zentren in Diamanten etc., wurden InP Quantenpunkte für eine detaillierte Untersuchung in dieser Arbeit gewählt.

Die InP und InAs Quantenpunkte, die in dieser Arbeit behandelt werden, sind mit Metallorganischer Gasphasenepitaxie im Stranski-Krastanov Wachstumsmodus hergestellt worden. Um Messungen an einzelnen Quantenpunkten ausführen zu können, wurden mehrere Ansätze der Vor- und Nachprozessierung wie Schattenmasken, Mesen, Mikroresonatoren und positioniertes Quantenpunktwachstum ausgenutzt.

Die Quantenpunkte wurden auf verschiedenen Substraten hergestellt, nämlich exakt- und fehl-orientiertes GaAs, Si und virtuellem Germanium Substrat auf Si. Die beiden Letzten könnten CMOS Kompatibilität erlauben, was von hohem Interesse ist, ermöglicht es doch die Integration von optischen Elementen innerhalb des kommerziell etablierten Si-basierten Umfelds. Hierbei wurde der Einfluss der verschieden Substrate auf die optischen Eigenschaften

der von Quantenpunkten erzeugten Einzelphotonen untersucht.

Zur detaillierten Analyse der hergestellten Proben wurden verschiedenste Techniken angewandt wie Röntgenbeugung, Sekundärionen-Massenspektrometrie, Rasterkraftmikroskopie, Elektronenmikroskopie, Photolumineszenzspektroskopie von einzelnen Quantenpunkten und Quantenpunkt Ensembles, sowie TCSPC und Photonenstatistikmessungen. Der Hauptfokus dieser Arbeit liegt auf den Letztgenannten, den optischen Messungen an einzelnen Quantenpunkten.

Die Ausweitung des Arbeitsbereiches InP Quantenpunkt basierter Einzelphotonenquellen, von den bisher erreichten 80 K in einen Temperaturbereich der PELTIER-Kühlung ($\geq 150\,\mathrm{K}$), ist sehr erstrebenswert, da sie die Größe und die Unterhaltungskosten eines solchen Gerätes erheblich reduziert. In dieser Arbeit konnte eine Erhöhung der maximalen Arbeitstemperatur bis hin zu 110 K bei $g^{(2)}_{\mathrm{deconv.}}(\tau = 0) = 0.41$ erzielt werden.

Dazu wurden detaillierte temperaturabhängige Untersuchungen zur Einzelphotonenerzeugung durchgeführt. Die Aktivierungsenergien für Ladungsträger in das Barrierematerial, die die Temperaturstabilität bestimmen, sowie besonders die spektrale Verbreiterung der Lumineszenzlinien in Abhängigkeit der Biexzitonenbindungsenergie wurden detailliert untersucht.

Die Ergebnisse dieser Untersuchungen wurden als Basis für die Entwicklung eines Exziton-Biexziton-Modells verwendet. Das Modell bietet die Möglichkeit, das Temperaturverhalten bis 200 K zu extrapolieren und den Einfluss des spektralen Biexziton-Exziton-Überlapps auf die Qualität der Einzelphotonenerzeugung zu untersuchen.

Contents

Abstract 1

Abstract (german) 3

Acronyms 11

Physical Constants and Symbols 15

Materials 17

1. Introduction 19

2. Physical Background 23

2.1. Semiconductors 23
2.2. Low Dimensional Systems 24
2.3. Excitation 27
2.4. State Population 29
2.4.1. Exciton: Bright State – Dark State 30
2.4.2. Biexciton 33
2.4.3. Charged States 33
2.4.4. Higher Shells 34
2.5. Photon Statistics 34
2.5.1. Harmonic Oscillator Model of Light 35
2.5.2. Thermal Light 35
2.5.3. Coherent Light 36

2.5.4. Non-Classical Light 38
2.5.5. Verification of Light States 39
2.6. Cavity QED 41
2.6.1. Micro-Pillars 41
2.7. Excitation Power Dependence 43
2.7.1. Exciton–Biexciton Dynamics 44
2.7.2. Higher Shells 45
2.7.3. Red- and Blue-shift 46
2.8. Temperature Dependence 46
2.8.1. Bandgap Shift 46
2.8.2. Cavity Shift 48
2.8.3. Dark State Dynamics 48
2.8.4. Blue-shift 49
2.8.5. Spectral Linewidth Broadening 49
2.8.6. Dark State 50
2.8.7. PL Intensity 50

3. Experimental **53**
3.1. Materials 53
3.1.1. CMOS Compatibility 53
3.1.2. Wafer Materials 54
3.2. Sample Fabrication 55
3.2.1. Epitaxial Growth Techniques 55
3.2.2. GaAs Buffer 57
3.2.3. Barrier Material 57
3.2.4. Quantum dot fabrication 58
3.3. Gaining Access to a Single QD 60
3.3.1. Post-Processing of Samples 61
3.3.2. Pre-Processing of Samples 63
3.3.3. In-Situ Quantum dot density reduction . . 64
3.4. Experimental Techniques 65
3.4.1. µ-Photoluminescence Setup 65

3.4.2. HBT Setup 67
3.4.3. TCSPC Setup 69

4. InP QDs on GaAs/GaAs Substrate 71
4.1. Micro Pillars 71
4.1.1. Mode investigations 73
4.1.2. Single-Photon Emission 74
4.1.3. Conclusion 82
4.2. Reduced Density Sample 83
4.2.1. Linewidth 86
4.2.2. Time Resolved Measurements 87
4.2.3. Conclusion 90
4.3. Site-controlled InP Nucleation 91
4.4. Conclusion of the GaAs based samples 93

5. InP QDs on GaAs/Si Substrate 95
5.1. InAs QD-Strain-Layer 95
5.1.1. Power Dependent Measurements 96
5.1.2. Temperature Dependent Measurements . . . 96
5.1.3. Time Resolved Measurements 99
5.1.4. Conclusion 99
5.2. InGaAs/GaAs Super-Lattice 100
5.2.1. Power Dependent Measurements 101
5.2.2. Temperature Dependent Measurements . . . 103
5.2.3. Time Resolved Measurements 105
5.2.4. Conclusion 108

6. InP QDs on GaAs/GeVS/Si Substrate 111
6.1. Power Dependent Measurements 112
6.2. Temperature Dependent Measurements 114
6.2.1. Time Resolved Measurements 115
6.3. Conclusion 117

7. InP QDs on GaAs/GaP/Si Substrate 119
7.1. Power Dependent Measurements 120
7.2. Temperature Dependent Measurements 122
7.2.1. Linewidth 123
7.3. Excitation Wavelength Dependent Measurements . 124
7.4. Photon Statistics Measurements 126
7.5. Conclusion 127

8. Comparison of Material Systems and Techniques 129
8.1. Comparison of Sample Processes 129
8.2. Refilling 135
8.3. Outlook 135

9. Modeling of Single-Photon Purity and Efficiency 137
9.1. Modeling the carrier generation 138
9.2. Obtaining of System Parameters 139
9.2.1. Spectral Position 139
9.2.2. Linewidth 139
9.2.3. Temperature Induced Red-shift 139
9.2.4. Dark State Dynamics 139
9.2.5. Thermal Quenching 140
9.2.6. Spectral Region of Interest 140
9.3. Flowchart of the model 141
9.4. Modeled Quantities 143
9.4.1. Photon Emission Probability Into the ROI 143
9.4.2. Purity of Single-Photon Emission 143
9.4.3. Single-Photon Efficiency 144
9.5. Results 144
9.5.1. Calculations Without Thermal Quenching . 144
9.5.2. Calculations With Thermal Quenching . . . 146
9.6. Conclusion & Outlook for the Model 149

10. Summary & Outlook 151

Summary & Outlook (german) 155

A. Created Software 159
A.1. LabVIEW 159
A.1.1. DotHunter 159
A.1.2. PeakFinder 161
A.2. Octave 162
A.2.1. PeakSim 163

List of Figures 171

Glossary 175

Own Publications 177

Bibliography 179

Acronyms

Notation	Description
ACO	autocorrelation.
AFM	atomic-force microscope.
AOTF	acoustic optical tunable filter.
APB	anti-phase boundary.
APD	anti-phase domain.
ASPD	avalanche single-photon detector.
BS	bright exciton state.
CB	conduction band.
CCD	charge-coupled device.
CMOS	complementary metal oxide semiconductor.
CW	continuous-wave.
DBR	distributed BRAGG-reflector.
DH	DotHunter.
DOS	density of states.
DS	dark exciton state.
e–h pair	electron–hole pair.
EPD	excitation power density.

Notation	Description
FIB	focused ion beam.
FWHM	full-width at half-maximum.
HBT	Hanbury Brown and Twiss setup.
IR	infrared.
LA	longitudinal acoustic.
LED	light emitting diode.
LO	longitudinal optical.
MBE	molecular beam epitaxy.
MCB	multi-channel buffer.
µ-PL	micro-photoluminescence.
MOVPE	metal-organic vapor-phase epitaxy.
MP	micro-pillar.
NA	numerical aperture.
NIR	near infrared.
NV	nitrogen vacancy.
PDC	parametric down-conversion.
PF	PeakFinder.
PL	photoluminescence.
QD	quantum dot.
ROI	region of interest.
SEM	scanning electron microscope.

Notation	Description
SIMS	secondary ion mass spectrometry.
SK	Stranski-Krastanov.
SL	super lattice.
SP	single-photon.
SPS	single-photon source.
T^+	positively charged trion.
T^-	negatively charged trion.
TA	transversal acoustic.
TAC	time-to-amplitude converter.
TCSPC	time-correlated single-photon counting.
TO	transverse optical.
VB	valence band.
VI	Virtual Instrument.
WD	working distance.
WL	wetting layer.
X	exciton.
XX	biexciton.

Physical Constants and Symbols

Notation	Description
a_B	BOHR radius.
E_G	band gap energy.
E	Energy.
e	EULER's constant: 2.718 281 8.
$E_\mathrm{bind}^\mathrm{XX}$	XX binding energy.
E_flip	BS–DS splitting energy.
$\epsilon_\mathrm{0,r}$	electrical permittivities.
$g^{(2)}(\tau)$	second-order correlation function.
Γ	spectral linewidth FWHM.
$\hbar$	PLANK constant, divided by 2π: $6.582\,118\,9 \times 10^{-16}$ eVs.
k_B	BOLTZMANN constant: $8.617\,342\,2 \times 10^{-5}$ eV/K.
$m^\star$	effective mass.
μ^*	effective exciton mass.

Notation	Description
π	ratio of circumference of circle to its diameter: 3.1415927.
σ_{int}	interface energy.
σ_{sub}	surface energy of the substrate.
σ_{sur}	surface energy.
$\uparrow$ / $\downarrow$	electron spin up / down.
$\Uparrow$ / $\Downarrow$	hole spin up / down.
T	temperature.
$t_{1,2}$	decay time (1 = fast, 2 = slow).
τ	delay time.
$T_{\text{max}}^{g^{(2)}}$	highest temperature with $g^{(2)}(\tau = 0) < 0.5$ (max. single-photon temperature).

Materials

Notation	Description
Al	aluminum.
AlGaInP	aluminum gallium indium phosphide, a III/V semiconductor used as barrier material for InP-QDs within this work.
AlN	aluminum nitrite, a II/VI semiconductor mainly used as barrier material for QDs.
As	arsenic.
Ga	gallium.
GaAs	gallium arsenide, a III/V semiconductor used as wafer material and for buffer layers.
GaInP	gallium indium phosphide, a III/V semiconductor mainly used as barrier material for InP-QDs.
GaN	gallium nitrite, a II/VI semiconductor.
GaP	gallium phosphide, used as an intermediate layer to prevent anti-phase domain (APD) formation within this work.
Ge	germanium.
GeVS	germanium virtual substrate.

Notation	Description
InAs	indium arsenide, a III/V semiconductor meterial used for QDs.
InGaAs	indium gallium arsenide, a III/V semiconductor meterial used for super-lattices within this work.
InP	indium phosphide, used as QD material within this work.
Si	silicon.

1. Introduction

> Den Rest meines Lebens möchte ich damit zubringen, darüber nachzudenken, was Licht ist.
>
> *(Albert Einstein 1879–1955)*

In our world, information becomes the most worthy object. Reducing information to its essentials is one of the most important tasks for humanity. Reducing the information carrier to its vital portion — a single quantum — opens up a door to possibilities of calculus [1] and cryptography [2,3] which are way beyond the classical means [4–9].

The generation of single or indistinguishable and entangled photons which can be obtained from quantum dots (QDs) in various ways [10–18] gives way to highly efficient algorithms e.g. prime factorization in polynomial instead of super-polynomial time [19], which, in this case, allows fast decryption of state-of-the-art cryptographic keys. Encoding information on a quantum system allows manipulation and interaction in the scope of quantum mechanics and therefore the implementation of protocols for highly secure communication [20–22]. The *SwissQuantum* quantum key distribution network nicely shows the long term stability and maturity of a real-world quantum cryptography network. It was installed near to Geneva and used by end-users since end of March 2009 to the beginning of January 2011 [23].

Nowadays, most electronic devices are based on silicon wafers, which are cheap, large and of high quality. Optical inter- and

intra-communication in electronic devices or pure optical functionality is highly desirable [24–26]. While Si-based photon detection devices are already developed [27–29], Si is disadvantageous for light emitting applications, due to its indirect band gap [30, 31]. The integration of well established optical technologies and materials, like III-V semiconductors, on Si-wafers in a CMOS-compatible way, is a promising approach to fabricate efficient light emitting structures [32–38]. To overcome the problem of the large lattice mismatch of 4% between the Si-matrix and the gallium arsenide (GaAs)-matrix and the therefore arising problems with crystal defects, several approaches have been investigated within this work. Approaches to build up the interface region between industrially used CMOS-compatible Si(001)-wafers and GaAs buffer layers by intermediate (Si/Ge) [39, 40] or gallium phosphide (GaP) layers [41, 42] have been investigated in this work. The main focus of the performed experiments lies on studies regarding the influence of the different structures on the optical properties of single InP-QD luminescence, especially exciton (X) recombination times, spectral linewidth and refilling effects arising from charge carrier traps and from the dark exciton state (DS).

Another important aspect for light emitting structures within commercial devices, especially single-photon (SP) sources, is the ability to work at elevated temperatures desirably in the regime of Peltier-cooling above 150 K. Actually, the maximum temperature for indium phosphide (InP)-QD single-photon emission is 100 K optically pumped [43] and 80 K, electrically pumped [44]. Other material systems allow higher working temperatures like CdSe/Zn(S,Se)-QDs [45, 46] (up to 200 K and 220 K), CdSe/-ZnSSe/MgS-QDs [47, 48] (300 K) or GaN/AlN-QDs [49] (200 K), and InGaAs/GaAs-QDs (135 K) [50], InAs/AlGaAs-QDs [51], but in different spectral regions. In order to investigate the temperature limits of InP-QDs, several system parameters as the spectral

linewidth, the biexciton (XX) binding energy, bright-dark-state splitting, and activation energies have been analyzed in detail.

The obtained parameters from the various measurements are further used to develop a numerical model. In this model the influence on the biexciton luminescence on the spectral region of the exciton luminescence is investigated to estimate the efficiency and purity of a InP-QD based SP source towards elevated temperatures.

The chapters this thesis is subdivided in, describe the fundamental theoretical background and the experimental techniques as well as the sample fabrication and preparation processes. The various measurements on single-QD luminescence are further separated in several chapters for each of the different sample structures, namely the GaAs substrate with different pre-/post- and in-situ processing steps. Further, several chapters for structures based on Si with different buffer and strained layers are discussed.

In the end, the main results of the different material systems are compared and the quality and efficiency of the SP generation process is numerically modeled. Finally, the whole work is summarized.

2. Physical Background

The following sections will provide the reader with the most essential knowledge, necessary to understand the applied experimental techniques and analysis methods. Furthermore it is also the basis for the conclusions made in this dissertation.

2.1. Semiconductors

Matter can roughly be classified into three groups, namely conductors, semiconductors, and insulators. Within a conductor, the valence electrons can be seen as a gas, not pinned to the atoms in the material and are therefore free to move. Insulators accommodate electrons which are strongly bound to the atoms and are therefore unable to propagate which makes the material electrically insulating.

In between, electrons in semiconductors are relatively easy excited from their lattice sites, located in the valence band (VB), into the conduction band (CB), leaving a hole behind. Both of this carriers, the electron and the hole, latter is seen as a quasiparticle, are now free to propagate within the system which leads to a transition from insulating to conductive material. The CB and VB are energetically separated by the valence-conduction band gap, which plays a central role in semiconductor physics [52]. Utilizing semiconductor materials with different band gap energies allow the fabrication of structures having a lower band gap within a material

owning a higher band gap, which results in designable potential landscapes for carriers, with a manifold of new properties [4, 53].

2.2. Low Dimensional Systems

Up to now, the properties of large volumes of material have been discussed. If now one reduces one or more dimension down to a length scale in the order of the electron and hole wave function (index e,h), which is given by their DE BROGLIE wavelength $\lambda_{\mathrm{e,h}}$

$$\lambda_{\mathrm{e,h}} = \frac{2\pi\hbar}{\sqrt{3m^{\star}_{\mathrm{e,h}} k_{\mathrm{B}} T}} \tag{2.1}$$

with k_{B} the BOLTZMANN constant, $m^{\star}$ the effective mass, $\hbar$ the PLANK constant divided by 2π and T the temperature, or down do scales of the BOHR-radius a^{*}_{B} of a bound electron–hole pair (e–h pair), called X

$$a^{*}_{\mathrm{B}} = \frac{4\pi\epsilon_0\epsilon_{\mathrm{r}}\hbar^2}{\mu^{*} e^2} \tag{2.2}$$

with $\epsilon_{0,\mathrm{r}}$ the electrical permittivities and μ^{*} the effective mass of the X, the density of states (DOS) for this particles (see Fig. 2.1) changes significantly [53].

Quantum well The reduction of one spatial dimension down to sizes mentioned above, leads to a so called quantum well. This structures are often used as active material for light emitting diodes (LEDs) or lasers [54–56]. See Fig. 2.1b.

Quantum wire Further reduction of a second dimension leaves an one dimensional carrier confinement potential behind, which has an even lower DOS and allows confined carriers to just move along the quantum wire axis. See Fig. 2.1c.

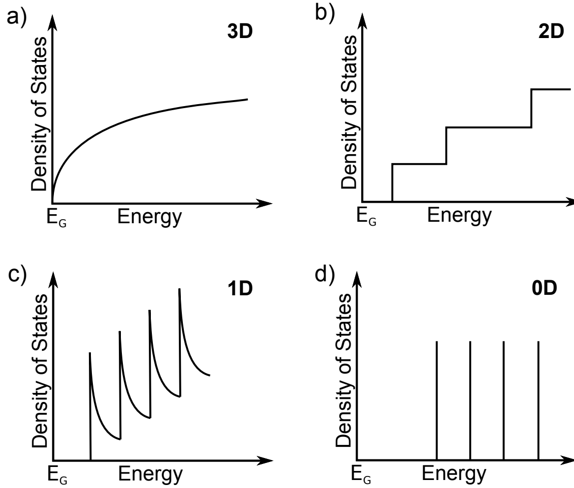

Figure 2.1.: Density of states for different dimensions. **a)** three dimensional, **b)** two dimensional, **c)** one dimensional, and **d)** zero dimensional. E_G denotes the energy of the band gap.

Quantum dot Finally one can build up a system where the electron wave function is confined in all three spatial dimensions by a carrier confinement potential, this "zero dimensionality" results in a delta like DOS. Such a system is called a QD and its states are similar to that of an atom, therefore QDs are often referred to as "artificial atoms". See Fig. 2.1d.

Because the QD is lens-shaped due to its fabrication process, the confinement in the growth direction (z-direction) is much stronger. Therefore, the calculation of states inside the QD can be accomplished by assuming a two-dimensional harmonic confinement potential in the x-y-plane, with leads to the following

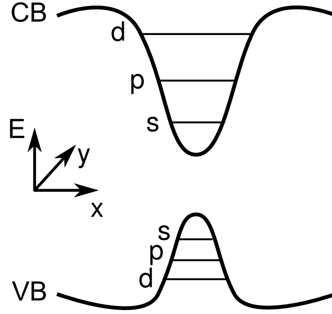

Figure 2.2.: Schematic shell structure of a QD with a harmonic carrier confinement potential with conduction band (CB) and valence band (VB).

two-dimensional single-particle Hamiltonian

$$\hat{H} = -\frac{\hbar^2 \nabla^2_{x,y}}{2m^\star} + \frac{1}{2} m^\star \omega_0^2 (x^2 + y^2) \tag{2.3}$$

this results in eigenstates which are closely related to those in atom physics:

$$E_{n,l} = \hbar\omega_0 (2n + |l| + 1) \tag{2.4}$$

with $n = \{0, 1, 2, \dots\}$ and $l = \{0, \pm 1, \pm 2, \dots\}$ the radial and azimuthal quantum numbers, respectively, one can define a *state index* $s = 2n + |l|$ [57]. In correspondence to atom physics the values of s are assigned to letters in the following way:

$$0 \rightarrow \mathrm{S}, \quad 1 \rightarrow \mathrm{P}, \quad 2 \rightarrow \mathrm{D}, \quad 3 \rightarrow \mathrm{F}.$$

The heavy- and light-hole states are split in energy by at least several tens of meV, due to the strain in self-assembled quantum dots. The spin of the energetically preferred *heavy hole* is $j_{\mathrm{h},z} = \pm\frac{3}{2}$, while the electron spin is still $s_{\mathrm{e},z} = \pm\frac{1}{2}$.

2.3. Excitation

Luminescence by thermal activation is extremely low, therefore carriers have to be excited in a different way, in order to have distinct luminescence. In the following sections some ways of excitation are described.

Above band excitation Photons with energies above the band gap energy of the barrier material, surrounding the QD, are absorbed by creating e–h pairs in the barrier of the QD. These charge carriers fast relax from the CB of the barrier energetically down into the wetting layer (WL) and further down the higher shells of the QD into the lowest possible state. This relaxation process has the consequence that electron and hole suffer from dephasing and may perform spin flips, which leads to a stochastical population of the lowest state regarding spin and phase [58]. See Fig. 2.3 (Arrow 1).

Wetting layer excitation The lowest possible photon energy for this excitation method corresponds to the WL band gap. Here the e–h pairs are created in the direct vicinity of the QD and can then relax into the QD. The efficiency of this approach is lower due to the lower probability of photon absorption in the thin WL. See Fig. 2.3 (Arrow 2).

Quasi resonant excitation For quasi resonant excitation a photon with the energy of a possible, regarding the selection rules, photonic transition within higher shells of the QD is needed. If this photon is absorbed, the e–h pair is directly generated within the QD, which results in an energetic shift of the transition due to Coulomb interaction, this limits this excitation variant to the

Figure 2.3.: Excitation scheme, 1: barrier/above band, 2: wetting layer, 3: quasi resonant (p–p solid; d–d dotted), 4: s–s resonant.

generation of a single e–h pair which can be seen as a benefit for SP generation. While this method needs the existence of confined higher shells it can not be used for all QDs, especially not for very small QDs with a shallow confinement potential. See Fig. 2.3 (Arrows 3).

Resonant excitation In the resonant excitation case, the lowest state, the s-shell is directly excited with an energetically matching photon. This method allows the highest conservation of spin and phase, but needs a very good suppression of stray light to separate excitation photons from luminescence. Also this method generates a single e–h pair in the QD. See Fig. 2.3 (Arrow 4).

For the latter two cases one has to note, that with a second photon, tuned to the shifted transition energy, further e–h pairs can be generated in the QD [59, 60]. There are also excitation schemes possible that make use of transitions between the barrier,

WL, and confined states, or even two-photon absorption, which are not explained here.

Electrical excitation Finally, if one thinks of a device structure, utilizing QDs, electrical excitation may be favorable due to a smaller footprint of the device and the absence of optical elements and light sources. For this method the sample has to be doped and contacted like LED structures to allow a current flow through the active region. However, the doping of the sample may have negative implications on the optical quality of the QDs due to electrical fields and dopant diffusion into the QDs [61, 62].

Acoustical excitation An other approach to excite QDs is the usage of strong shock waves which may be applied by laser pulses hitting metal films on the sample and then propagate through the structure [63]. This method is currently more and more investigated within the semiconductor physics community.

2.4. State Population

All discussed measurements in this work are based on above band or WL excitation, where many e–h pairs can be created and may relax into a QD. The number of created e–h pairs follows the Poissonian distribution:

$$f(k;\lambda) = \frac{\lambda^k e^{-\lambda}}{k!} \tag{2.5}$$

with λ the expected number of e–h pairs which can be associated with the excitation power density (EPD) (which should not be confused with *etch-pit-density*, used for crystal defect density measurements) and k the number of excited e–h pairs per excitation cycle. A visualization of this distribution is displayed in Fig. 2.4.

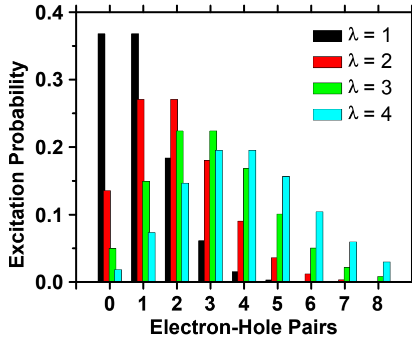

Figure 2.4.: Poisson distribution for $\lambda = \{1, \ldots, 4\}$.

2.4.1. Exciton: Bright State – Dark State

Assuming an excitation with only one e–h pair, a relaxation into the s-shell is possible. Due to the relaxation process, the electron spin and the hole spin can undergo random spin flips which results in two possible spin configurations, a parallel and a anti-parallel spin orientation for the X [58]. The selection rule for a photonic transitions only permits the recombination of the anti-parallel spin configuration $|\Uparrow\downarrow\rangle = |\pm 1\rangle$ which is therefore called the bright exciton state (BS), while the parallel spin configuration $|\Uparrow\uparrow\rangle = |\pm 2\rangle$ is optically dipole forbidden and referred to as DS. The symbols $\uparrow$ and $\Uparrow$ represent the electron spin and the heavy-hole spin, respectively. See Fig. 2.5.

Due to exchange interaction of the electron and hole spin the DS lies energetically lower than the BS [64].

The exchange interaction in its general form is proportional to the following integral [64] where it is obvious that the splitting is

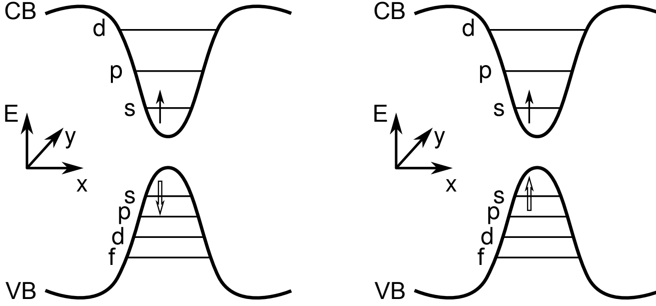

Figure 2.5.: Bright (left) and dark (right) X spin configuration.

strongly dependent on the size of the QD.

$$E_{\mathrm{ex}} \propto \int\int \mathrm{d}^3\vec{r}_1 \mathrm{d}^3\vec{r}_2 \Psi^{\star}_{\mathrm{X}}(\vec{r}_{\mathrm{e}} = \vec{r}_1, \vec{r}_{\mathrm{h}} = \vec{r}_2) \times \frac{1}{|\vec{r}_1 - \vec{r}_2|} \Psi_{\mathrm{X}}(\vec{r}_{\mathrm{e}} = \vec{r}_2, \vec{r}_{\mathrm{h}} = \vec{r}_1) \tag{2.6}$$

where Ψ_{X} is the exciton wave function and $\vec{r}_{\mathrm{e,h}}$ are the electron and hole coordinates.

There are two contributions for the spin exchange interaction, a *short-range* and a *long-range* part, the first gives reason to the BS–DS splitting and, in case of a reduced QD symmetry ($< \mathrm{D}_{2d}$), to a BS splitting. The latter alters these splittings, especially raising the DS splitting. The general form of the spin Hamiltonian for short-range exchange interaction is [65]

$$\hat{H}_{\mathrm{exchange}} = -\sum_{i=x,y,z} \left(a_i \hat{J}_{\mathrm{h},i} \hat{S}_{\mathrm{e},i} + b_i \hat{J}^3_{\mathrm{h},i} \hat{S}_{\mathrm{e},i} \right) . \tag{2.7}$$

Using the exciton states $(|+1\rangle, |-1\rangle, |+2\rangle, |-2\rangle)$ as basis, the

following matrix representation can be obtained:

$$\hat{H}_{\text{exchange}} = \frac{1}{2} \begin{pmatrix} +\delta_0 & +\delta_1 & 0 & 0 \\ +\delta_1 & +\delta_0 & 0 & 0 \\ 0 & 0 & -\delta_0 & +\delta_2 \\ 0 & 0 & +\delta_2 & -\delta_0 \end{pmatrix} \tag{2.8}$$

With the following abbreviations:
$\delta_0 = 1.5(a_z + 2.25b_z)$, $\delta_1 = 0.75(b_x - b_y)$, and $\delta_2 = 0.75(b_x + b_y)$.

One can deduce from the block diagonal form of the matrix that the bright and dark X do not mix with each other but are energetically split by the electron-hole exchange energy δ_0. The off-diagonal elements show that the states with a total spin $M = s_{\text{e},z} + j_{\text{h},z} = \pm 1$ and $M = \pm 2$ are each hybridized. The $|\pm 1\rangle$ states are degenerate within a D_{2d} symmetry.

The *long-range* exchange interaction can be included by replacing the $M = \pm 1$ block of the matrix (2.8) by

$$\begin{pmatrix} +\Delta_0 & +\Delta_1 \\ +\Delta_1 & +\Delta_0 \end{pmatrix} \tag{2.9}$$

with $\Delta_0 = \delta_o + \gamma_0$, $\Delta_1 = \delta_1 + \gamma_1$, and $\gamma_1 = \gamma_x - \gamma_y$. where $\gamma_{x,y}$ are the coupling constants for the long-range interaction.

While Δ_0 defines the splitting between BS and DS, the Δ_1 terms come into play for a broken symmetry $< D_{2d}$, which leads to $b_x \neq b_y$ and the eigenstates of $\hat{H}_{\text{exchange}}$ are symmetric and antisymmetric linear combinations and split by δ_1 which results in orthogonal linear polarisations of the fine-structure splitting components of the bright X, while the dark X with $M = \pm 2$ is split by δ_2 [64]. A direct measurement of the DS splitting has been performed by Poem, revealing a splitting energy of 1.4 µeV [66].

DS–BS splitting energies ranging from 100 µeV up to some meV have been reported in literature [62, 67, 68].

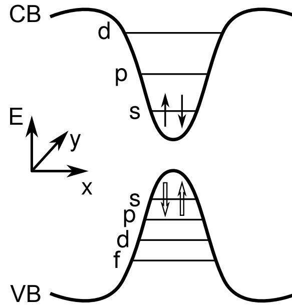

Figure 2.6.: Biexciton spin configuration.

2.4.2. Biexciton

For a higher EPD more e–h pairs are generated which can relax into the QD, so the possibility for the relaxation of an additional e–h pair into the QD s-shell before the first on is decayed raises, especially if the first one is trapped in the DS. See Fig. 2.6. This configuration is called a XX and its energy differs from the X energy due to an extra COULOMB *interaction* between the contributing four carriers. In contrast to the X the XX is not split due to its spin singlet character, but due to the fact that the final state of the XX is the eventually split X state the XX luminescence line might also be a doublet. The XX has two decay channels, one for each e–h pair with anti-parallel spin orientation, which results in a up to two times faster decay in comparison to the bright X [69, 70]. More details about the EPD-dependence of the X and XX are given in Section 2.7.1.

2.4.3. Charged States

Transitions with an additional charge carrier present in the QD are leading to positively charged trions (T^+s) or negatively charged

trions (T^-s) depending on the charge of the additional carrier. Coulomb interaction shifts these luminescence lines in a range of some meV.

2.4.4. Higher Shells

If the confinement potential is deep enough to contain more shells than the s-shell, a high excitation power density can lead to a filling of higher shells with e–h pairs which than can decay in correspondence to the transition rule, resulting in approximately equidistant luminescence lines [71].

2.5. Photon Statistics

Classical light which is e.g. radiated from hot bodies, flames, stars, etc. owns a photon statistics in which the occurrence of pairs of photons is enhanced by a factor of two for short time scales. This can be illustratively explained by the fact that this light sources have a very large number of independent single light emitters, e.g. atoms or molecules. If one looks from a point to such a light source, the emitted light waves can, within their very short coherence time, constructively or destructively interfere at this point of view. This results in an enhancement of the probability for two photons or zero photons with respect to other numbers within the mentioned short time scale.

If one now thinks of a laser as light source, one imagines a coherent light field within the mirrors of a resonator, one mirror randomly couples out some of the, due to their certainty in momentum delocalized, photons which results in a random number of photons with an equal probability for all numbers of photons.

A single two-level emitter, e.g. an atom, molecule, nitrogen vacancy (NV) [47], or as investigated in this dissertation, a single

QD, is only able to send out a single-photon in a time, and has to be re-excited before it is able to emit an other photon. This suppression of simultaneously emitted photons for a short time scale is called antibunching.

These three kinds of light sources have been precisely theoretically described by GLAUBER [72, 73] which was awarded with the NOBEL price in 2005 and FOCK [57].

2.5.1. Harmonic Oscillator Model of Light

The light field can be described by the superposition of single harmonic oscillator modes i, which can contain n photons, each carrying an energy

$$E_i = \hbar\omega_k n_i \ . \tag{2.10}$$

In analogy to an harmonic oscillator, one can define the Hamiltonian

$$\hat{H}_i = \frac{1}{2}\hbar\omega_i \left(\hat{a}_i^\dagger \hat{a}_i + \hat{a}_i \hat{a}_i^\dagger\right) \tag{2.11}$$

where $\hat{a}_i^\dagger$ is the creation and $\hat{a}_i$ the annihilation operator, adding or removing one photon to/from the mode, respectively [74–76].

2.5.2. Thermal Light

Light that is radiated from matter, consisting of many independent emitters whose states are thermally excited, like a light bulb, is called thermal or classical light. The probability P_{th} to emit a photon with an energy $E_i = \hbar\omega_i$ from an emitter into the mode i is following the BOLTZMANN distribution.

$$P_{\mathrm{th}}(n) = \left(1 - \exp\left(-\frac{\hbar\omega_j}{k_{\mathrm{B}}T}\right)\right) \cdot \exp\left(-\frac{n\hbar\omega}{k_{\mathrm{B}}T}\right) \tag{2.12}$$

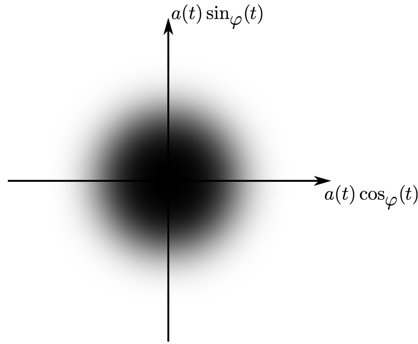

Figure 2.7.: Phase-space portrait of the thermal state with amplitude $|E(t)| = a(t)$ and a totally random phase $\varphi(t)$.

which results in a mean photon number $\langle n \rangle$ of a mode

$$\langle n \rangle_{\text{th}} = \sum_n n \cdot P_{\text{th}}(n) = \frac{1}{\exp\left(\frac{\hbar\omega}{k_{\text{B}}T}\right) - 1} \tag{2.13}$$

The *variance* of the Boltzmann distribution results in

$$(\Delta n)^2 = \left\langle n^2 \right\rangle - \langle n \rangle^2 = \langle n \rangle^2 + \langle n \rangle \tag{2.14}$$

which leads to a Gaussian distribution in phase-space [75] (See Fig. 2.7).

2.5.3. Coherent Light

Modes i of coherent light, which are e.g. radiated from a laser above threshold, are limited by the *minimum uncertainty product* of the photon number n_i and its phase φ_i

$$\delta n_i \cdot \Delta\varphi_i = 1 \; . \tag{2.15}$$

GLAUBER demonstrated in [72] that the states of coherent light are eigenvalues of the annihilation operator $\hat{a}_i$. In the basis of *number states* $|n_i\rangle$ the light field can be written as a superposition of these states [75, 76]

$$|a_i\rangle = \sum_n |n\rangle \langle n|a_i\rangle = \sum_n \exp\left(-\frac{1}{2}|a_i|^2\right) \cdot \frac{a_i^n}{\sqrt{n!}} |n\rangle \ . \tag{2.16}$$

The probability distribution of the photon number n in a mode results in

$$\begin{aligned} P_{\text{coherent}}(n) &= |\langle n|a_i\rangle|^2 \\ &= \exp\left(-|a_i|^2\right) \cdot \frac{|a_i|^{2n}}{n!} \ . \end{aligned} \tag{2.17}$$

Using

$$\langle n\rangle_{\text{coherent}} = \langle a_i| \left(\hat{a}_i\right)^\dagger \hat{a}_i |a_i\rangle = |a_i|^2 \tag{2.18}$$

equation (2.17) can be written as

$$P_{\text{coherent}}(n, \langle n\rangle) = \exp\left(-\langle n\rangle\right) \cdot \frac{\langle n\rangle^n}{n!} \tag{2.19}$$

which is a POISSON distribution (See Fig. 2.4 and 2.8).

The POISSONian distribution in phase-space is located around the mean value $\langle n\rangle$ of photons in the mode with a *variance*

$$(\Delta n)^2_{\text{coherent}=} \langle n\rangle \ . \tag{2.20}$$

A *relative variance* can be defined as follows

$$\frac{(\Delta n)^2}{\langle n\rangle^2} = \frac{1}{\langle n\rangle} \xrightarrow{\langle n\rangle\to\infty} 0 \tag{2.21}$$

which decreases with an increasing mean photon number, like in a laser cavity [75, 76].

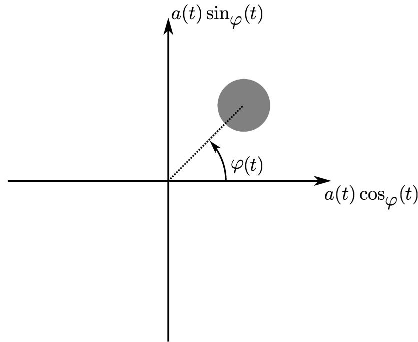

Figure 2.8.: Phase-space portrait of the GLAUBER state with amplitude $|E(t)| = a(t)$ and phase $\varphi(t)$.

2.5.4. Non-Classical Light

Non-classical light can be directly expressed as FOCK-state, which consists of just one state of the sum in equation (2.16)

$$|a_i\rangle = \sum_n |n\rangle \langle n|a_i\rangle \ . \tag{2.22}$$

Therefore the mean photon number $\langle n\rangle$ in a *number state* is exactly defined

$$\langle n\rangle = n \tag{2.23}$$

which results in a vanishing *variance* for the photon number

$$(\Delta n)^2 = 0 \ . \tag{2.24}$$

Fig. 2.9 shows the phase portrait of a number state with the photon number n projected on the radius and a absolutely undefined phase φ resulting in a circle [74, 76].

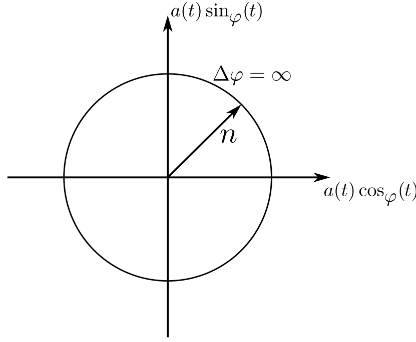

Figure 2.9.: Phase-space portrait of the FOCK state with amplitude $|E(t)| = a(t)$ and $\Delta\varphi = \infty$.

2.5.5. Verification of Light States

The states of light described above, can be verified in terms of photon statistics. The $g^{(2)}(\tau)$-function can be approximated by autocorrelation (ACO) measurements for short delay times τ. Especially interesting to distinguish light states, is the $g^{(2)}(\tau = 0)$ value

$$g^{(2)}(0) = \frac{\langle \hat{n}(\hat{n} - 1) \rangle}{\langle \hat{n} \rangle^2} = 1 + \frac{(\Delta n)^2 - \langle n \rangle}{\langle n \rangle^2} \ . \tag{2.25}$$

Here we find the previously defined figures of merit $\langle n \rangle$ and $(\Delta n)^2$ again. Using these values for the different light states, we find the following values (Table 2.1) for $g^{(2)}(\tau = 0)$.

Experimentally this can be realized by the utilization of a HANBURY BROWN and TWISS setup (HBT) (see Section 3.4.2) [74, 75, 77].

Fitting When the system is excited by a pulsed light source, the $g^{(2)}(\tau = 0)$ value can be derived by integrating the areas of

Light State	$\langle n \rangle$	$(\Delta n)^2$	$g^{(2)}(\tau = 0)$
Thermal		$\langle n \rangle^2 + \langle n \rangle$	2
Coherent		$\langle n \rangle$	1
FOCK	n	0	$1 - \frac{1}{n}$
FOCK $(n = 1)$	1	0	0

Table 2.1.: $g^{(2)}(\tau = 0)$ values for different light states.

the $\pm 1, \pm 2, \pm 3, \ldots$ histogram peaks and calculating their mean area. Then the ratio of the 'zero'-delay peak over the mean area is $g^{(2)}(\tau = 0)$.

$$g^{(2)}(\tau = 0) = \frac{A_0}{\langle \sum_i A_i \rangle}; \quad i = \{\pm 1, \pm 2, \pm 3, \ldots\} \tag{2.26}$$

In case of continuous-wave (CW) excitation the following function can be utilized to fit the data and calculate the $g^{(2)}(\tau = 0)$ value.

$$y(x) = a \cdot \left(1 - (1 - b) \cdot \exp\left(\frac{-|x - x_0|}{d}\right)\right) \tag{2.27}$$

In this equation, the histogram data $y(x)$ is fitted via the POISSON-level a, d the decay time and b represents $g^{(2)}(\tau = 0)$ at x_0, with $\tau \equiv x - x_0$.

Additionally, in the CW case the resolution of the setup leads to a convolution of the measured data with the *apparatus function*, which is the response of the setup, having a time-jitter of 700 ps, to a *delta-function*, in our case this is a GAUSS-function with a standard deviation of $\sigma = 0.297\,\text{ns} \approx \frac{0.7\,\text{ns}}{2\sqrt{2\ln(2)}}$.

Background Correction In case of a POISSONIAN background in the auto correlated signal, the $g^{(2)}(0)$ value can be corrected for that by obtaining the signal-to-noise ratio

$$\rho = S/(S+B) \tag{2.28}$$

with S the integrated signal and B the underlying background. Now one can define a background corrected value [78]

$$g^{(2)}_{\text{corr.}}(0) = g^{(2)}(0) - \left(1 - \rho^2\right) . \tag{2.29}$$

It is worth to note that this formula applies to the pulsed excitation case, whereas in CW-excitation the following equation is valid [78]:

$$g^{(2)}_{\text{corr.}}(0) = \frac{g^{(2)}(0) - (1 - \rho^2)}{\rho^2} \tag{2.30}$$

2.6. Cavity QED

2.6.1. Micro-Pillars

Cavity Dip

The samples used for micro-pillar (MP) structures own a planar cavity consisting of two distributed BRAGG-reflector (DBR) which are building up the cavity around the active medium. The emitters are located in an anti-node of the expected electrical field. Each DBR has a typical reflectivity curve for the wavelength of the light, consisting of a stopband with high reflectivity and adjacent oscillations in the reflectivity, two stacked DBRs can build up a cavity, in which photons can be stored if they are in resonance with the cavity. Figure 2.10 shows a typical luminescence of QDs within a planar cavity. Visible is the cavity dip around 635 nm and the stopband around it, followed by stopband oscillations to both sides [79].

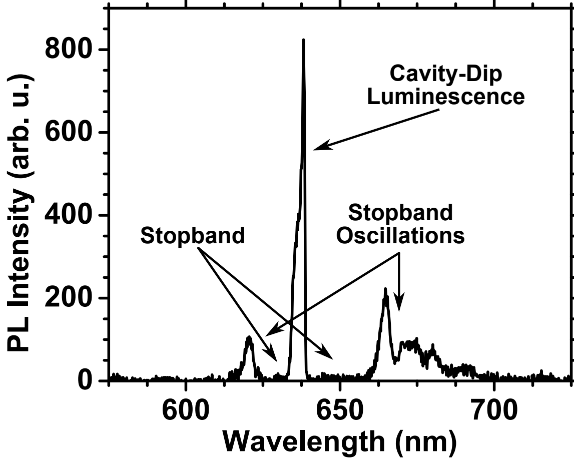

Figure 2.10.: Luminescence of a QD ensemble embedded in a planar cavity.

Quality Factor

If light is trapped in an optical cavity, the mean number of round trips of a photon within the cavity defines the *quality factor* Q of the cavity. The *quality factor* for optical cavities is defined as

$$Q = \frac{2\pi f_0 \mathcal{E}}{P} \tag{2.31}$$

with f_o the frequency of the observed mode and $\mathcal{E}$ the energy stored in the cavity and $P = -\frac{d\mathcal{E}}{dt}$ the dissipated power.

A direct measurement of photon round trips is of course very difficult to achieve. An other definition which is valid for high Q values and which has parameters that are experimentally accessible, is of the form

$$Q \approx \frac{\lambda}{\Delta\lambda} \tag{2.32}$$

with λ being the wavelength of the cavity mode and $\Delta\lambda$ its full-width at half-maximum (FWHM), important for this definition is, that the mode has to be energetically fully filled by coupling emitters and that there is no absorption happening inside the cavity by the emitters, which is given at a certain EPD where the emitters are excited and therefore can not absorb the trapped photons, this EPD is called *transparency point* [80–82].

Mode Coupling

If the QDs luminescence is in energetically in resonance with the cavity mode and the QD is spatially located in an anti-node of the mode field, a coupling of cavity and QD leads to a shorter decay time due to the PURCELL-*effect* [76, 83] and the emitted light is directed along the pillar axis. A faster decay time is essential for high frequency single-photon sources (SPSs), where the decay constant naturally limits the repetition rate and highly directed emission allows a better collection efficiency of the generated photons.

Additionally the regimes of weak and strong coupling open interesting fields for new physics and applications, far beyond the scope of this work [84–90].

2.7. Excitation Power Dependence

Finding an appropriate EPD for a type of experiment depends on several properties. In nearly any case the quality of the measurement and signal to noise ratio improves at higher count rates. But additional generated carriers, by raising the EPD, may also lead to fluctuating electrical fields, leading to an energetically wandering of the luminescence line on time scales faster than the integration time of the experiment and therefore to a broadening

of the investigated line, which is called *spectral diffusion*. This effect has been temporally analyzed by [91]. Further aspects are discussed in the following sections.

2.7.1. Exciton–Biexciton Dynamics

Even in case of a negligible BS–DS splitting, the X luminescence will saturate with a raise of the EPD, because chances for a XX decay are growing due to the capture of additional e–h pairs within the recombination time of the X. Investigation of the EPD dependence of the X and XX luminescence intensity can help to distinguish these lines. The following equation describes how the integrated intensity of the luminescence line I depends from the EPD P

$$I \propto P^b \tag{2.33}$$

with b being the slope of this dependency which results theoretically in $b = 1$ for an X and in $b = 2$ for a XX.

This results from the e–h pair generation process, following the POISSON-distribution (Eq. (2.5)) for a single QD with a small carrier-capture volume. In addition, a dominantly linear EPD-dependent e–h pair-loss to neighbor QDs and non-radiative decay channels, like defects, is assumed.

Fig. 2.11 shows the probability for the generation of one and two e–h pairs with respect to the mean value of the POISSON-distribution, which is proportional to the EPD. Obviously, the probability curve for one e–h pair has a slope of one, while the slope is two for the probability of two e–h pairs which are needed to form a XX.

Important to note is, that when *mirroring the luminescence* of the (bright) X or the XX, these having a slope of one or two, respectively, is only valid in simple cases of rate-equations [62]

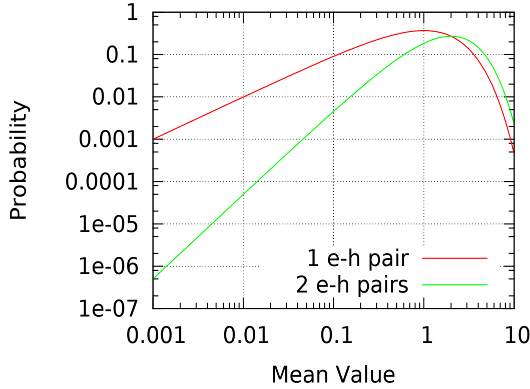

Figure 2.11.: Probability for the generation of one (red) and two (green) e–h pairs versus the *mean value* of the POISSON-distribution.

where the X and XX populations can be seen as approximately independent of each other and any loss-channels.

In the general case, e.g. one e–h pair can be trapped in the DS at low temperatures for the whole integration time of he measurement. As a result, the XX-formation takes place after the generation *one* (additional) e–h pair and therefore the XX will show a slope of *one* in this case, like otherwise an X would do.

In addition, any strong loss-channels or redistribution of the populations by mixed terms in the rate equations [62], can also alter the mirrored slopes.

2.7.2. Higher Shells

Luminescence of higher shells, if they are confined in the QD, can be observed when the EPD is further enhanced. In this case, the capture rate of e–h pairs becomes higher than the decay

rate in lower shells, and emission from all shells can happen simultaneously. The luminescence lines are then renormalized due to COULOMB *interaction* [71, 92].

2.7.3. Red- and Blue-shift

The surplus energy of above band excitation is disposed in the generation of phonons, which results in a local heating of the sample. This leads to a red-shift of the luminescence, due to an increase of the lattice constant and therefore to a lowering of the band gap, see Sec. 2.8.1.

In cases where internal electric fields are leading to already red-shifted luminescence energies at low EPDs due to the *quantum-confined* STARK-*effect* [83, 93–95], the generation of additional e–h pairs can lead to a *screening-effect* canceling out these fields to a certain amount, which then results in a blue-shift with raising EPD [96].

2.8. Temperature Dependence

The photon emission of QDs is strongly affected by temperature. In the following section these effects will be explicated and analysis methods will be discussed in order to derive quantitatively which phonons are inducing the observed behaviors.

2.8.1. Bandgap Shift

Generally, solid state matter expands with raising temperature, this can be explained by an increasing vibration of the atoms building up the lattice, which leads to a growing equilibrium distance of the atoms. This results in a reduced bang gap energy

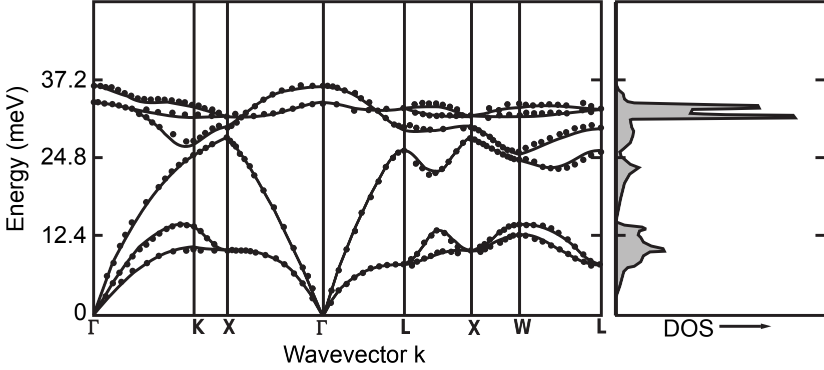

Figure 2.12.: (left) Dispersion relation of GaAs phonons. **(right)** Corresponding density of states [99].

E_G described empirically by VARSHNI

$$E_\mathrm{G}(T) = E_\mathrm{G}(0) - \frac{\alpha T^2}{T+\beta} \tag{2.34}$$

with α $\left[\frac{\mathrm{eV}}{\mathrm{K}}\right]$ and β [K] being material constants [97].

O'DONNEL and CHEN found a more analytic expression for this effect derived from the entropy and enthalpy of the formation of electron-hole pairs in semiconductors in [98]:

$$E_\mathrm{G}(T) = E_\mathrm{G}(0) - S\left\langle\hbar\omega\right\rangle\left[\coth\left(\left\langle\hbar\omega\right\rangle/2k_\mathrm{B}T\right) - 1\right] \tag{2.35}$$

with S being a dimensionless coupling constant and $\langle\hbar\omega\rangle$ the average phonon energy. In this work the latter expression will be used to gain information about the average phonon energy affecting an observed band gap change in the sample.

Typical dispersion relations of phonons are shown in Fig. 2.12 for the example of GaAs.

2.8.2. Cavity Shift

Cavities formed by DBRs around an active medium also experience a red-shift with raising temperature. This shift is weaker than the above mentioned and results from the expansion of the DBRs, the cavity material and from a change of the refractive index of these materials. The different temperature dependencies allow a tuning of QD emission energy with respect to the cavity dip [61, 100].

In metal-organic vapor-phase epitaxy (MOVPE) grown samples additionally a negative layer thickness gradient from the center of the wafer to the outer area leads also to a site-dependent blue-shift of the cavity dip, allowing to choose an appropriate location for a volitional detuning between QD-ensemble luminescence and cavity dip [61, 100].

2.8.3. Dark State Dynamics

The fact that the X splits into BS and DS and that state filling occurs when one raises the EPD has implications on the choice of the appropriate EPD.

Depending on the temperature and the BS–DS splitting energy, the X tends to spin-flip into the DS on a time scale shorter than the X decay and is trapped in this state if no phonon is available to allow a back-flip into the BS.

Then the capture of an additional e–h pair leads to the formation of the XX state. The decay of this state leaves behind a X in the BS that again flips into the DS and therefore no X recombination is observed.

Raising the temperature brings phonons into existence, following the Boltzmann-distribution, that can provide the energy for "back-flipping" of the DS into the BS, leading to an onset of thermalization of BS and DS and therefore allows the bright X

transition. Rate-equations for this process can be found in [62] and have been used for numerical simulations in Section 9.

2.8.4. Blue-shift

The above mentioned effects are both leading to a red-shift with increasing temperature, under certain circumstances one observes a blue-shift, which can be attributed to carriers that are trapped in the potential landscape in direct vicinity to a QD, applying an STARK-shift [101].

At elevated temperatures, these carriers can be freed from their traps by increasing phonon scattering neutralizing the electrical field and therefore the initial red-shift, leading to an observation of a temperature dependent blue-shift.

2.8.5. Spectral Linewidth Broadening

With increasing temperature, the state population of phonons is following the BOLTZMANN-distribution and therefore the probability of phonon carrier scattering. As a result, the FWHM of the QD luminescence lines increases with temperature following the dependency [102]

$$\Gamma(T) - \Gamma(T=0) = \alpha T + \frac{a}{\exp\left(\frac{E_{\mathrm{A}}}{k_{\mathrm{B}}T}\right) - 1} \qquad (2.36)$$

with α [µeV/K] associated with a linear longitudinal acoustic (LA) and transversal acoustic (TA)-phonon interaction at low temperatures, while a [µeV] is a coupling factor for an activation energy E_{A} in the range of longitudinal optical (LO) and transverse optical (TO)-phonons (See Fig. 3.3), resulting in an exponential spectral emission line broadening at higher temperatures.

In addition, scattering between charge carriers at high EPDs is a further mechanism for spectral linewidth broadening. This may have an influence on temperature dependent measurements, too, as the charge carrier mobility can be enhanced with temperature.

The XX luminescence may than energetically overlap with the X luminescence line, especially for thermally broadened luminescence lines, depending on the XX binding energy which varies with the confinement potential of the QD. This overlap has implications on the photon statistics in the energetically overlapping region. This negative effect on the purity of SPs is further discussed in section 9.

2.8.6. Dark State

In comparison to other material systems, InP-QDs have a large BS–DS–splitting [62, 67, 103]. Therefore the spin-flip rate into the DS is high and the e–h pair is trapped until it can scatter with an appropriate phonon. This can result in spectra where the X emission line is not observable for low temperatures at all. With raising temperatures phonons are excited and back-flips into the BS become possible, at a temperature where $k_\mathrm{B}T$ is comparable to the BS–DS splitting energy, a thermalization of BS and DS occurs, and the X lifetime is found to be double the value than without the existence of a DS. Rate equations describing the BS–DS–dynamics can be found in [62].

2.8.7. PL Intensity

At elevated temperatures the average phonon energy becomes comparable to the energy difference of confined charge carrier states within the QD and therefore allows an excitation of these charge carriers into higher states prior to their recombination. At

higher average phonon energies the carriers can even be directly excited into the WL or barrier. This results in an "activation-like" behavior of the intensity quenching with raising temperature. Arrhenius described such an behavior for chemical reactions [104]. His equation can be adapted in terms of a temperature dependence of the intensity

$$I(T) = \frac{I_0}{1 + \sum_n b_n \cdot e^{-E_n/k_\mathrm{B}T}} \tag{2.37}$$

with the zero-phonon intensity I_0, n activation energies E_n and their coupling coefficients b_n. One can reveal activation energies for a phonon mediated loss of carriers into the WL or barrier, or even the energy level separation for the carriers which may "climb up" their "ladder of states" by multiple phonon scattering processes leading to a quenching of the QD luminescence [43, 62, 71].

3. Experimental

The following sections will present details regarding the experimental methods used to acquire the data presented in this thesis. It will also describe the different types of samples which are based on different substrates and are treated with different pre- and post-processing techniques.

3.1. Materials

3.1.1. CMOS Compatibility

A main focus of this work is the integration of optical semiconductor materials owning a direct band gap within the well established complementary metal oxide semiconductor (CMOS) processes that are based on exactly oriented Si(001)-wafers. There are three main problems for hetero-epitaxy of these two materials, the lattice constant mismatch of about 4%, the combination of the non-polar Si with the polar GaAs and the different thermal expansion coefficients of the materials [105].

In this work three approaches to tackle the first two problems were investigated and the results were compared to the native GaAs-wafer processes.

3.1.2. Wafer Materials

InP-QDs are traditionally fabricated on GaAs-wafers, because of a well matching lattice constant between GaAs and aluminum gallium indium phosphide (AlGaInP), containing 51% (AlGa), which is used as barrier material, enhancing the confinement potential for the InP-QDs. A main subjective of this work is the optical investigation of InP/AlGaInP-QDs fabricated in a CMOS compatible way, which traditionally uses (001) orientated Si-wafers. Si owns an indirect band gap and is therefore very inefficient for optical emitters. The lattice mismatch to GaAs demands an intermediate buffer structure to allow the transition to a crystalline GaAs deposition on which conventional InP-QDs can be fabricated.

GaAs Substrate

The GaAs substrate is the most common substrate for MOVPE-grown InP-QDs. It is a polar semiconductor material with a zink-blende structure.

In order to prevent an ordering of barrier materials, a 6° mis-cut, with respect to the (001) crystal axis, of the wafer is often used [100]. However, the resulting atomic steps on its surface tend to act as crystallization seeds for QDs raising their density, which often makes post processing methods necessary to allow optical access to single QDs.

The usage of exactly oriented GaAs(001) substrate allows a lower density of InP-QDs at the cost of a lower confinement potential due to the above mentioned ordering effects within the barrier material [100, 106, 107].

Si Substrate

Si wafers are non-polar and own a diamond crystal structure. The bandgap of pure Si is indirect. About 96% of all produced electronic devices are based on exactly oriented Si(001) wafers. Low-cost, high-purity wafers with diameters up to 300 mm are common in industrial processes. The orientation of the crystal axis and a limited usable layer thickness of about 1 µm is challenging for the integration of naturally GaAs based optical devices on this kind of wafers [105]. Up to now, most optical devices have been realized on miscut Si-wafers [30]. In order to allow CMOS-compatibility, one has to adapt to exactly oriented Si wafers and is limited in the layer thickness due to following lithography steps within the process. In addition, limitations in process temperatures exist, depending on the allowed temperature range of the full device structure.

In this work the implementation of InP-QDs on Si substrate based systems requires the deposition of GaAs as a basis for the QD fabrication. Therefore, the large lattice constant mismatch from the Si-matrix to the GaAs-matrix has to be compensated by buffer layers, relaxing the strain and avoiding the formation of threading dislocations and APDs which can act as non-radiative recombination centers or form potential traps, internal electric fields etc. lowering the optical efficiency and quality of the samples [105].

3.2. Sample Fabrication

3.2.1. Epitaxial Growth Techniques

Two epitaxial growth techniques have been utilized in the fabrication process:

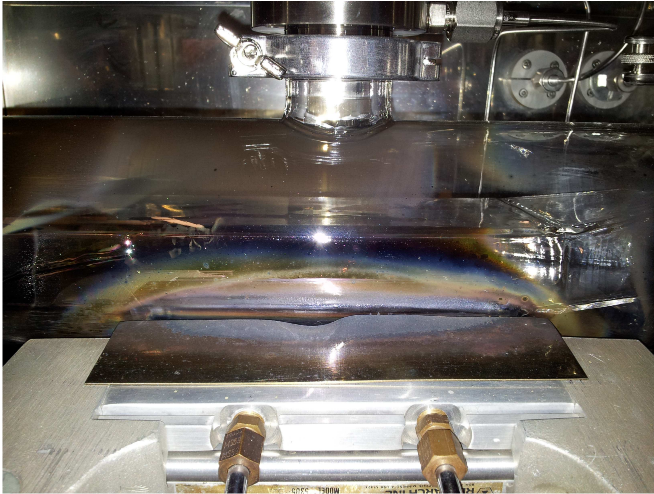

Figure 3.1.: Photo of the Aixtron 200 reactor.

Metal-Organic Vapor-Phase Epitaxy All QD-structures investigated within this work are fabricated by an Aixtron 200 MOVPE system[1] with standard precursors (trimethylgallium, trimethylindium, trimethylaluminium, arsine, and phosphine) and a horizontal reactor at 100 mbar pressure (Figure 3.1), heatable by an infrared (IR)-lamp.

Molecular Beam Epitaxy For this work some Si substrates are prepared with a germanium virtual substrate (GeVS) by the *Institut für Halbleitertechnik (Universität Stuttgart)*. The Ge was deposited by molecular beam epitaxy (MBE) on Si wafers at low temperatures of ≈400°C in several layers with intermediate annealing steps.

[1] Further information can be found on http://aixtron.com.

3.2.2. GaAs Buffer

The deposition of an intermediate buffer layer is of high importance to create a suitable crystal surface for the barrier deposition. For the fabrication of InP-QD structures on GaAs substrates, a 100 nm GaAs buffer layer is grown before switching to the AlGaInP barrier material.

The deposition of GaAs on surfaces with mono-atomic steps leads to the formation of APDs. The first deposited atomic layer consists of As atoms which are then followed by Ga atoms to build up the GaAs-matrix. This results in As-As and Ga-Ga bonds, building up the anti-phase boundaries (APBs) [108].

3.2.3. Barrier Material

InP-QDs are embedded in $((\mathrm{Al}_x\mathrm{Ga}_{1-x})_y\mathrm{In}_{1-y})_{0.5}\mathrm{P}_{0.5}$, while the group III material fraction y is adjusted to 0.51 in order to achieve lattice matching at growth temperature [109].

SP emission at elevated temperatures requires a high carrier confinement potential. Raising the Al content x in the AlGaInP widens the band gap of the compound, as shown in Fig. 3.2.

AlGaInP has a transition from a direct to a an indirect band gap at an Al-content of about 50 %. The phonon energies for different Al contents in AlGaInP are depicted in Fig. 3.3.

Ordering of the compound materials within the barrier can lower the band gap energy. The usage of miscut GaAs substrates helps to prevent the ordering, but the atomic steps on the surface of the miscut substrate are nucleation cites for QDs and are therefore raising their spatial density [106, 107, 110].

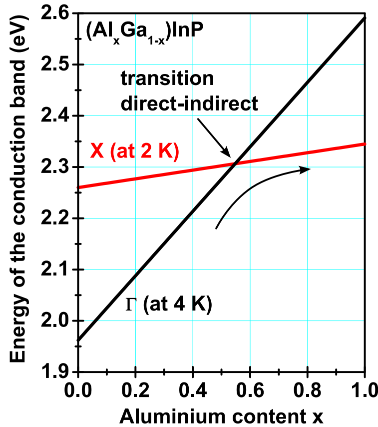

Figure 3.2.: Al dependence of the AlGaInP band gap.

3.2.4. Quantum dot fabrication

In the last years many types of QDs and ways to fabricate them have been developed. Nano crystals in solution, for example, are treated with wet chemical methods to form core-shell QDs. QDs can also be fabricated by lithographic methods by etching on two-dimensional electron gases in semiconductor heterostructures with the possibility to apply electrodes in direct vicinity of the QDs [112].

Many different semiconducting materials are used for their fabrication, allowing luminescence from near UV down to near IR.

A map showing the band gap versus the lattice constant for many semiconducting compounds is depicted in Fig. 3.4.

This dissertation deals with self-assembled QDs that are fabricated by MOVPE in the Stranski-Krastanov (SK) growth mode [113]. This self-organization process is driven by the prin-

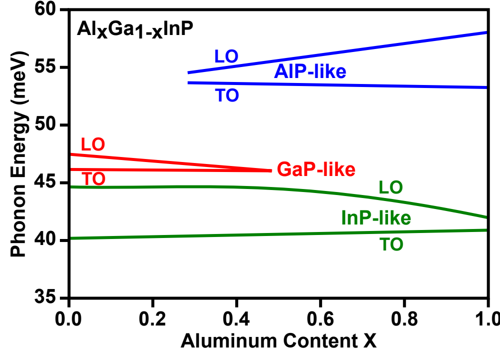

Figure 3.3.: Al dependence of the AlGaInP phonon energies [111].

cipal of energy minimization. The sum of surface and interfacial energies is given by

$$\Delta\sigma = \sigma_{\text{int}} + \sigma_{\text{sur}} - \sigma_{\text{sub}} \tag{3.1}$$

with σ_{int} the interface energy, σ_{sur} the surface energy and σ_{sub} the energy of the substrate surface.

In the SK growth mode, the lattice mismatch of QD material and substrate leads to a surface energy σ_{sur} which is layer thickness dependent. While $\Delta\sigma \leq 0$ the QD material tends to build up a closed film of atomic mono layers on the substrate, the strain accumulates and after some layers, exceeding the critical thickness, the sign of $\Delta\sigma$ becomes positive. Now the formation of islands, which incorporate less strain energy, starts, using also some of the already deposited atoms of the WL. The resulting structure is depicted in Fig. 3.5. To complete the three dimensional confinement potential, the islands and the thin remaining WL are then capped with barrier material, completing the three dimensional confinement potential, and finishing the QD fabrication.

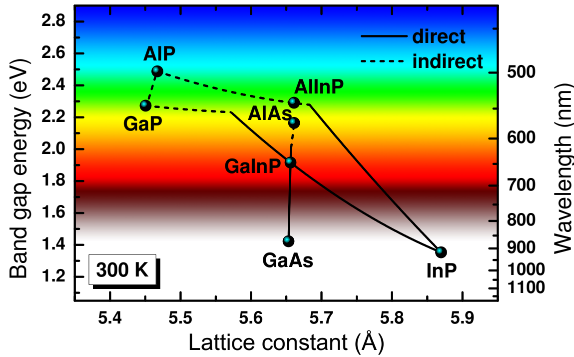

Figure 3.4.: Epitaxy map showing the band gap energy versus the lattice constant for compounds used in this work.
(Slightly modified version of Robert Roßbach)

3.3. Gaining Access to a Single QD

Accessing a single InP-QD on a plain sample is difficult due to the small lateral QD dimension of about 20 nm and their high density of typically $\approx 10 \times 10^{10}\,\mathrm{cm}^{-2}$ especially on 6°-tilted substrates, while having an excitation/collection spot of about 1.5 µm in diameter. Depending on the uniformity of the QDs energetic ensemble distribution, one collects light from hundreds of QDs.

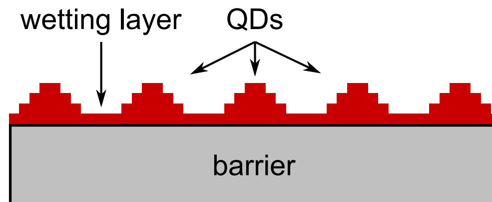

Figure 3.5.: Schematics of SK growth mode.

Even when examining the edges of their energetic distribution, the chances are extremely low and the spectrally separated QDs one may find there, are not the nominal grown ones.

To enhance chances of addressing a single QD, several processing methods have been utilized. One can divide these methods into three groups, post-processing of a plain QDs samples, pre-processing the substrate or buffer material before the growth of the QDs or reducing their density down to $\approx 5 \times 10^7\,\mathrm{cm}^{-2}$ by special growth recipes to allow the investigation of a single QD within the collection focus.

3.3.1. Post-Processing of Samples

Mesas

An approach to limit the amount of investigated QDs is to cut away most of the QDs leaving areas of QDs behind that are smaller than the size of the collection spot. To fabricate these areas, the so called mesa, requires a pattering of the plain sample surface in the sub-µm range. This can be done by means of lithography or spin-coating with diluted polymer micro-spheres to protect areas from etchants which remove the QDs beside [61].

The drawback of this approach is the generation of additional side surfaces with defects around the QDs. This defects generate surface states, allowing generated carriers to escape to and build up local electrical fields, adulterating the quality and intensity of QD luminescence.

Shadow Mask

In order to prevent the generation of additional surfaces in the vicinity of the QDs one can cover the sample by a nontransparent metal layer, leaving just small holes open. This can be

accomplished by the same means as mentioned above, spheres or lithography [61].

Due to the fact that these holes have to be smaller than the collection spot on the sample, the hole sizes are in the order of the wavelength of the luminescence and excitation light, leading to diffraction and therefor to a lowering of the excitation and collection efficiency.

Micro-Pillars

To overcome the problems of the processing methods mentioned above, a more sophisticated technique can be used. This method is similar to the mesa approach, but accomplished with an focused ion beam (FIB) to mill out areas with QDs having steep and smooth side walls. Additionally the integration of DBRs below and above the QD layer forming a λ-cavity for the luminescence of the QDs has several advantages. MPs that act as part of a cavity system require smooth sidewalls in order to confine the light in lateral direction via the refractive index step to vacuum/air and to minimize the scattering of confined light. A possible realization method for their fabrication is the FIB process.

Appliance of FIB for sample processing allows great flexibility for various shapes and smooth, steep sidewalls of the etched structures, at the cost of a slow speed [114]. The manipulation of the sample is realized by accelerating ions in an electrical field of 1 to 50 keV and focusing them in a spot down to $\approx$2 nm on the sample. The sample material is physically removed by sputtering, allowing to mill out structures within a nm scale. The FIB machine is usually combined with an scanning electron microscope (SEM) to allow in-situ observation of the etching process.

The SEM-image in Fig. 3.6 shows two MP structures which are located in craters. Milling of the shown structure takes about

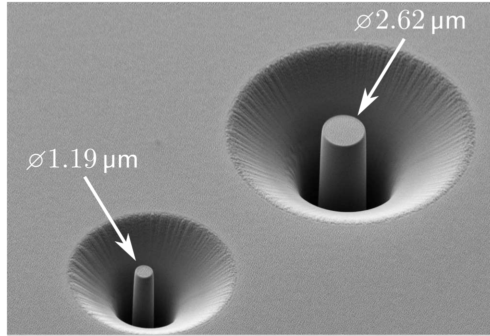

Figure 3.6.: SEM image of two micro pillars, fabricated by FIB.
(by Tim Thomay, University of Konstanz)

45 min. Due to that, it is not possible to gain free standing MPs by removing the whole surrounding barrier material using only FIB and therefore, optical access is just possible from the top, also scattering of light at the crater wall is possible, especially in the case of MPs smaller than the spot size of the objective used for excitation and collection.

3.3.2. Pre-Processing of Samples

Langmuir-Blodgett-Process

With the LANGMUIR-BLODGETT-process the generation of nucleation cites for the QD formation in a suitable low density for micro-photoluminescence (µ-PL) measurements is possible [115, 116]. To achieve a pattern of sub-µm holes, micro-sphere photolithography in combination with wet chemical etching can be used as a fast and low-cost method to produce regular arrays in a GaAs surface, which are suitable for controlled nucleation of self-assembled InP islands [117].

The self-assembly process of micro-spheres on a water surface allows the formation of a hexagonally close packed mono-layer, which can be transferred on the sample surface covered with a 400 nm thick UV-sensitive photo resist.

In the following exposure step, the micro spheres act as lenses for the UV-light, allowing for a sufficient exposure only below the spheres. With a variation of exposure and development time, the resulting hole size can be adjusted [118].

After the removal of the developed photo resist, which results in a regular patterned hole-mask, pits can be etched into the surface which can act as nucleation sites for the QD material, due to an alteration of the chemical surface potential. Therefore, a growth sequence of GaAs-buffer, gallium indium phosphide (GaInP)-barrier and InP for the QD formation was applied on the etched sample.

3.3.3. In-Situ Quantum dot density reduction

Attempts to tackle the problem of the very high QD density, varying of temperature, pressure and the amount of offered QD material during QD formation, had only slight effects on the QD density, not sufficient for single-QD spectroscopy [61, 100].

Another approach to affect the QD density are changes in the atmospheric composition inside the reactor in the ripening phase of the QDs, like growth interruptions reported for the InAs/GaAs system [119]. Therefore the influence of a phosphine flow interruption after the deposition of the InP on the QD formation was investigated. See Sections 4.2

3.4. Experimental Techniques

The characterization of nano-structure photoluminescence properties at different temperatures, requires several measurement techniques. The spectral information and efficiency of photon emission as well as the purity of SPs and their FWHM have to be characterized. Therefore, time dependent analysis of the luminescence lifetime and photon statistics are of high interest. The next sections will provide the reader with the necessary information regarding the applied measurement techniques.

3.4.1. µ-Photoluminescence Setup

The fundamental measurement system is the µ-PL-setup (Fig. 3.8), which allows precise positioning of the sample, controlling its temperature and allows a high spectral resolution combined with a high detection efficiency. Also the sample excitation light source is part of this setup.

The reader will now be conducted through the setup, following the path of light from the source to the detectors. The excitation source of the setup is a pulsed super-continuum fiber laser with a repetition rate of 50 MHz that radiates light with a spectral distribution ranging from 450 to 2000 nm with an average power of 3 mW/nm and a wavelength dependent pulse-width of ≈200 ps. This light can either be spectrally filtered by an acoustic optical tunable filter (AOTF) or a monochromator allowing a spectral width of $\Delta\lambda \approx 3$ nm or down to $\Delta\lambda \approx 0.05$ nm, respectively.

The excitation light can be attenuated by a gradient neutral-density filter (not shown in Fig. 3.8) over several orders of magnitude and is then directed on a 95/5 beam splitter, reflecting 95% of the light on a powermeter head to control the EPD. The remaining 5% of the collimated light are used for excitation and

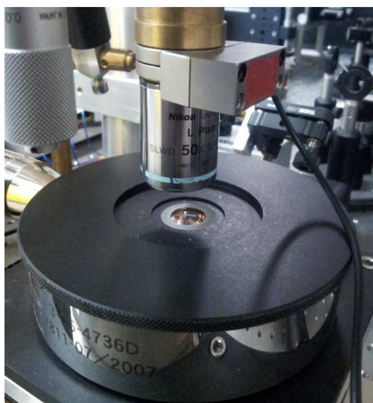

Figure 3.7.: Photography of the He-flow cryostat, allowing measurements at temperatures ranging from 4 to 350 K, and the 50× objective with super-long working distance of 17 mm and an NA of 0.45 mounted on a piezo-actuator.

are focused by an infinity corrected 50× objective (numerical aperture (NA) 0.45, working distance (WD) 13.8 mm), resulting in an excitation spot diameter of ≈1.5 µm on the sample (See Picture 3.7). Additionally a white-light source is available for sample illumination allowing an orientation on the sample. Luminescence light from the sample is collected via the same objective and 95% of it is reflected into the detection arm by the beam splitter.

The sample is mounted on a heatable cold-finger He flow-cryostat which allows sample temperatures ranging from 4 to 350 K. The luminescence or the white-light can be directly sent to a charge-coupled device (CCD)-camera resulting in an image which can be used for orientation on the sample or checking of the excitation spot.

For analysis, the light in the detection arm is filtered to suppress scattered excitation light and coupled into an spectrometer. The spectrometer is equipped with a interchangeable grating turret[2] containing tree gratings: 300 lines/mm, 1200 lines/mm, and 1800 lines/mm. A switchable exit mirror allows to analyze the

[2]See http://www.roperscientific.de/Spectrapro.html

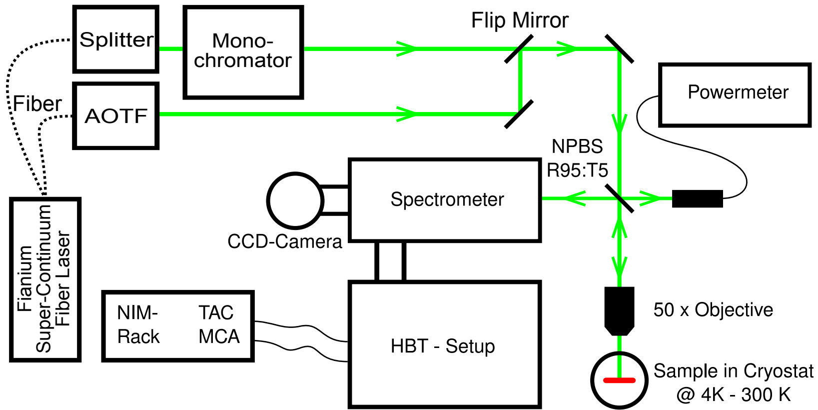

Figure 3.8.: Schematic μ-PL-setup.

dispersed light with a back-illuminated CCD-camera, resulting in a maximal spectral resolution better than 130 μeV (typical with 1200 lines/m $<$ 250 μeV).

By flipping the mirror in front of the CCD-camera, one can send the light through an variable exit slit, allowing to pass light which would hit 1 up to 20 pixel of the CCD-camera spectrum, to an analysis box for time dependent measurements, which is described in the next sections.

3.4.2. HBT Setup

In order to measure the photon statistics of the investigated luminescence, the light is divided into two paths by sending it through a 50/50 non-polarizing beam splitter, which results in a probability of 50% for two simultaneously emitted photons to be sent in different detection arms. At each end of these paths an Si-based avalanche single-photon detector (ASPD) is placed

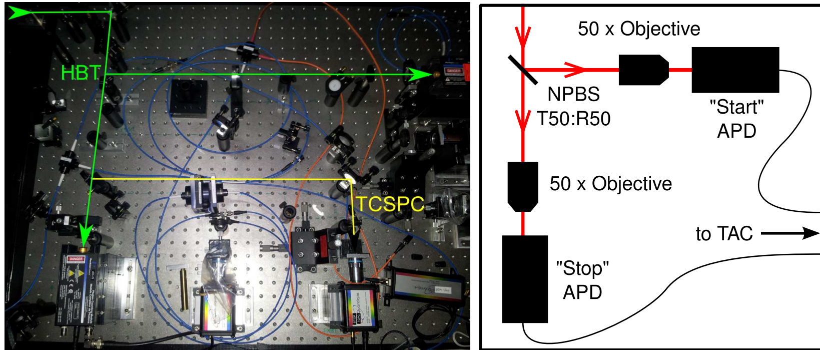

Figure 3.9.: (left) Photography of the HBT(green)/TCSPC(yellow) setup. **(right)** Schematic HBT-setup.

which are sending their detection events to a time-to-amplitude converter (TAC) (see Fig. 3.9), this kind of setup was invented in 1958 by Hanbury Brown and Twiss [120]. Each of the ASPDs used for the measurement have a temporal jitter of 350 ps and a quantum efficiency of 70 % at 670 nm, resulting in a temporal resolution of 700 ps for the whole setup.

A TAC is a high-precision stop-watch, it loads a capacitor when getting a start-signal and sends out a pulse with the accumulated voltage of this capacitor when receiving a stop-signal. A multi-channel buffer (MCB) then stores this event as a "click" in one of its channels. The used channel depends on the amplitude of the pulse. The channel information can be read out by a computer, resulting in a histogram of recorded delays between detection events. The signal of the "stop"-ASPD can be delayed by several ns, resulting in negative delay times allowing a shift of the "zero delay" channel into the middle of the histogram.

It is worth to note that an ASPD emits a broad, weak light-pulse, ranging from red to near infrared (NIR), which is generated

by the amplification process when a photon is detected. This light-pulses can be reflected to the other ASPD, leading to the so called "cross-talk"-effect. To suppress this, short-pass filters with a transition wavelength of 750 nm are placed between the ASPDs and the beam splitter.

3.4.3. Time-Correlated Single-Photon Counting Setup

The temporal evolution of luminescence lines can be investigated with a similar technique as described above. If one of the ASPDs is exchanged with a photo-diode which is directly hit by the laser pulses, the delay between excitation and luminescence can be investigated. The resulting histogram in the MCB then shows the decay characteristics by integrating over many decay processes, allowing to extract decay times of the investigated luminescence. Experimentally one uses the laser signal for the "stop"-channel of the TAC to enhance the probability of having a stop-event for every detected luminescence photon, what results in a time-inverse histogram. In case of TCSPC measurements an ASPD with a higher temporal resolution of 20 ps was used, at the cost of a lower quantum efficiency of just 20 % at 670 nm.

4. InP QDs on GaAs/GaAs Substrate

This chapter will present the measurements of InP-QDs grown on miscut and exactly oriented GaAs-wafers. Some samples are post- or pre-processed with different techniques (described in Section 3.3.2) like MPs or pre-pattering of the sample or reduction of the QDs density by a special recipe on exactly oriented GaAs-substrate.

4.1. Micro Pillars

In order to access single QDs and to enhance the collection efficiency a sample with standard InP-QDs, sandwiched within a pair of DBRs, has been processed with micro-pillars (MPs). The plain sample was therefore etched by FIB[1], to mill out several MPs with different diameters ranging from 0.5 to 3.8 µm; a SEM image is displayed in Fig. 3.6.

Figure 4.1 shows the schematic structure of an MP. Based on a GaAs-buffer 44 pairs of AlAs/$(Al_{0.5}Ga_{0.5})As$ DBRs are deposited. The active region is formed by $(Al_{0.55}Ga_{0.45})InP$ and $(Al_{0.2}Ga_{0.8})InP$ barrier layers, InP-QDs and $(Al_{0.2}Ga_{0.8})InP$ and $(Al_{0.5}Ga_{0.5})InP$ barrier layers, forming a λ-cavity for the QD luminescence. Above that, again 36 DBR-pairs of $(Al_{0.95}Ga_{0.05})As$/

[1] by Tim Thomay, University of Konstanz

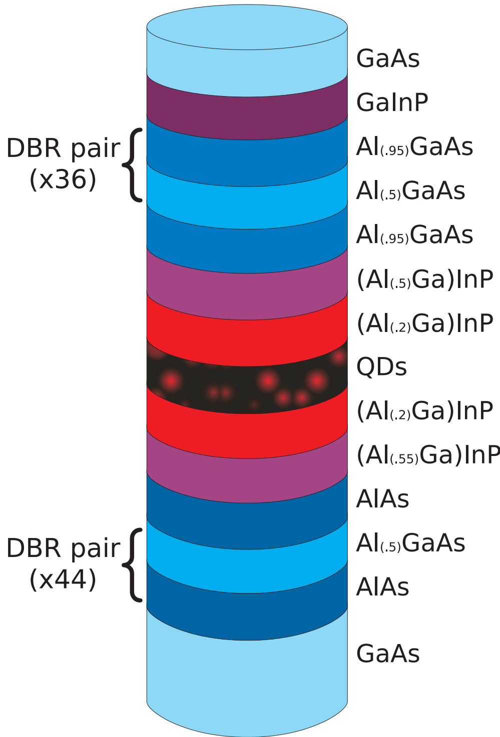

Figure 4.1.: Schematic structure of the micro pillar sample with a λ-cavity and the QDs located in the anti-node of the electrical field.
The dimensions of the layers are not represented correctly in this scheme.

$(Al_{0.5}Ga_{0.5})As$ are deposited and capped with a GaAs layer. A detailed discussion of the sample fabrication can be found in [61, 82].

As described in Section 2.6.1, MPs can show a characteristic mode spectrum, if emitters are available within the energetic region of the modes [114, 121–128]. The mode spacing is depending on the MP diameter. For a high density of QDs, the modes are fully excited and their quality factor can be measured at the transparency EPD [129]. If the energetic detuning between the fundamental mode and the QD ensemble is large enough, just a few QDs are coupling to the modes [130, 131], which are then

not fully spectrally filled and consequently reflect the FWHM of the coupling QDs. If no QD is coupling to the modes, no mode behavior at all can be observed.

4.1.1. Mode investigations

Several MPs with diameters ranging from 1 to 5 µm have been investigated by µ-PL measurements in order to determine the quality factors and mode signatures of these pillars. Additionally the expected mode energies and the mode-field distribution have been theoretically calculated by W.-M. Schulz using a transfer-matrix model including the lateral confinement [61]. Some results of this calculation are plotted in Figure 4.2. On the left side, a measured mode spectrum of a 2.1 µm MP is displayed along with the calculated mode energies. On the right side, the mode energies of the fundamental and higher modes are displayed for different pillar diameters, the black dots represent the measured mode energies while the lines reflect the calculated mode energies. The inset depicts the measured *quality factors* of the different pillars.

The mode field distribution for a 2 µm diameter MP was obtained by using the CCD-camera attached to the spectrometer without vertical binning, therefore a one-dimensional image of the mode intensity distribution for several energetically separated modes could be measured. The result of the mode calculations and the measured mode-field distribution is depicted in Fig. 4.3. The calculations and the measured data are in excellent agreement. A detailed discussion of the calculations and measurements can be found in [61].

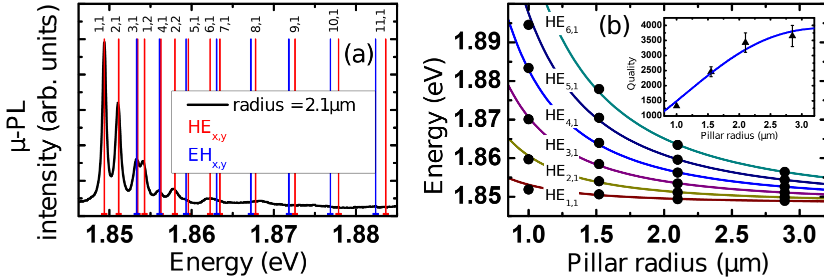

Figure 4.2.: (**a**) Mode spectrum of a 4.2µm MP with calculated modes. (**b**) Mode energies for different MP radii and their measured quality factor. (Calculations by W.-M. Schulz [61])

4.1.2. Single-Photon Emission

In order to find energetically well separated QD luminescence lines, µ-PL-measurements on several MPs have been performed. MPs have been chosen, which were on a sample area where the expected fundamental mode of the MPs is detuned with respect to the QD ensemble luminescence maximum. In this spectral region the separation of small QDs was sufficiently large that single QDs could be addressed. Due to the low number of QDs emitting in this spectral region, the emission from the investigated MPs showed no mode behavior. In the following, an MP with a diameter of 2.6 µm containing an addressable energetically separated single QD will be discussed.

Power Dependent Measurements

To identify the emission lines of this QD, a series of µ-PL-spectra at different EPDs were measured. Fig. 4.4(a) shows nicely the typical power dependence of the X and XX luminescence intensity. At low EPDs of 3 W/cm^2 the X luminescence is clearly dominant.

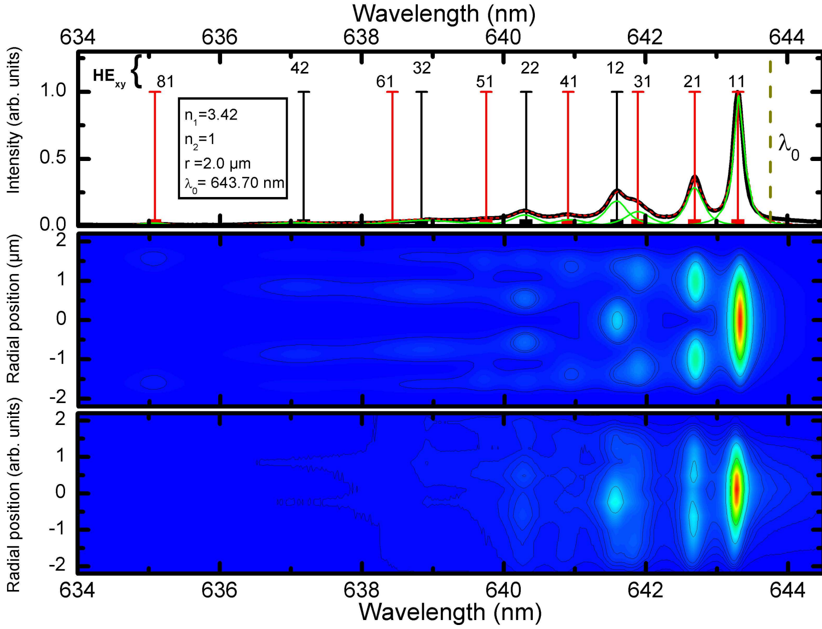

Figure 4.3.: (**upper**) Mode spectrum of a 2 µm diameter MP with calculated mode energies. (**middle**) Calculated mode field intensity is color-coded over radial spatial position and energy. (**lower**) Measured mode field. (Mode calculation by W.-M. Schulz [61].)

Detailed analysis of the X and XX show a super-linear increase of the XX intensity with increasing EPD, leading to dominantly biexcitonic decay at high EPDs above 150 W/cm^2 while the excitonic emission line saturates and than decreases due to the raising probability of higher numbers of e–h pairs in the QDs. This typical power-dependent behavior and the XX binding energy of $\approx$7 meV allows to clearly identify the X and XX decay channels. For higher pump powers $\geq$600 W/cm^2 additional luminescence

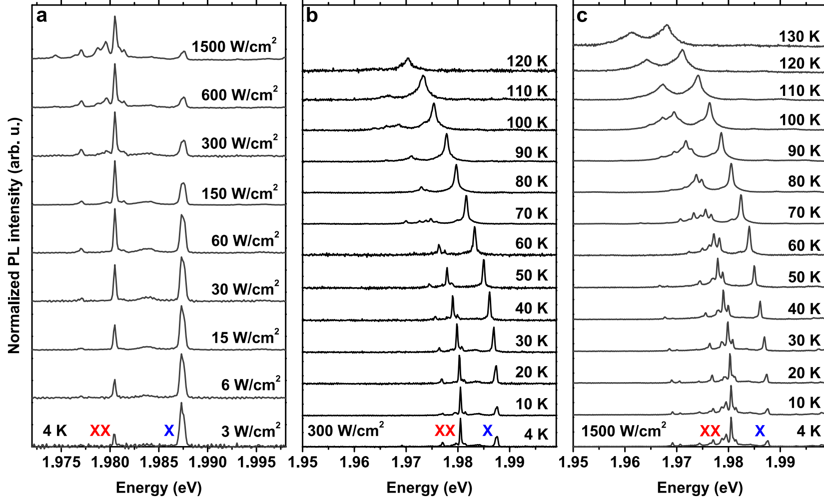

Figure 4.4.: **(a)** Normalized excitation power dependent spectra at $T = 4\,\mathrm{K}$. **(b,c)** Temperature dependent µ-PL-measurements on a single QD in a MP with an EPD of 300 and $1\,500\,\mathrm{W/cm^2}$.

lines around the XX line are observed, which can be attributed to multi-excitonic [132] and/or charged multi-excitonic transitions, where additional charge carriers in higher shells of the QD are present [133].

Temperature Dependent Measurements

The temperature dependence of the QD luminescence has been investigated in a range from 4 to 120 K (130 K) for EPDs of $300\,\mathrm{W/cm^2}$ ($1\,500\,\mathrm{W/cm^2}$), respectively (Figure 4.4(b,c)).

The typical red shift observable in Fig. 4.5(b) with increasing temperature reflects the gradual decrease of the band-gap due to an phonon-induced increase of the mean lattice-constant and

is analyzed in detail with an O'DONNEL-like fit (Eqn. 2.35) yielding an average phonon energy $\langle \hbar\omega \rangle = 12 \pm 2\,\text{meV}$ which corresponds to the GaInP TA–phonon (11.2 meV) (See Fig. 3.3).

For this type of QDs, the effect of e–h pair trapping into an optically forbidden excitonic DS has been demonstrated to have strong influence on the decay dynamics [67]. Starting at low temperatures (4 K) under the conditions of moderate (Fig. 4.4(b)) or strong (Fig. 4.4(c)) excitation the XX decay signal is found to dominate the emission spectra. This can be interpreted as a consequence of the interplay of initial multi-carrier occupation in combination with subsequent BS depopulation into the competing DS at 4 meV lower energy [67]. Consequently, for these conditions, the X luminescence is strongly suppressed.

At fixed EPD but increasing temperature, we observe a gradual revival of the BS excitonic µ-PL intensity I_x, where $I_\text{x}/I_\text{xx} \geq 1$ above $T = 45\,\text{K}$. One can interpret this as a temperature-induced deliberation of trapped carriers back into the optically active BS by a spin-flip activation energy of $E_\text{flip} = k_\text{B}T = 3.9 \pm 0.5\,\text{meV}$ with $T = 45 \pm 5\,\text{K}$.

The intensities of the X and XX luminescence have been analyzed for the different temperatures and plotted logarithmically versus the inverse Temperature T^{-1} (Fig. 4.5(a)). Fits in an ARRHENIUS-like fashion (Eqn. 2.37) have been applied to the data revealing activation energies of $96 \pm 7\,\text{meV}$ and $80 \pm 8\,\text{meV}$ for the X and XX thermal quenching. The Inset in Fig. 4.5 shows a zoom on the kink around $T^{-1} = 0.015\,\text{K}^{-1}$ to better display the dense data points in this thermal region. The obtained activation energies are in good agreement with the theoretical value of $\approx 90\,\text{meV}$ resulting from the barrier confinement at the given emission energy [134].

The FWHM of the X and XX luminescence lines has been investigated for the full temperature range (Fig. 4.6(a)). While at low

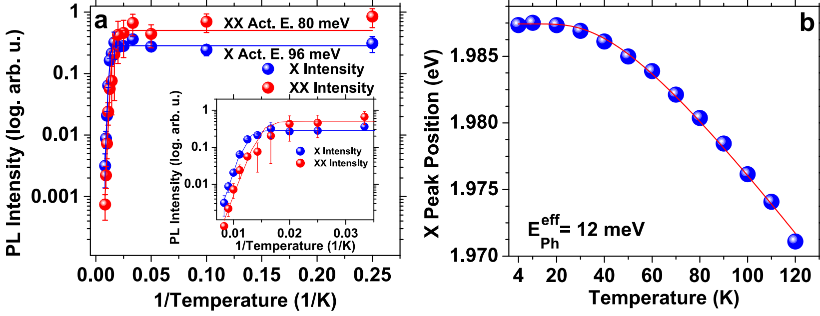

Figure 4.5.: **(a)** Temperature dependent analysis of the integrated X and XX intensities. ARRHENIUS-like fits are applied against the data, revealing activation energies for both lines (inset is a zoom on the kink). **(b)** Energetic position of the X luminescence for different temperatures with an O'DONNEL-like fit, yielding the effective phonon energy responsible for the band gap red-shift.

temperature, a fit via a LORENTZ-function is fully sufficient, an onset of a phonon sidebands becomes significant for temperatures above 30 K. Above 80 K this phonon sidebands are dominating the integrated intensity and the FWHM rises abruptly. Linear temperature coefficients for the broadening of the luminescence lines have been applied to the data revealing $a^{X} = 3.7 \pm 1\,\mu\text{eV}$ and $a^{XX} = 1.5 \pm 0.7\,\mu\text{eV}$ which is in good agreement with literature values [135, 136].

Time Resolved Measurement

In Fig. 4.6(b) the decay dynamics of the X and XX are displayed. The bi-exponential fits, applied to both transients, yield decay times $t_1^{X} = 0.33\,\text{ns}$, $t_2^{X} = 34\,\text{ns}$ and $t_1^{XX} = 0.46\,\text{ns}$, $t_2^{XX} = 3\,\text{ns}$ for the X and XX. The value of t_1^{X} is shorter than the value t_1^{XX}

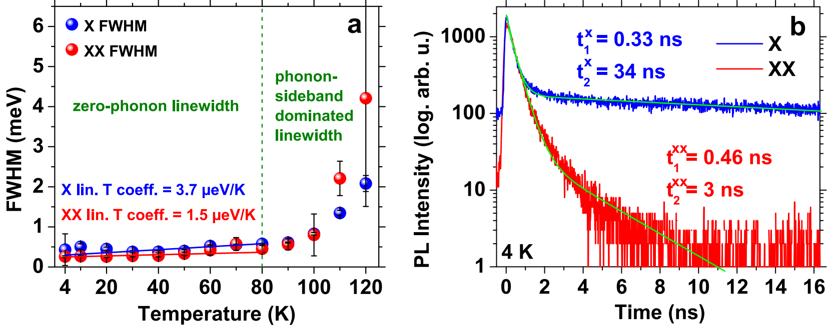

Figure 4.6.: **(a)** Temperature dependence of the X and XX FWHM. **(b)** Lifetime of the X and XX luminescence at 4 K.

despite the two decay channels of the XX. While the XX shows a quick bi-exponential decay, the X suffers from refilling out of the energetically lower DS. This indicates a strong tendency of the X BS to flip into the DS, what results in a shorter lifetime.

The slower component of the X lifetime $t_2^X = 34\,\text{ns}$ is longer than the repetition rate of the used laser $t_{\text{laser}} = 20\,\text{ns}$. Consequently, this strong refilling prohibits an on demand SP generation and the pulsed excitation character of an ACO measurement changes into a CW-like histogram (not shown here).

In order to obtain high-purity triggered single-photon emission, fast QD recombination dynamics, with respect to the laser pulse excitation cycle, is a necessary precondition. For the QD under study, only the XX decay is found to fulfill this requirement for low temperatures (see Fig. 4.6(b)).

Consequently, ACO measurements have been performed on the XX emission line of the QD from 20 to 80 K, depicted in Fig. 4.7(a–d). The peaks in the histograms are well separated without any indication for refilling. For the calculation of $g^{(2)}(\tau = 0)$

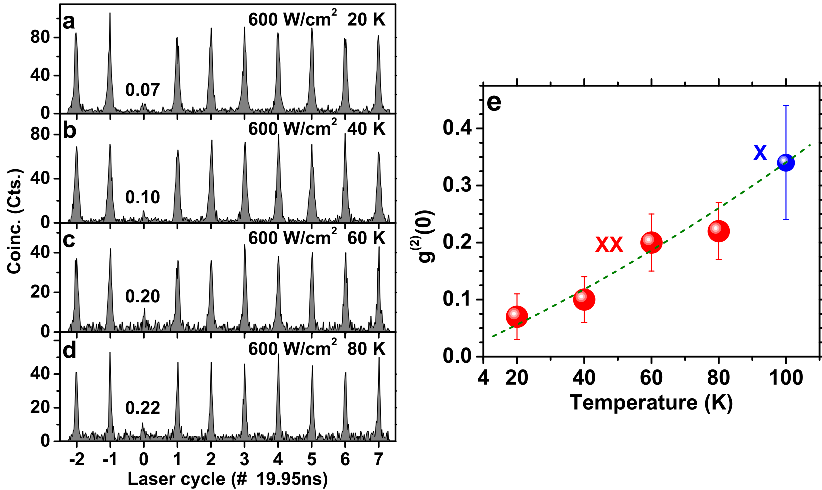

Figure 4.7.: (a–d) Temperature dependent auto-correlation measurements on the XX line (red) for temperatures of 20, 40, 60, and 80 K. The derived $g^{(2)}(0)$-values for these temperatures and for the X (blue) at 100 K (see Fig. 4.8) are compiled in (e), the green dashed line is a guide to the eye.

values (labels at the "zero"-delay peaks), a constant low noise level, mainly related to the detector dark counts, has been subtracted from the raw correlation data, whereas a correction for uncorrelated (Poissonian) µ-PL-signal background has not been performed. The $g^{(2)}(0)$ values for the XX are additionally assembled in Fig. 4.7(e).

With raising temperature, the amount of uncorrelated background below the auto-correlated XX and X luminescence lines raises, as a consequence the uncorrected $g^{(2)}(0)$ values are also raising in a range from 0.07 to 0.34, which is depicted in Figure 4.7(e) with a green dashed line as a guide to the eye.

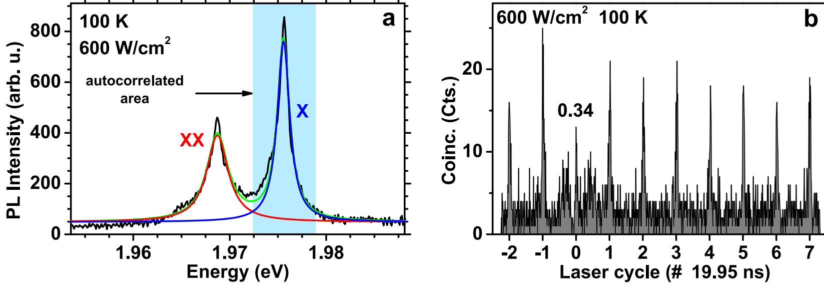

Figure 4.8.: *(a)* µ-PL-spectrum of the QD luminescence at 100 K with an EPD of 600 W/cm^2, the auto-correlated spectral range is shaded in blue. *(b)* shows the corresponding ACO histogram data on the X line at 100 K.

At high temperatures thermalization of BS and DS allows again a fast X recombination. At 100 K the XX luminescence is already more quenched and broader than the X luminescence (see Fig. 4.8(a)), and consequently an auto-correlation measurement on the X has been performed and resulted in a pulsed histogram again (Fig. 4.8(b)).

Figure 4.8(a) shows the µ-PL-spectrum at 100 K, the X and XX have just a slight energetic overlap. In this graph the spectral width, used for the auto-correlation measurement, is marked by a blue shaded box. On the right side in the figure, the obtained ACO histogram is displayed. The data showed in the histogram are not corrected for µ-PL background.

The $g^{(2)}(0) = 0.34$ value, printed in the graph, reflects the ratio of the zero-delay peak against the average of the other peaks, while the integration areas of the single peaks are all evenly chosen in a way that the clearly visible cross-talk features are left out.

To further analyze the reason for the not-vanishing value of $g^{(2)}(0)$, the signal to noise ratio of $\rho = S/(S+B) = 0.83 \pm 0.03$

was obtained from the µ-PL-spectra. If this ratio is taken into account a corrected value

$$g^{(2)}_{\text{corr.}}(0) = g^{(2)}(0) - \left(1 - \rho^2\right) = 0.03 \pm 0.02 \tag{4.1}$$

can be obtained, which comes very close to the theoretical value of zero for a single emitter. At this temperature, the spectral overlap of the XX within the X-FWHM is still not significant. With raising temperature, however, this overlap will raise and therefore influence the purity of the single photons. To investigate this effect at higher temperatures, a model has been developed which is discussed in Chapter 9.

4.1.3. Conclusion

The processing of MPs on the sample allowed the investigation of single, spectrally separated luminescence lines. EPD dependent µ-PL-measurements revealed clear signatures of X and XX from a single QD. QD luminescence could be measured up to a temperature of 130 K. Applied ARRHENIUS like fits to the integrated temperature dependent intensities of the X and XX emission lines revealed activation energies of 96 and 80 meV, respectively, corresponding well with the theoretical confinement energy of ≈90 meV. The zero-phonon FWHM was determined for the X and XX as 0.3 and 0.4 meV, and linear temperature coefficients of 3.7 and 1.5 µeV/K, respectively. From thermal activation of the X BS, a BS–DS splitting energy of 3.9±0.5 meV could be derived. A fitting of the temperature induced red shift yielded an average phonon energy of 12 meV, corresponding well to the GaInP TA–phonon (See eg. GaAs Fig. 2.12).

Time resolved measurements revealed decay times of the X and XX of $t_1^{\text{X}} = 0.33$ ns, $t_2^{\text{X}} = 34$ ns (caused by refilling from the DS) and $t_1^{\text{XX}} = 0.46$ ns, $t_1^{\text{X}} = 3$ ns. Autocorrelation measurements

have been performed up to 100 K resulting in $g^{(2)}(\tau = 0) = 0.34$, while it could be shown that the remaining multi-photon events arise from an uncorrelated photoluminescence (PL)-background. This states a temperature record at the time of writing this thesis and is published in [43]. Single-QD measurements including electrically pumped auto-correlations up to 80 K can be found in [44, 103, 134, 137].

4.2. Reduced Density Sample

For the investigated sample, InP-QDs in a $(Al_{33}Ga_{67})_{51}In_{49}P$ barrier were grown, including 2.5 s of PH_3-flow interruption after the deposition of 2.1 mono-layers of InP at 610°C. This recipe was applied on an exactly oriented GaAs-wafer in order to reduce the nucleation sites resulting from steps on the wafer surface.

With this technique we could achieve a low QD-density of about $7.5\times10^8\,cm^{-2}$ (type-B) (average QD distance ≈ 385 nm) and $2.75\times10^9\,cm^{-2}$ (type-A) (average QD distance ≈ 190 nm), determined by atomic-force microscope (AFM) measurements, allowing to access a single, optically active QD by spectroscopy without the need of any processing steps. By scanning the sample with the DotHunter (DH) scanning routine, one could find energetically well separated QD luminescence lines.

In Figure 4.9(left) an ensemble PL spectrum is depicted, showing PL of the GaAs substrate at ≈ 1.52 eV, followed by large and small QDs located energetically at ≈ 1.65 eV and ≈ 1.85 eV, respectively. The WL shows luminescence at ≈ 2.07 eV and the barrier at ≈ 2.13 eV.

InFig. 4.9(right), an AFM image of the sample surface is depicted, showing nicely the homogeneous distribution of type-A (big, white) and type-B (small, orange) QDs.

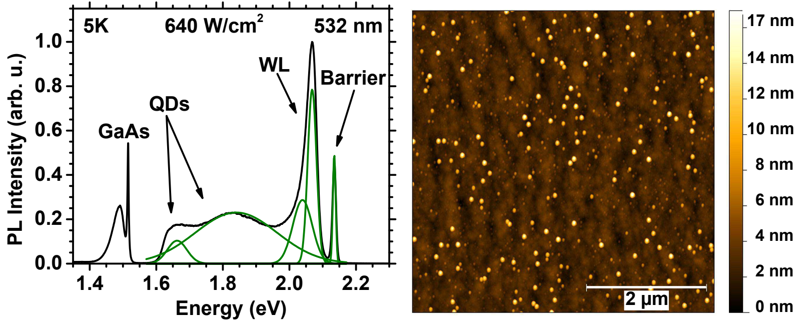

Figure 4.9.: (left) Ensemble PL-measurement performed with an EPD of 640 W/cm^2 at 5 K. The green lines are Gaussian fits to the ensemble, illustrating the overlapping of the different QD size distributions. **(right)** $5 \times 5\,\mu$m AFM image of an un-capped sample with identical growth parameters.

In order to identify the luminescence lines of the QDs, EPD dependent measurements have been performed. Fig. 4.10(a) shows the XX luminescence line at 4 K for EPDs ranging from 0.1 to 300 W/cm^2.

The integrated intensity of the visible luminescence line has been investigated for the given EPDs. The resulting data are plotted in Fig. 4.11(left) and a slope of 0.93 could be extracted. A slope of ≈ 1 indicates an X transition, but we will see that it is a XX luminescence line, which has a lower slope, due to a large DS–BS splitting energy and the low measurement temperature, see also Section 2.7.1 for a detailed explanation.

The identification of the QD lines is easily possible by investigating the luminescence behavior at higher temperatures. Figure 4.10(b) depicts the development of the QD luminescence with increasing temperature ranging from 4 to 130 K, here a transition from purely biexcitonic to purely excitonic luminescence can be ob-

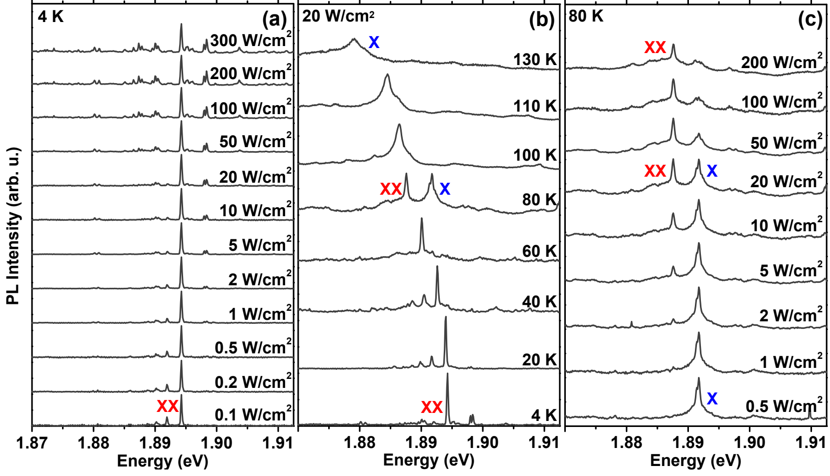

Figure 4.10.: Normalized EPD dependent µ-PL measurement of the QD at a temperature of 4 K **(left)**. Normalized temperature dependent µ-PL spectra at 20 W/cm^2 **(middle)** and normalized EPD dependent spectra at 80 K **(right)**.

served at $T \geq 80\,\mathrm{K}$ for a moderate EPD of $20\,\mathrm{W/cm^2}$. This allows an estimation of the BS–DS splitting energy via the transition temperature ($T = 80\,\mathrm{K}$) $E_{\text{flip}} = k_{\mathrm{B}}T \approx 6.9\,\mathrm{meV}$.

The power dependent intensity development at 80 K for EPDs between 0.5 and 200 W/cm^2 is shown in Fig 4.10(c), where we see the transition from X to dominantly XX PL around 20 W/cm^2. Out of this data one can again determine the slopes of the X and XX intensities versus the excitation power as displayed in Figure 4.11(right). Now, the measured slopes of 0.82 and 1.59 allow a clear identification of the luminescence lines as X and XX, respectively, resulting in an XX binding energy of 4.1 meV.

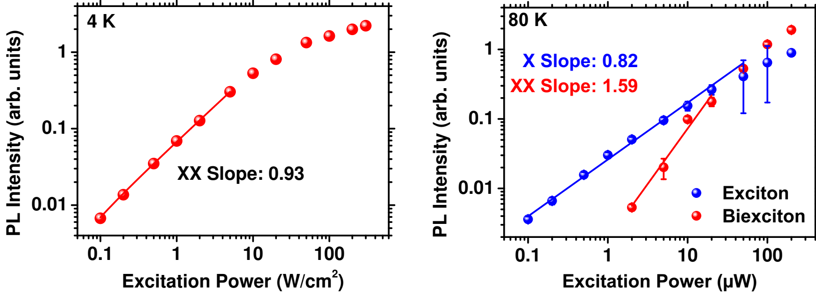

Figure 4.11.: (left) Excitation power dependent XX intensity at 4 K and **(right)** X and XX intensity dependency at 80 K.

4.2.1. Linewidth

The FWHM of the XX luminescence line has been investigated over three decades of EPD from 0.1 W/cm^2 up to 300 W/cm^2. The data from this analysis is displayed in Fig. 4.12(left). The FWHM has its minimum measured value at the lowest EPD of 0.1 W/cm^2 with an value of 0.2 meV and raises up to ≈0.24 meV at an EPD of 10 W/cm^2 and than stays constant up to the maximum EPD of 300 W/cm^2. Unfortunately, an EPD of 0.1 W/cm^2 is the lowest possible EPD, due to the resolution of the used power-meter in the setup. Additionally, a shoulder on the low energetic side of the X is visible, which might explain the high FWHM and can be attributed to a fine structure splitting of the luminescence line.

In the right graph of Fig. 4.12 the temperature dependence of the luminescence lines has been investigated. At temperatures ranging from 4 to 80 K the XX FWHM raises from 0.24 meV to 0.49 meV at an EPD of 20 W/cm^2. A fit via Eqn. (2.36) reveals an phonon energy responsible for the broadening of $E_{\text{Ph}} = 38 \pm 1$ meV and a linear coupling constant $\alpha = 0.9 \pm 0.04$ μeV/K. As a result of the fine structure splitting, the X line, becoming active at

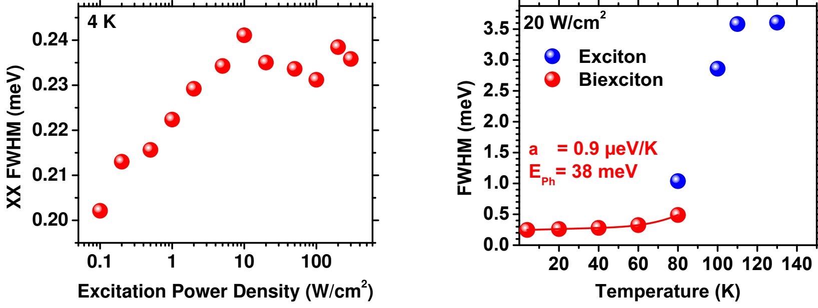

Figure 4.12.: (left) Excitation power density dependent XX FWHM at 4 K. **(right)** Temperature dependent FWHM of the X and XX at an EPD of 20 W/cm^2. For the XX an activation energy of $E_{\mathrm{Ph}} = 38 \pm 1$ meV and a linear coupling constant of 0.9 ± 0.04 µeV/K was found.

80 K at this EPD, is much broader and suffers from a strong onset of background luminescence at higher temperatures, see Fig. 4.10(middle). Therefore, it was not analyzed for an effective phonon energy.

4.2.2. Time Resolved Measurements

The decay dynamics of this sample revealed a strong carrier refilling effect, which has been analyzed via TCSPC measurements at different temperatures. Due to the fact, that the large BS–DS splitting energy allowed only the observation of the XX luminescence line at low temperatures, this line has been chosen for temperature dependent decay time studies.

In Figure 4.13(left) the histograms of the XX decay times for temperatures of 20 up to 130 K has been measured. A clear reduction of the fast decay time is visible between 20 and 60 K with raising temperature, while the slow decay time stays constant.

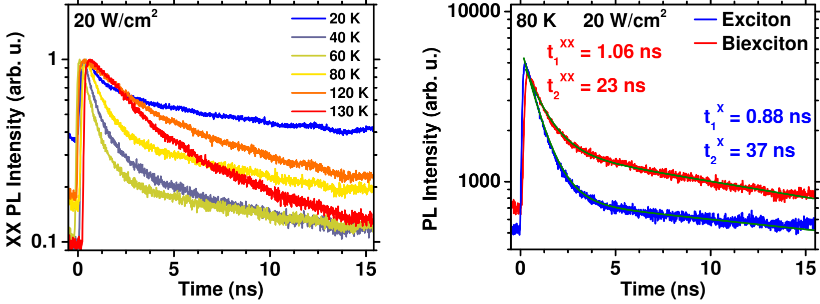

Figure 4.13.: (left) XX luminescence lifetime measurements performed at temperatures between 20 and 80 K with an EPD of 20 W/cm^2. **(right)** Direct comparison of the decay times of the X and XX at 80 K under an excitation power density of 20 W/cm^2.

Above ≈ 80 K the amplitude of the short decay time reduces strongly and the decay behavior becomes gradually nearly mono-exponential. Simultaneously the slow decay time, caused by refilling, decreases and nearly vanishes at 130 K, along with the luminescence. This effect can be attributed to an increasing loss of charge carriers out of the QD and a decrease of refilling due to thermal activation of charge carriers out of their potential traps. These traps might be related to the crystal defects found on the sample surface on top of the 30 nm barrier-layer, shown in Fig. 4.14.

On the right side of Fig. 4.13 a comparison of the decay times of X and XX luminescence is plotted under an EPD of 20 W/cm^2 at a temperature of 80 K. The shorter fast decay constant of the X of $t_1^X = 0.88$ ns in comparison to $t_1^{XX} = 1.06$ ns confirms a remaining probability for the X to flip and stay in the DS.

On this sample it was possible to perform a ACO measurement at a temperature of 110 K on the X luminescence line. The

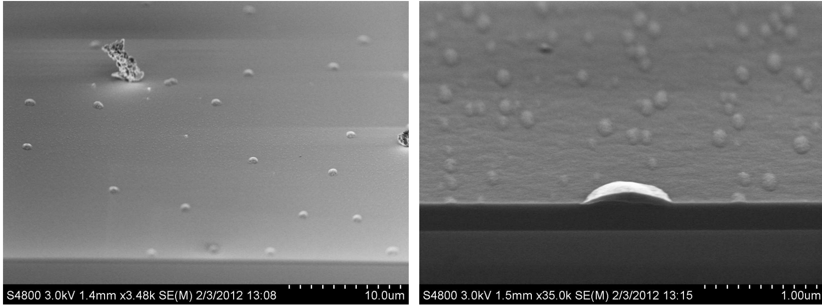

Figure 4.14.: SEM images of the sample. **(left)** Overview with clearly visible defects in a distance of ≈ 10 µm from each other. **(right)** Zoom-in on a defect at the edge of the sample. Capped QDs of various sized are visible behind the defect.

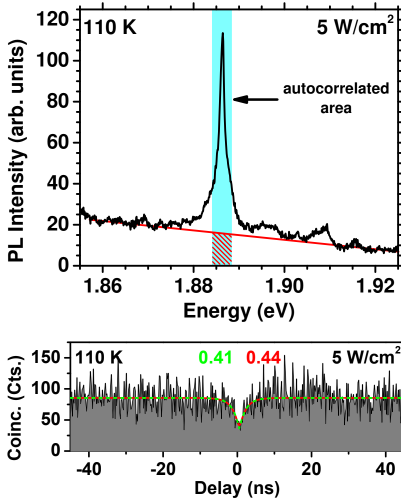

Figure 4.15.: µ-PL-spectrum of the QD at a temperature of 110 K with an EPD of 5 W/cm^2 **(top)** and according ACO-measurement under identical conditions **(bottom)**.
CW-like fits are applied to the ACO histogram: (red) uncorrected and (green) de-convoluted with the *apparatus function* of the setup. The numbers represent the derived $g^{(2)}(\tau = 0)$ values.

according µ-PL-spectrum is displayed in Figure 4.15(top), the excitation was performed in pulsed mode with an EPD of 5 W/cm^2.

The spectral region that was sent to the HBT-setup is marked by a blue shaded box, the significant Poissonian background is additionally marked by a red striped pattern within the auto-correlated spectral area.

In Fig. 4.15(bottom) the recorded ACO histogram is plotted. An CW-type fit, due to the CW-like character of the histogram, reveals a fully uncorrected $g^{(2)}(\tau = 0) = 0.44$ value. Up to the date of this thesis, this is the highest temperature ever measured on an InP-QD with $g^{(2)}(\tau = 0) < 0.5$.

A de-convolution of the fit with the *apparatus function* (See Sec. 2.5.5) reveals $g^{(2)}_{\text{deconv.}}(\tau = 0) = 0.41$. A correction for the red-marked Poissonian background (see Eqn. (2.29)) with an $\rho = 0.939$ calculated by the integration of the peak area and the background area, results in $g^{(2)}_{\text{corr.}}(\tau = 0) = 0.32$.

4.2.3. Conclusion

Using the optimized QD growth recipe for a reduced density enabled the measurement of single QD luminescence lines without further processing of the sample. At a temperature of 4 K only XX lines where found, with raising temperature ($\approx$80 K) the X DS began to thermalize, and X photon emission became observable, which could be identified by their excitation power dependency, revealing an XX binding energy of $\approx$6 meV. The BS–DS splitting energy was approximated to be $\approx$6.9 meV.

XX linewidths of $\approx$200 µeV have been found, which are broadened with raising temperature due to scattering with optical phonons of an effective energy of 38 ± 1 meV (close to the energy of an InP-like TO-phonon, see Fig. 3.3) and a linear constant $\alpha = 0.9 \pm 0.04$ µeV/K for the coupling to acoustical phonons at low temperatures.

The strong refilling effect could be reduced by raising the sample

temperature up to 60 K. It was possible to observe a suppression of multi-photon events down to $g^{(2)}_{\text{deconv.}}(\tau = 0) = 0.41$ at 110 K, which is the highest temperature measured for InP-QDs up to now.

4.3. Site-controlled InP Nucleation

Another type of sample structure was pre-processed with a regular hole-array before overgrowth, in order to allow site-controlled nucleation of InP-QDs. The structuring was carried out using micro-sphere photo-lithography after the deposition of a hexagonally close-packed mono-layer of polystyrene micro-spheres in a Langmuir-Blodgett-process. This process is described in Section 3.3.2.

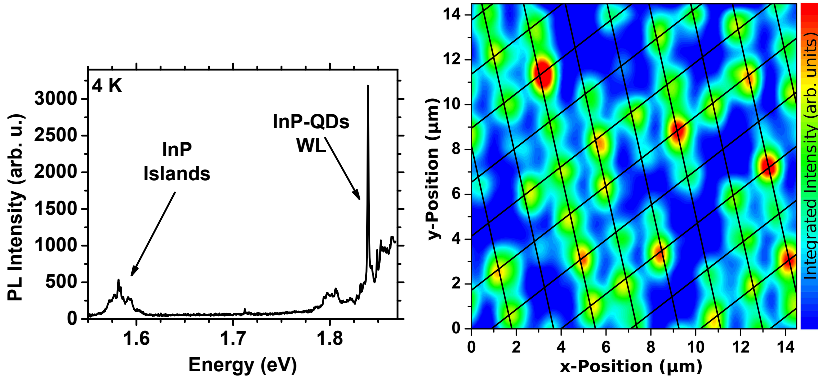

Figure 4.16.: (left) µ-PL overview spectrum recorded at 4 K, showing the InP-islands around 1.75 eV and QDs with WL onset above 1.8 eV. **(right)** Color coded µ-PL intensity map of a 15×15 µm area with a step width of 0.5 µm, showing the InP-island luminescence, black lines are guides to the eye [118].

To investigate the sample, a two dimensional map was recorded by scanning the sample with the DH program (described in Section A.1.1) with a step width of 0.5 µm over an area of 15×15 µm. The data was collected by in-situ analysis of the recorded spectra by the PeakFinder (PF) program.

The recorded intensity, collected in a range from 770–800 nm, is shown color coded in Figure 4.16(right). The regular intensity pattern, visible in this Figure results from InP islands, which are deposited at the etched sites on the sample in a distance of 2 µm. Their luminescence energy is $>$200 meV lower than expected for InP-QDs due to their larger size. Auto-correlation measurements showed no signature of anti-bunching, confirming the assumption that these structures do not have a zero-dimensional character. In between these islands, randomly located QDs have been found, their luminescence is depicted in a µ-PL overview spectrum (Fig. 4.16(left)) [118].

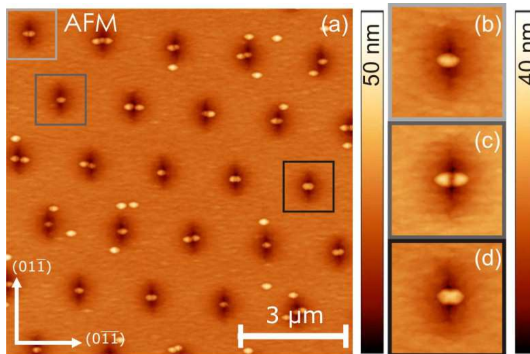

Figure 4.17.: Height signal of an AFM scan performed on the site-controlled InP-islands sample with a 3 nm GaInP cap-layer, (b-d) are magnified images of the marked areas [118].

A reduction of the offered QD material amount in the growth process may reduce the size of the InP island down to a length scale of QDs. An AFM-image is displayed in Fig. 4.17, showing the nucleated InP-islands, covered by a 3 nm GaInP cap-layer. This approach is very interesting for further application of QDs, because it allows the precise positioning of single QDs inside of wave-guide structures or resonators.

4.4. Conclusion of the GaAs based samples

Maximum SP-emission temperatures for InP-QDs of up to 110 K have been shown on GaAs-based systems. Interestingly, the higher temperatures have been achieved on the sample with the reduced density recipe, owing a simple 33% Al containing barrier structure with a theoretically lower carrier confinement than the one used in the MP-sample. Table 4.1 lists some of the extracted values characterizing the InP-QD luminescence properties.

Sample	E (eV)	Γ (µeV)	$E_{\mathrm{bind}}^{\mathrm{XX}}$ (meV)	E_{flip} (meV)	t_1^{X} (ns)	$T_{\mathrm{max}}^{\mathrm{Lumi}}$ (K)	$T_{\mathrm{max}}^{g^{(2)}}$ (K)
MP	1.987	250	6.9	3.9	0.33	130	100
reduced density	1.894	200	4.1	6.9	0.88	130	110

Table 4.1.: Assembled optical properties of InP-QDs on the investigated GaAs based sample structures. $T_{\mathrm{max}}^{g^{(2)}}$ represents the highest temperature where a ACO measurement resulted in $g^{(2)}(\tau = 0) < 0.5$.

5. InP QDs on GaAs/Si Substrate

5.1. InAs QD-Strain-Layer

In this sample structure a super lattice (SL) of five layers of indium arsenide (InAs) QDs have been deposited in order to incorporate strain into the sample at which threading dislocations can bend and, in the best case, annihilate. A detailed description of the sample fabrication can be found in [105]. On top of this, standard InP-QDs embedded in a 10/20 nm $(Al_{20}Ga_{80})_{51}In_{49}P$/-$(Al_{50}Ga_{50})_{51}In_{49}P$ hetero-confinement barrier are deposited.

In Figure 5.1 an ensemble PL measurement of the sample is displayed. The excitation was performed by use of a CW laser at 514 nm with an EPD of $640\,W/cm^2$. The QD ensemble luminescence has its maximum at $\approx 1.7\,eV$ with an FWHM of $\approx 0.2\,eV$. At an energy of $\approx 1.9\,eV$ the WL and at $\approx 1.95\,eV$ the barrier luminescence is visible. At the low energetic side, a signature of InAs luminescence has been found which may originate from InAs-QDs or an InAs-WL. Additionally, no evidence of GaAs buffer luminescence can be found in the spectrum, indicating a high defect density within the buffer, leading to non-radiative decay channels.

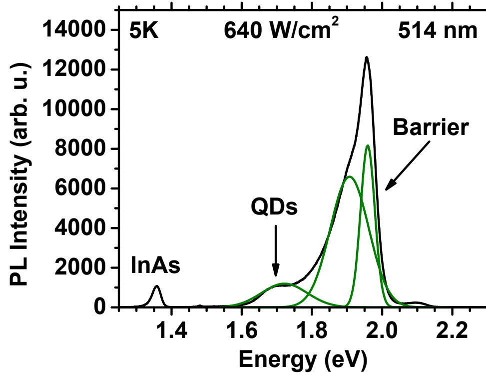

Figure 5.1.: Ensemble PL-measurement with an EPD of $640\,\mathrm{W/cm^2}$ at $5\,\mathrm{K}$ and an excitation wavelength of $514\,\mathrm{nm}$. The green lines are GAUSSian fits to illustrate the components of the spectrum.

5.1.1. Power Dependent Measurements

At the high energetic side of the QD ensemble single luminescence lines could be measured, Fig. 5.2 shows EPD dependent µ-PL spectra of a single QD.

Up to an EPD of $50\,\mathrm{W/cm^2}$ just a single line and a weak bump $4\,\mathrm{meV}$ higher in energy can be found. At higher EPDs a high energetic shoulder becomes visible, which probably is caused by multi-excitonic transitions [133]. Above $200\,\mathrm{W/cm^2}$ an additional signature $5\,\mathrm{meV}$ lower than the main peak arises. Both mentioned signatures do not show any indication to identify them as X or XX.

5.1.2. Temperature Dependent Measurements

The temperature dependent luminescence in a temperature range from 4 to $100\,\mathrm{K}$ of the same QD is depicted in Fig. 5.3. Also, in

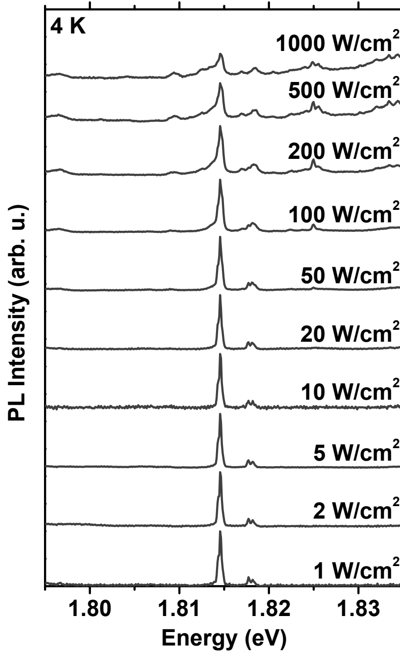

Figure 5.2.: EPD dependent µ-PL measurement of a single QD at EPDs ranging from 1 to 1 000 W/cm^2 at a temperature of 4 K.

this measurement no significant additional feature can be observed that would allow a clear identification of the observed luminescence line. This behavior was also found for other QDs on this sample. A comparison with the spectra shown in Fig. 4.10 indicates that the observed luminescence line may be a XX luminescence, separated from an energetically $\approx$3.6 meV higher and weak X feature.

The intensity of the luminescence line increases up to a temperature of 20 K and drops significantly at higher temperatures, accompanied by a strong spectral broadening. Unfortunately, an analysis to obtain an *activation energy* from the data was not possible.

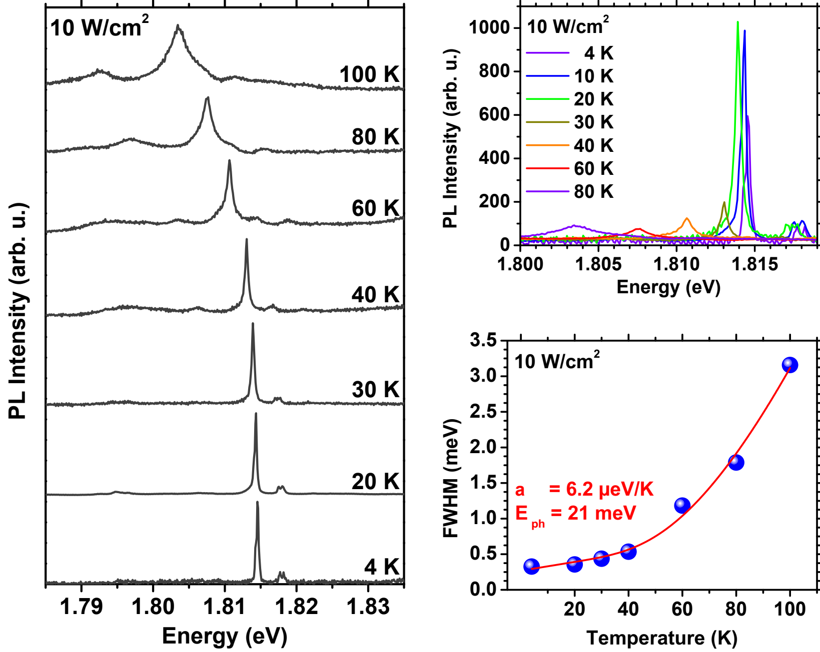

Figure 5.3.: (left) Temperature dependent µ-PL spectra of a single QD at an EPD of 10 W/cm^2 in a temperature range from 4 to 100 K. **(right top)** The spectra shown in the left graph normalized to a common integration time of 1 s. **(right bottom)** Temperature dependent FWHM with an applied fit (see Sec. 2.8.5) revealing an effective phonon energy of 21 ± 6 meV and a linear coupling constant of 6.2 ± 5.4 µeV/K.

The FWHM of the luminescence line revealed a linear coupling constant of $\alpha = 6.2 \pm 5.4\,\mu\text{eV/K}$ and an effective phonon energy of $E_{\text{Ph}} = 21 \pm 6\,\text{meV}$ by applying a fit via Eq. (2.36).

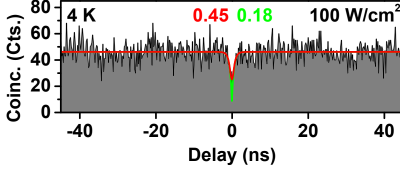

Figure 5.4.: ACO measurement at 4 K and an EPD of 100 W/cm^2 with an standard fit (red) and a de-convoluted fit (see Sec. 2.5.5) (green) applied, revealing $g^{(2)}(0) = 0.45$ and $g^{(2)}_{\text{deconv.}}(0) = 0.18$, respectively.

5.1.3. Time Resolved Measurements

The origin of the luminescence from a single QD could be proven by auto-correlating the signal at 4 K with an EPD of 100 W/cm^2 under pulsed excitation. The resulting histogram of the feature visible in Figure. 5.3 is shown in Figure 5.4. The red line represents the convoluted fit, while the green line is the same fit de-convoluted with the *apparatus function*, revealing $g^{(2)}(\tau = 0) = 0.45$ and $g^{(2)}_{\text{deconv.}}(0) = 0.18$, respectively.

5.1.4. Conclusion

The integration of five InAs-QD layers into the structure to implement strain into the system, still allowed the formation of InP-QDs with zero-phonon linewidths of $\approx$0.3 meV. But the raising intensity with temperatures up to 20 K indicates the presence of charge carrier traps, what can also be supported by the strong refilling effect visible in the ACO measurement. Also, the significant luminescence intensity drop at temperatures above 30 K which has been found for all measured QDs on this sample indicates the presence of non-radiative decay channels due to remaining threading dislocations. It was possible to show multi-photon event suppression down to $g^{(2)}_{\text{deconv.}}(0) = 0.18$, revealing a CW-like histogram, despite the pulsed excitation. The low count rates, especially at higher temperatures, did not allow further temperature dependent mea-

surements, though very weak µ-PL luminescence was detectable up to 100 K.

5.2. InGaAs/GaAs Super-Lattice

The incorporation of an InGaAs/GaAs SL introduces high strain at the InGaAs/GaAs interfaces, leading to a bending or even annihilation of the threading dislocations, what reduces the defect density from $\approx 1\times10^{11}\,\text{cm}^{-2}$ down to $\approx 1\times10^{9}\,\text{cm}^{-2}$ [105], at the surface of the SL a 1 µm GaAs-buffer, deposited above [138]. On top of this, standard InP-QDs embedded in a 10/20 nm $(Al_{20}Ga_{80})_{51}In_{49}P$/ $(Al_{50}Ga_{50})_{51}In_{49}P$ hetero-confinement barrier are deposited.

Nevertheless, the anti-phase domains (APDs) still remain in the system and are leading to internal electric fields at the anti-phase boundaries (APBs). A detailed description of the sample fabrication can be found in [105].

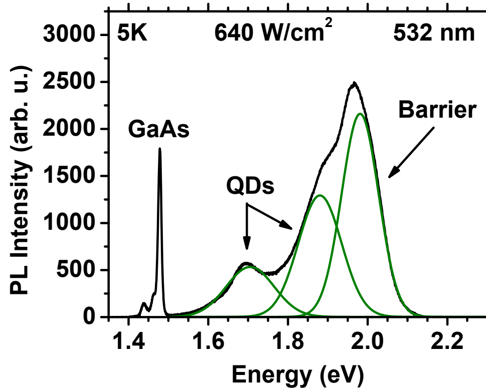

Figure 5.5.: Ensemble PL-measurement with an EPD of 640 W/cm^2 at 5 K and an excitation wavelength of 532 nm. The green lines are GAUSSian fits to illustrate the components of the spectrum.

In Figure 5.5 an ensemble PL measurement of the sample is displayed. The excitation was performed with a CW laser at 532 nm with an EPD of 640 W/cm^2. The QD ensemble luminescence has its maximum at ≈1.7 eV with an FWHM of ≈0.15 eV. At an energy of ≈1.87 eV the WL and at ≈1.95 eV the barrier luminescence is visible. At an energy of ≈1.48 eV the luminescence of the GaAs buffer is clearly visible and intense, what indicates a good crystal structure with a low defect density.

5.2.1. Power Dependent Measurements

At a temperature of 4 K detailed measurements on the luminescence of a single QD have been performed, Fig. 5.6(left) shows the EPD dependency of the X and XX luminescence lines which can be identified by their typical intensity development with increasing EPD, which is displayed in Fig. 5.6 (upper right). From this analysis, slopes for the X and XX of 1.02 ± 0.1 and 2.18 ± 0.24 have been derived. These slopes are in very good agreement with the theoretically expected values of 1 and 2 for the X and XX, described in Sec. 2.7.1.

Interestingly, the luminescence lines reveal a blue shift with increasing EPD, this behavior is quantitatively plotted in Figure 5.6(lower right). A strong increase of the luminescence energy is visible form 0.1 up to 20 W/cm^2, which then seems to slowly saturate towards higher EPDs with a full shift of nearly 700 µeV. Such a behavior can be explained by the compensation of a Stark-shift, induced by an internal electrical field, with increasing charge carrier density while raising the excitation power density, see also Sec. 2.8.4.

This blue shift has been found for many QDs luminescence lines on this sample and might be correlated with the existence of APDs in this sample. During the deposition of the GaAs-buffer,

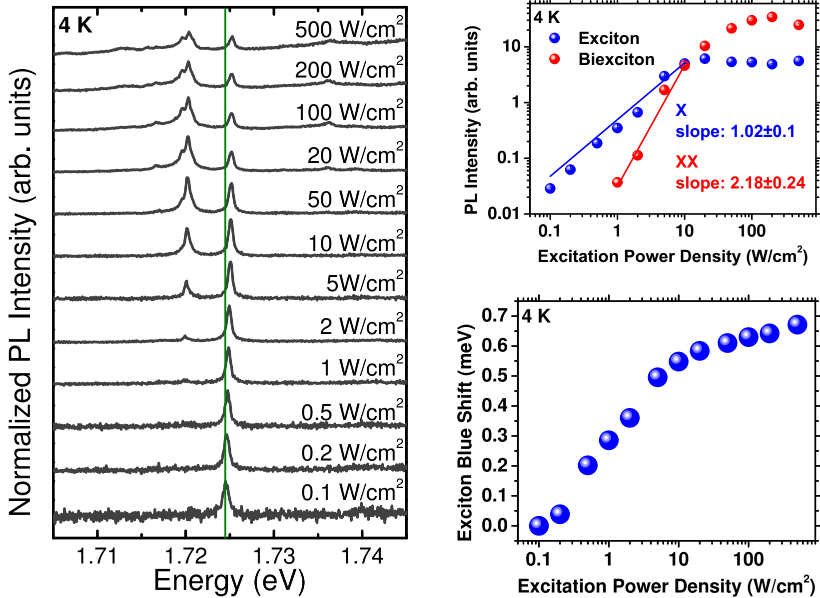

Figure 5.6.: (left) Normalized EPD dependent µ-PL spectra measured at 4 K with EPDs ranging from 0.1 to 500 W/cm^2. The green line is a guide to the eye, representing a constant energy. **(upper right)** EPD dependent blue shift of the X luminescence energy in the left pane. **(lower right)** EPD dependent integrated X and XX intensities, with fitted slopes at $T = 4\,\text{K}$.

the APDs are forming plateaus of around 10 nm in height on the GaAs-buffer surface. The edges of this plateaus may act as nucleation cites for the formation of QDs directly at the APBs and therefore at cites of high electrical fields. This formation process may explain an initial Stark-shift of the luminescence at low temperatures and low EPDs, while no additional charge carriers are in the system to cancel-out the electrical field.

5.2.2. Temperature Dependent Measurements

The QD luminescence could be investigated in a temperature range from 4 to 140 K, which is plotted in Fig. 5.7(left). Also, in this measurement, a slight blue shift between 4 and 20 K is visible, competing the typical temperature dependent red shift of the luminescence.

The possibility to measure single-QD luminescence up to a temperature of 140 K is very promising, but in this case the count rates of the QD luminescence, even at low temperatures, is quite low and therefore does not allow auto-correlation measurements at elevated temperatures.

Bandgap and effective Phonon Energy

From the red shift of the luminescence, effective phonon energies of 8.81 ± 0.56 meV and 8.75 ± 0.78 meV, consistent with the TA-phonon of an InP/GaInP mixture (See Fig. 3.3), could be derived from the mean lattice constant change by fitting of the data as described in Sec. 5.2.2.

Activation Energies

The reduction of the X and XX luminescence intensity with increasing temperature has been investigated by applying an Arrhenius-like fit (see Sec. 5.2.2) on the integrated intensities shown in Fig. 5.7(lower right). Here activation energies of $E_{\mathrm{A}}^{\mathrm{X}} = 17 \pm 3$ meV and $E_{\mathrm{A}}^{\mathrm{XX}} = 67 \pm 30$ meV have been found. The large error, especially on the XX activation energy, results from long integration times, due to low count rates and an upcoming background intensity which impeded an accurate focusing on the QD.

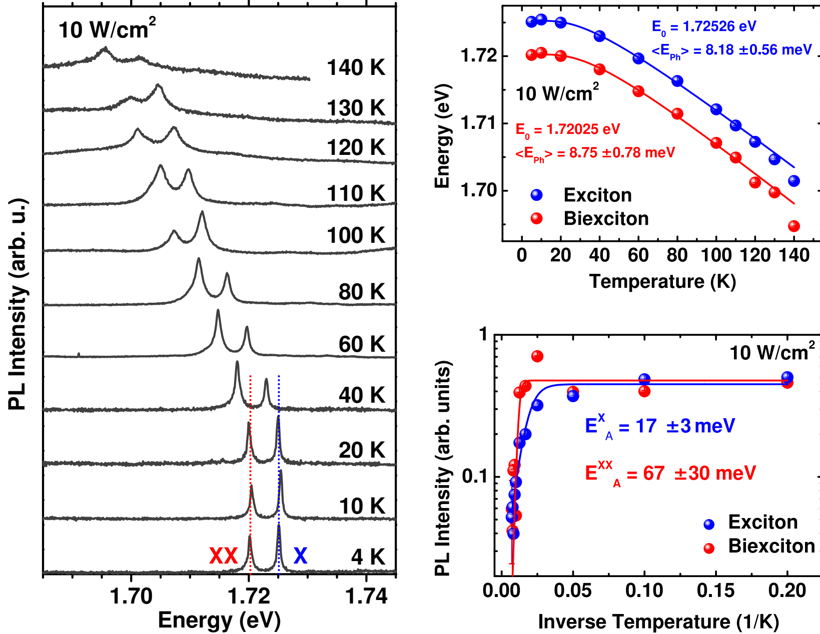

Figure 5.7.: (left) Normalized Temperature dependent µ-PL spectra measured at an EPD of 10 W/cm^2 within a temperature range of 4 to 140 K. **(upper right)** Temperature dependent spectral position of X and XX with an applied fit (Eq. (2.35)) revealing an effective phonon energy of ≈8.4 meV. **(lower right)** Temperature dependent intensities of X and XX resulting in activation energies of 17 ± 3 and 67 ± 30 meV, respectively. (Acquired via an Arrhenius-like fit, see Eq. (2.37))

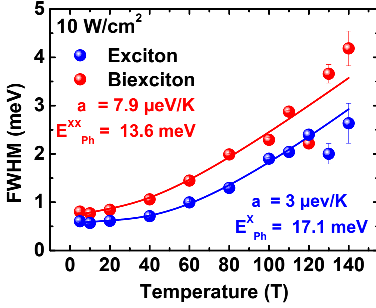

Figure 5.8.: Temperature dependent FWHM of the X and XX in a temperature range from 4 to 140 K with an EPD of $10\,\mathrm{W/cm^2}$, with fits, applied via Eqn. (2.36), revealing phonon energies of $E^{X}_{Ph} = 17.1 \pm 2\,\mathrm{meV}$ and $E^{XX}_{Ph} = 13.6 \pm 3.7\,\mathrm{meV}$ and linear coupling coefficients $\alpha^{X} = 3 \pm 2.5\mathrm{\mu eV/K}$ and $\alpha^{XX} = 7.9 \pm 2.4\mathrm{\mu eV/K}$.

Linewidth

The temperature dependent X and XX FWHM is depicted in Fig. 5.8. Consistently with the data derived in Sec. 5.2.2, the analysis of the X and XX FWHM via Eqn. (2.36) resulted in phonon energies of $E^{X}_{Ph} = 17.1 \pm 2$ and $E^{XX}_{Ph} = 13.6 \pm 3.7\,\mathrm{meV}$ and linear coupling coefficients $\alpha^{X} = 3 \pm 2.5\mathrm{\mu eV/K}$ and $\alpha^{XX} = 7.9 \pm 2.4\mathrm{\mu eV/K}$. The minimal FWHM was found for the X line at 10 K with a value of 570 µeV.

5.2.3. Time Resolved Measurements

On this QD the temperature and excitation power density dependency of the decay times has been investigated. The measurements revealed a strong refilling effect in the luminescence of the X and XX, therefore temperature and excitation wavelength variation have been utilized in order to suppress the refilling effect.

Temperature Dependence Time-correlated single-photon counting has been performed on the X and XX luminescence line, depicted in Figure 5.9(left) and (right), respectively. The X decay characteristic is strongly influenced by temperature, its short decay

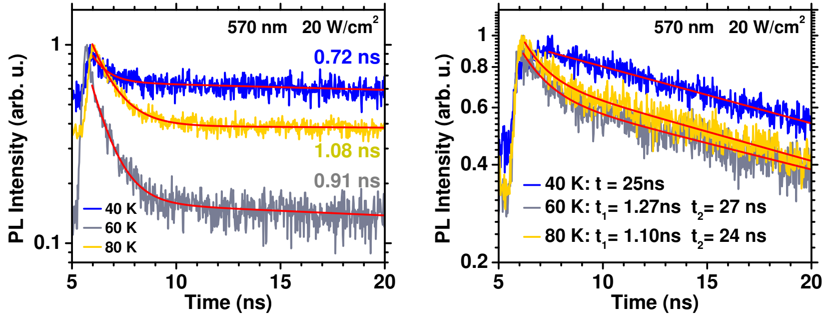

Figure 5.9.: Temperature dependent decay time measurements, with an excitation wavelength of 570 nm and 50 W/cm^2 EPD at temperatures of 40, 60, and 80 K for the X **(left)** and XX **(right)** (µ-PL-spectra in Fig. 5.7(left)).

time t_1 raises from 0.72 ns at 40 K up to 0.91 ns at 60 K. Simultaneously the *amplitude* of the long, refilling induced, decay constant decreases strongly up to 60 K and then revives towards higher temperatures, see Fig. 5.9(left). The XX decay dynamics are less influenced by temperature, but nevertheless a change from a very slow mono-exponential decay of $t = 25$ ns to a bi-exponential decay with a short decay time of $t_1 = 1.27$ ns ($t_1 = 1.1$ ns) for 60 K (80 K) can be observed.

Excitation Wavelength Dependence An investigation of the excitation wavelength dependence of the decay characteristics has been performed for wavelengths between 500 and 610 nm. The resulting histograms are plotted in Fig. 5.10(left). Here, no clear dependency of the short decay time t_1 can be observed, t_1 stays relatively constant at 0.8 ± 0.12 ns, while the intensity of the refilling effect drops slowly towards 610 nm, but still stays significantly high.

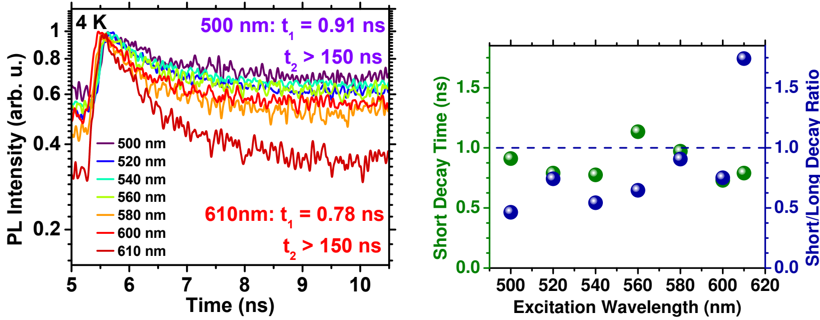

Figure 5.10.: Excitation wavelength dependent X decay time measurements, **(left)** histograms, **(right)** resulting values for the X short decay time t_1 (green) and the ratio of the short/long decay amplitudes (blue) at 4 K and excitation wavelength between 500 and 610 nm and an EPD of 50 W/cm^2 (µ-PL-spectra in Fig. 7.2(left)).

Excitation Wavelength Dependent Auto-correlation The influence of different excitation wavelength on the photon statistics of the X has been investigated for excitation wavelength of 570 nm and 600 nm and an EPD of 20 W/cm^2. Keeping the EPD constant for different wavelengths results, however, in different excitation situation due to the more efficient charge carrier generation at lower excitation wavelengths. Figure 5.11(right) shows nicely the blue shift of the emission line with increasing excitation energy as well as an upcoming PL-background. The auto correlated X peaks are marked with arrows. Obviously, the XX feature does not show the same shift as the X, this may result from a higher carrier density at the lower excitation wavelength and therefore a renormalization of the transition energy [92, 133].

The two graphs in Fig. 5.11(left) show the according auto correlation histograms, the top one with an excitation wavelength of 570 nm resulting in $g^{(2)}(\tau = 0) = 0.42$. Below, the

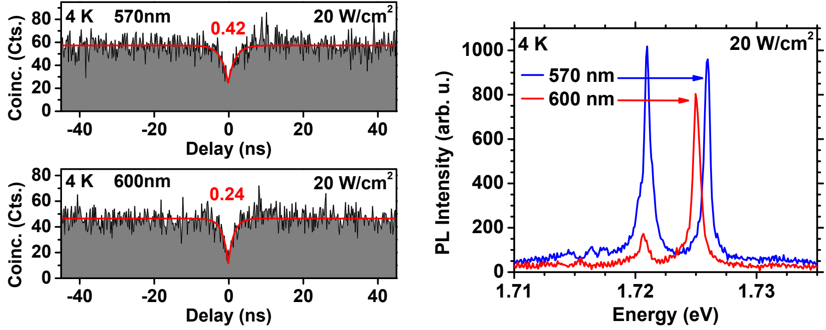

Figure 5.11.: Auto-correlation histograms of the X in Fig. 5.6(left) at $T = 4\,\mathrm{K}$ and an EPD of $20\,\mathrm{W/cm^2}$ under pulsed excitation (20 ns repetition rate) with an excitation wavelength of 570 nm **(top left)** and 600 nm **(bottom left)**. **(right)** Corresponding µ-PL-spectra of the auto-correlated features, marked with arrows.

same luminescence line was auto-correlated under excitation with 600 nm photons at the same nominal EPD of $20\,\mathrm{W/cm^2}$. Here the $g^{(2)}(\tau = 0) = 0.24$ is lower, what can be attributed to a lower Poissonian PL-background. The fits applied to the data are for CW excitation, due to the CW-like histograms that are arising, despite the pulsed excitation, see Eq. (2.27).

5.2.4. Conclusion

The strain introduced by an InGaAs/GaAs strained super-lattice should reduce the density of threading dislocations remaining at the surface of the GaAs buffer. Zero-phonon linewidths of $\approx 0.6\,\mathrm{meV}$ have been found in connection with effective phonon energies of $\approx 8.3 \pm 1.7\,\mathrm{meV}$ and $\approx 13.1 \pm 1.3\,\mathrm{meV}$, which can be attributed to the TA-phonon of InP and GaInP, respectively (See Fig. 3.3). Similar phonon energies have been derived from the

temperature dependent red-shift (8.75 ± 0.76 meV and 8.18 ± 0.56 meV for the X and XX lines, respectively). Excitation power density dependent measurements showed clear X-XX intensity slopes, very close to the expected theoretical behavior. On all measured QDs on this sample a power dependent blue-shift was found, resulting from an initial *quantum confined* STARK-*effect* at low temperatures and EPDs, which may be related to APDs building up internal electric fields at their APBs. Additionally, strong refilling was found and could be slightly suppressed by lowering of the excitation wavelength or raising the temperature. The luminescence intensity dropped rapidly at a temperature of 60 K revealing activation energies of 17 ± 3 meV and 67 ± 30 meV for the X and XX, respectively. Autocorrelation measurements at 4 K resulted in $g^{(2)}(\tau = 0) = 0.42$ and $g^{(2)}(\tau = 0) = 0.24$ at pulsed excitation with an wavelength of 570 nm and 600 nm, respectively. The better $g^{(2)}(\tau = 0)$ value results from a lower background luminescence level at lower excitation energy. From these findings one can deduce an significant density of remaining threading dislocations and APDs.

6. InP QDs on GaAs/GeVS/Si Substrate

To tackle the problem of threading dislocations, the miscibility of Si and Ge can be utilized to overcome the lattice mismatch between Si and GaAs by gradings or diffusion processes at the annealing steps of multi-layer growth [139]. To build up the germanium virtual substrate (GeVS), first a Si buffer layer was deposited on a Si wafer, followed by Ge in three layers by MBE, each of them followed by a high-temperature annealing step. These annealing steps considerably reduce the density of threading dislocations, resulting in a defect density at the GeVS surface of $1 \times 10^7\,\mathrm{cm}^{-2}$, at a total thickness of the virtual substrate of 450 nm [140]. On top of the GeVS, the GaAs buffer was grown by MOVPE in a two-step growth mode, starting with a 50 nm nucleation layer grown at 475°C, followed by growth at standard temperatures.

The growth of GaAs on Ge suffers from a strong segregation behavior of Ge, which acts as a n-type dopant in GaAs. In order to suppress the segregation process, the first 500 nm of the GaAs buffer are grown at a temperature of 600°C, resulting in a compromise between crystal quality and an inhibition of segregation. Afterwards, 500 nm GaAs at a standard growth temperature of 700°C were grown. On top of this, standard InP-QDs embedded in a 10/20 nm $(Al_{20}Ga_{80})_{51}In_{49}P/(Al_{50}Ga_{50})_{51}In_{49}P$ hetero-confinement barrier are deposited. A detailed description of the sample fabrication can be found in [105].

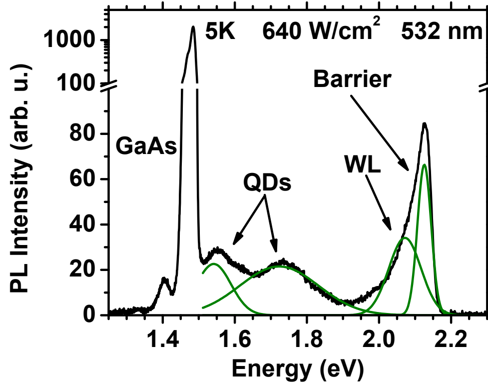

Figure 6.1.: Ensemble PL-measurement with an EPD of 640 W/cm^2 at 5 K and an excitation wavelength of 532 nm. The green lines are GAUSSian fits to illustrate the components of the spectrum. The vertical axis is split and the upper part is in logarithmic scale.

In Figure 6.1 an ensemble PL measurement of the sample is displayed. The excitation was performed with a CW laser at 532 nm with an EPD of 640 W/cm^2. On this sample two relatively weak QD ensembles have been found with their maxima at $\approx$ 1.55 eV and $\approx$ 1.75 eV with an FWHM of $\approx$ 0.1 eV and $\approx$ 2 eV, respectively. At an energy of $\approx$2.15 eV the WL and at $\approx$2.13 eV the barrier luminescence is visible. At an energy of $\approx$1.48 eV the luminescence of the GaAs buffer is very intense, what indicates a good crystal structure with a low defect density.

6.1. Power Dependent Measurements

Excitation power dependent µ-PL measurements have been performed on the sample in order to identify the QD luminescence lines. At a temperature of 4 K just a single line (with a small

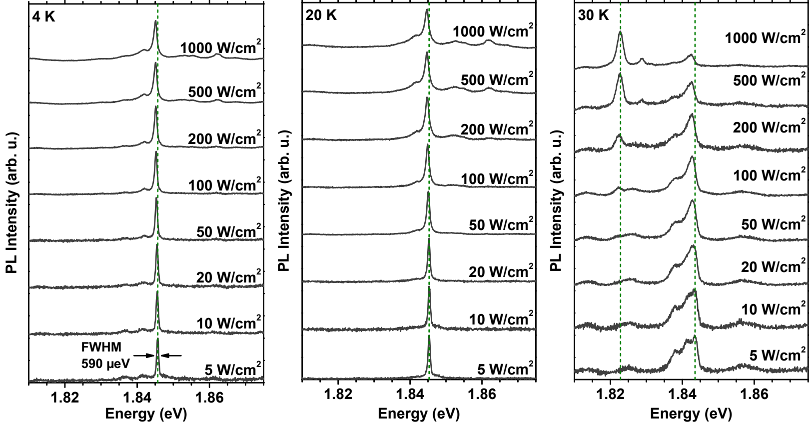

Figure 6.2.: Normalized power dependent µ-PL spectra with an EPD rang from 5 to 1 000 W/cm^2 at 4 K **(left)**, 20 K **(middle)**, and 30 K **(right)**.

3 meV lower energetic shoulder) is visible in an EPD range from 5 to 1 000 W/cm^2 which shows a small EPD-dependent red shift (Fig. 6.2(left)), illustrated by a dashed green line at constant energy. The integrated intensities of both components at 4 K is plotted double-logarithmically versus the EPD in Fig. 6.3, revealing slopes derived via Eq. (2.33) of 0.53 and 1.1 — which are both half of the theoretically expected values for an X–XX complex. At a temperature of 20 K (Fig. 6.2(middle)) the small low energetic shoulder becomes more visible at EPDs above 50 W/cm^2 and gains intensity relative to the main peak.

At 30 K (Fig. 6.2(right)), however, the shoulder is more intense at low EPDs and the intensity of both components reduces in favor for a 20 meV lower energetic line, showing a typical EPD dependent X–XX intensity behavior. Unfortunately, the determination of the slopes is not possible for this temperature, due to the already

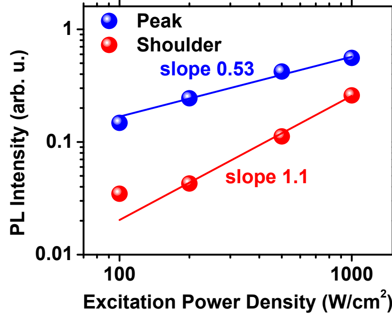

Figure 6.3.: Double-logarithmic EPD dependent integrated peak and shoulder intensities of the luminescence peak in Fig. 6.2(left), revealing slopes (see Sec. 2.7.1) of 0.53 and 1.1 for the peak and shoulder, respectively.

decreasing intensity of the high energetic complex in the measured EPD range. Therefore, it is not possible to clearly identify the luminescence lines, but a XX binding energy of 3 meV could be possible. For other measured QDs on this sample, also just single lines with a similar shoulder and very weak signatures $\approx$20 meV energetically below were found.

6.2. Temperature Dependent Measurements

The luminescence intensities of all measured QDs was very low and suffered from an early temperature dependent quenching. To illustrate this behavior, temperature dependent µ-PL spectra are plotted in Fig 6.4 at two EPDs of 10 W/cm^2 (left) and 100 W/cm^2 (right) for temperatures of 4, 20, and 30 K. In this case the spectra are normalized to a common integration time of 1 s, in order to allow a comparison of the intensities.

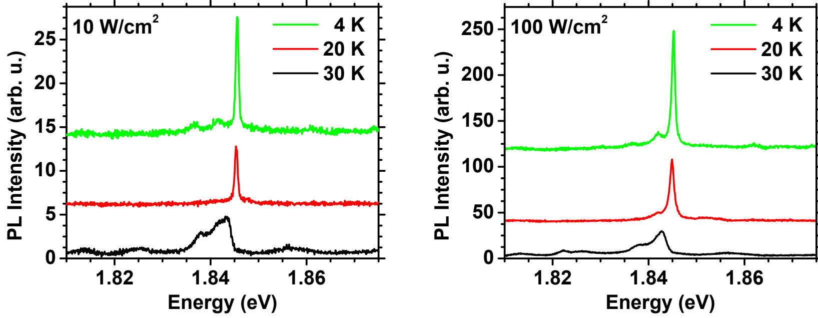

Figure 6.4.: Temperature dependent µ-PL spectra with an EPD of $10\,\mathrm{W/cm^2}$ **(left)** and $100\,\mathrm{W/cm^2}$ **(right)**. Spectra vertically shifted for enhanced clarity.

6.2.1. Time Resolved Measurements

TCSPC Measurements Despite the strong decrease of intensity with raising temperature, it was possible to measure the decay constants for the luminescence line in Fig. 6.4(right) up to 30 K. Figure 6.5 shows the TCSPC measurements for 4 K, 20 K, and 30 K (top, left, right). From this measurement a decrease of the decay time from 1.23 ± 0.01 ns at 4 and 20 K down to 0.76 ± 0.02 ns at 30 K has been derived. A possible explanation of this behavior could be that a higher charge carrier mobility may lead to multi-excitonic transitions, which have a faster decay constant [69, 70], and that the onset of thermal quenching is leading to a non-radiative loss of charge carriers out of the QD, which both would lead to a faster decay of the luminescence.

Auto-Correlation Measurements A clear suppression of multi-photon events could be proofed by ACO measurements on the luminescence line in Figure 6.4(left). Figure 6.6 depicts this mea-

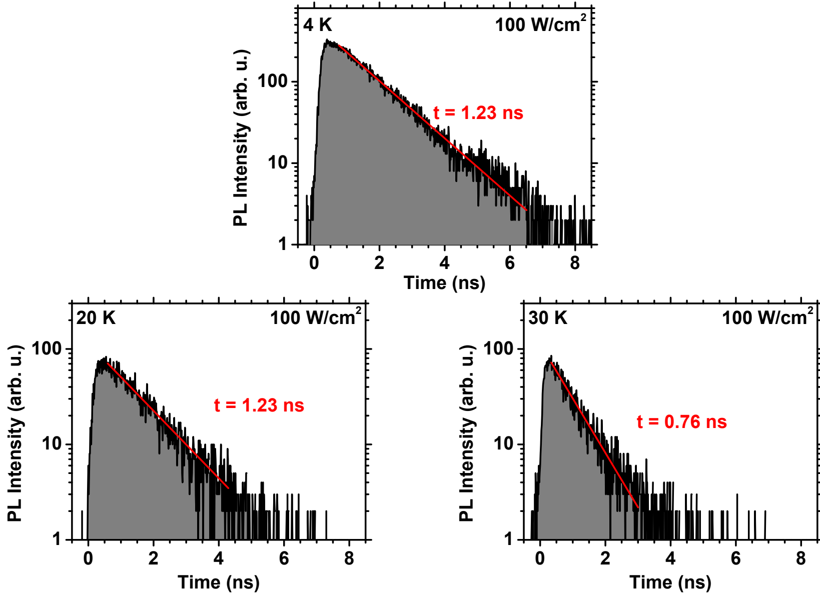

Figure 6.5.: Decay time measurements with exponential fits on the luminescence lines in Fig. 6.4(right) at an EPD of 100 W/cm^2 measured at a temperature of 4 K **(top)**, 20 K **(left)**, and 30 K **(right)**.

surement performed with an EPD of 100 W/cm^2 at a temperature of 4 K, allowing a derivation of $g^{(2)}(\tau = 0) = 0.32 \pm 0.03$. Unfortunately, the strong intensity decrease did not allow measurements at elevated temperatures.

No signature of refilling was found in the measurements on this sample. This is in full agreement with the TCSPC measurement shown above and may result from a strong defect reduction by the GeVS implemented in this sample structure, leading to a good crystal quality, consistent with the strong GaAs peak visible in Fig. 6.1.

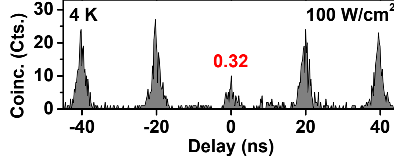

Figure 6.6.: Auto-correlation measurement on the luminescence line in Fig. 6.4(left) at an EPD of 100 W/cm^2 and $T = 4$ K.

6.3. Conclusion

The GeVS layer on this sample provided a very smooth surface and segregation of Ge during GaAs buffer deposition was successfully suppressed (analyzed by secondary ion mass spectrometry (SIMS) measurement [105]. Time resolved measurements revealed decay times of 1.23 ns at 4 K down to 0.76 ns at 30 K, without any carrier refilling effects. This is very promising for triggered SP generation.

SEM images of the GaAs buffer surface still showed APBs [105], but no blue-shift has been observed. This could be related to the low QD density of 2×10^9 cm^{-2} on the sample, measured by AFM [105], which allowed µ-PL access to single QDs within the inner region of the APDs. Therefore, the measured QDs are spatially separated from the APBs and consequently from the internal electric fields.

µ-PL measurements exhibit low background and linewidths of $\approx$590 µeV, however the luminescence intensity was extremely low and thermal quenching allowed only for µ-PL measurements up to 30 K.

Additionally, single QD luminescence lines have been observed, which revealed multi-photon suppression at 4 K with $g^{(2)}(\tau = 0) = 0.32 \pm 0.03$.

7. InP QDs on GaAs/GaP/Si Substrate

The deposition of an intermediate 46 nm thick GaP layer on a Si buffer located on the Si wafer may help to overcome the issue with the APDs described in Section 5. By first creating a Si-surface, containing only atomic double-steps, the formation of APDs in the GaP layer and the subsequent GaAs buffer is avoided [105, 141]. To achieve such a surface, the Si buffer is annealed for 30 min at 950°C under pure hydrogen atmosphere [141, 142].

For this sample, the lattice mismatch still remained for the subsequent GaAs buffer, but one can think of gradings from GaP directly to GaInP or AlGaInP, what is used as barrier material for the InP QDs anyway and may help to shrink the height of the buffer layer further down. The QDs are fabricated as described for the reduced density sample in the GaAs Section (see Sec. 4.2) with a $(Al_{33}Ga_{67})_{51}In_{49}P$ barrier. A detailed description of the sample fabrication can be found in [105].

In Figure 7.1 an ensemble PL measurement of the sample is displayed. The excitation was performed with a CW laser at 532 nm with an EPD of 640 W/cm^2. On this sample two QD ensembles have been found with their maxima at ≈ 1.57 eV and ≈ 1.67 eV with an FWHM of ≈ 0.1 eV and ≈ 1.5 eV, respectively. At an energy of ≈ 2.01 eV the WL and at ≈ 2.03 eV the barrier luminescence is visible. At an energy of ≈ 1.48 eV the luminescence of the GaAs buffer is not visible, what indicates a high defect

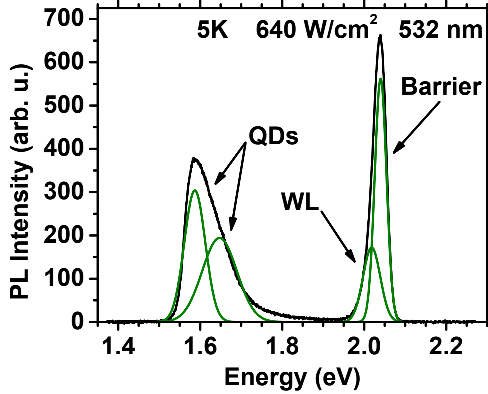

Figure 7.1.: Ensemble PL-measurement with an EPD of 640 W/cm^2 at 5 K and an excitation wavelength of 532 nm. The green lines are GAUSSian fits to illustrate the components of the spectrum.

density, resulting in non-radiative decay channels.

The InP QD epitaxial recipe is the same as used for the sample with reduced QD density, discussed in Section 4.2.

7.1. Power Dependent Measurements

The investigation of single QDs on this sample was possible without the need of any pre- or post-processing steps, due to the optimized density reduced QD-growth recipe (see Sec. 4.2). Figure 7.2(left) shows the normalized luminescence of a QD at 4 K for different excitation power densities ranging from 0.1 to 200 W/cm^2. At low powers, up to 5 W/cm^2 just the X luminescence is observable, at higher powers a XX complex becomes visible and finally some weak luminescence from QDs in the vicinity of the investigated QD.

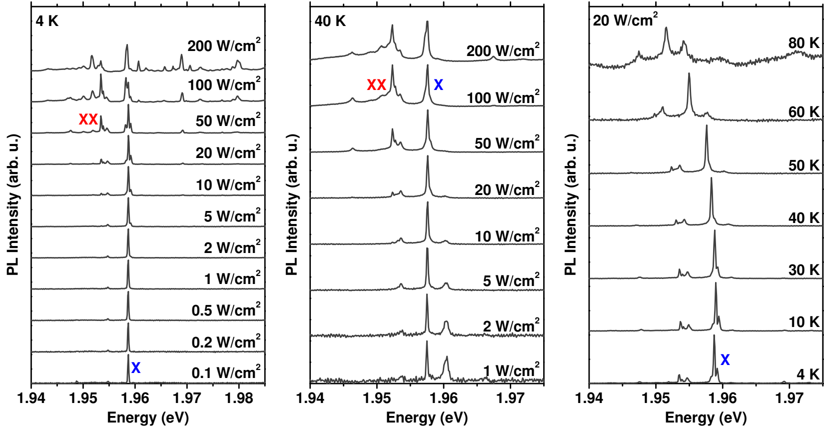

Figure 7.2.: **(left)** Normalized excitation power density dependent µ-PL-spectra recorded at 4 K for EPDs between 0.1 and 200 W/cm^2 and **(middle)** at 40 K. **(right)** Normalized temperature dependent µ-PL-spectra with an applied EPD of 20 W/cm^2 at temperatures ranging from 4 to 80 K. The excitation was performed at 570 nm.

In Figure 7.2(middle) the excitation power dependence of the QD was recorded at 40 K and shows a more pronounced XX luminescence.

Time Resolved Measurement

Time resolved measurement at low temperature revealed a strong refilling effect which is investigated in detail within this section. Figure 7.3 shows decay characteristics of the X luminescence under varied excitation power conditions. With increasing EPD the short decay time t_1 raises from 1.23 ns at 10 W/cm^2 to 2.16 ns at 50 W/cm^2, while the long decay time t_2 remains nearly constant and therefore the refilling persists. The significant delay of the

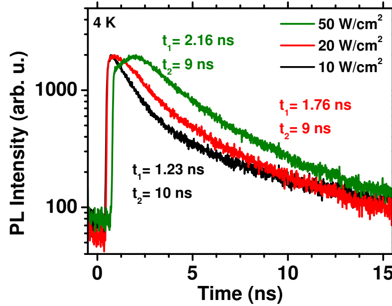

Figure 7.3.: Time resolved X intensity at 4 K under pulsed excitation with 10, 20, and 50 W/cm^2 excitation power density. The according spectra are shown in Fig. 7.2(left).

X luminescence at 50 W/cm^2 in comparison to the lower EPDs is caused by the XX–X cascade, which takes place at 50 W/cm^2 excitation power density, compare according spectra in Fig. 7.2(left) for the onset of the XX luminescence at this EPD.

7.2. Temperature Dependent Measurements

The (left) graph in Figure 7.4 displays the temperature dependence of the QD luminescence at an EPD of 20 W/cm^2 within an temperature range from 4 to 80 K of the spectra shown in Fig. 7.2(left). Above 60 K the intensity decreases massively and, in comparison to the QD features, a significant amount of background luminescence appears. From this data, thermal activation energies have been derived resulting in 6 and 114 meV.

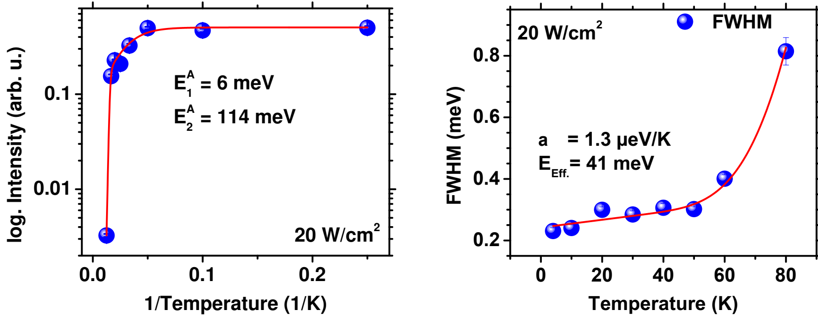

Figure 7.4.: (left) Integrated intensity over inverse temperature with an applied ARRHENIUS-like fit, revealing activation energies of 6 ± 3 and 114 ± 28 meV. **(right)** FWHM evolution with raising temperature, an applied O'DONNEL like fit (Eqn. (2.35)) results in an effective phonon energy of 41 ± 16 meV and a zero-phonon linewidth of 240 ± 20 µeV.

7.2.1. Linewidth

The thermal broadening of the X luminescence line has also been investigated and is plotted in Fig. 7.4 (right). From this data, a zero-phonon linewidth of 240 ± 20 µeV and an effective phonon energy of 41 ± 16 meV (corresponding to an InP-TO-phonon (see Fig. 3.3)) and a linear coupling constant of $\alpha = 0.8 \pm 0.3$ µeV/K could be derived by applying a fit discussed in Sec. 2.8.5, responsible for phonon-carrier scattering which results in a line broadening.

Time Resolved Measurement

The influence of temperature on the decay times has been investigated in a range from 4 to 80 K with an excitation wavelength of 570 nm and an EPD of 50 W/cm^2. The resulting decay curves are displayed in Fig. 7.5(left) with the according decay times (right).

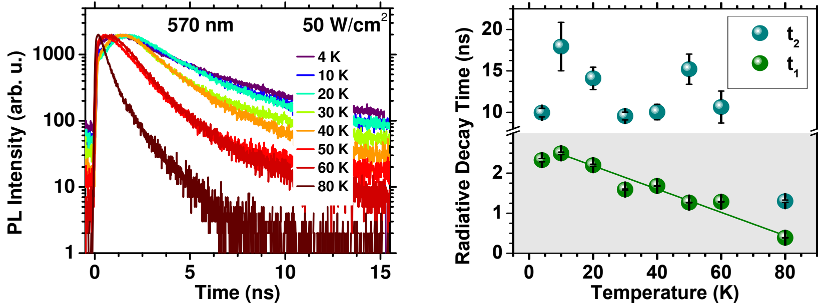

Figure 7.5.: (left) Decay time evolution of the X line in Fig. 7.2 for different temperatures and an EPD of 50 W/cm^2. **(right)** Extracted short (t_1) and long (t_2) decay times of the graphs beside.

An increase of the temperature has a significant impact on the decay times of the X luminescence. A linear decrease of t_1 from 2.45 ns at 10 K down to 0.49 ns at 80 K with a slope of 29 ps/K is observable in this temperature regime. The long decay time t_2 stays nearly constant up to 60 K and decreases rapidly towards 80 K. It has to be noted that the values for t_2 suffer a large error, because of the limited time window between the excitation cycles of just 20 ns, so the error bars in Fig. 7.5 (right) of t_2 just reflect the errors of the fits which are underestimated.

7.3. Excitation Wavelength Dependent Measurements

Excitation wavelength dependent spectra and decay time measurements have been investigated for between 450 and 600 nm. The spectra for the different excitation wavelength are shown in Fig. 7.6 (left). While keeping the EPD constant for every wave-

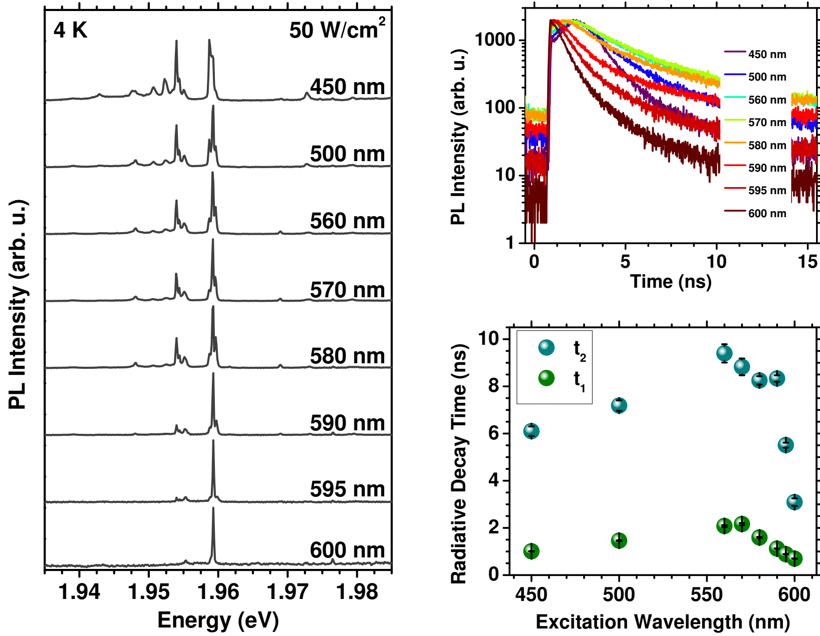

Figure 7.6.: (left) Normalized µ-PL-spectra of a single QD for different excitation wavelength. **(top right)** decay histograms of the X luminescence shown left. **(bottom right)** Short and long decay times extracted from the histograms above.

length, an increase of the excitation efficiency can be observed with decreasing excitation wavelength.

In Figure 7.6 (top right) the decay histograms of the X luminescence for different excitation wavelength are displayed, ranging from 450 to 600 nm. In this graph, the onsets of the different traces are horizontally aligned.

With decreasing wavelength, a significant delay of the maximum intensity can be observed, resulting from the onset of the XX exci-

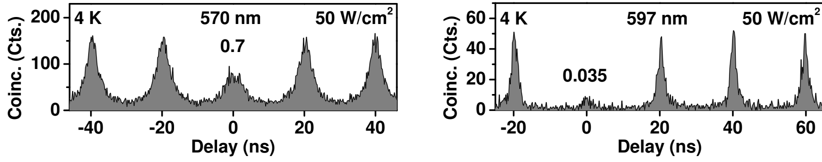

Figure 7.7.: Auto-correlation measurements on the X luminescence line at 4 K and 50 W/cm^2 EPD. **(left)** with an excitation wavelength of 570 nm and **(right)** with 597 nm. Spectra in Fig. 7.6(left).

tation starting around 590 nm. The dramatic change of both, the short and the long decay time, is plotted below. In this graph an increase of both decay times with increasing excitation wavelength is visible between 450 nm and ≈565 nm, hitting a maximum there and are then drastically decreasing towards 600 nm. Especially the rapid decrease of the long decay time t_2 is very interesting with respect to the refilling effect. A wavelength of 595 nm corresponds to ≈2.084 eV, which can be attributed to the energy of the defects or traps causing the refilling.

7.4. Photon Statistics Measurements

Additionally to the investigation of decay times, auto-correlations on the X luminescence line have been performed in order to proof the single quantum system character of the investigated feature. In Figure 7.7 two measurements of this kind on the same luminescence line are shown, the left one with an excitation wavelength of 570 nm at 4 K and the right one with 597 nm, also at 4 K, the corresponding spectra are shown in Fig. 7.6(left).

The left histogram shows a slow decay time, leading to an overlap of the neighboring peaks and a weak suppression of multi-photon events per excitation cycle of only 30%, a dip inside

the central peak, which is expected in case of refilling, was not resolved. The right histogram has clearly separated peaks and reveals a very strong suppression of multi-photon events, resulting in $g^{(2)}(\tau = 0) = 0.035$. This shows clearly the benefit, with respect to refilling suppression, of an excitation energy close to or at the wetting layer energy, however, this kind of excitation is less efficient than above band excitation.

7.5. Conclusion

The introduction of a GaP layer to avoid the formation of APDs seemed to be successful, from the point of QD luminescence no indications for their existence have been observed. The low QD density obtained from the optimized growth recipe allowed the measurement of single QDs. From EPD dependent measurements X and XX luminescence could be observed with an XX binding energy of ≈ 5 meV and a zero-phonon X-FWHM of ≈ 240 µeV.

Temperature dependent luminescence measurements could be performed up to 80 K, while strong refilling was observed up to 60 K and vanished nearly at 80 K. Along that, the fast decay time linearly decreased from 2.4 ns at 4 K down to 0.5 ns at 80 K. The thermal evolution of the X linewidth is related to a effective phonon energy of 41 ± 16 meV.

From excitation wavelength dependent analysis of the decay times, an increase of both, the fast and slow decay time, derived from bi-exponential fits, increased from 1 and 6 ns, respectively, at 450 nm up to 2 ns and 9 ns at 560–570 nm, hitting their maximum, to fall again rapidly towards 600 nm. This indicates an effective pumping of carrier traps around an energy of 2.18–2.21 eV. The refilling effect nearly vanished at an excitation wavelength of ≈ 590 nm (≈ 2.1 eV).

Auto-correlation measurements at excitation wavelengths of 570 nm and 600 nm revealed multi-photon suppression down to $g^{(2)}(\tau = 0)$ values of 0.7 and 0.035, respectively, the big difference is related to the suppression of refilling and a lower background luminescence at lower excitation energy.

8. Comparison of Material Systems and Techniques

Several approaches to integrate III/V semiconductor structures on complementary metal oxide semiconductor (CMOS)-compatible Si(001)-wafers have been investigated in this work. The applied strategies tried to suppress the negative implications of the lattice mismatch between Si and gallium arsenide (GaAs) that introduces threading dislocations and thermal strain in the samples. Further, the formation of anti-phase domains (APDs) was tried to be prevented by special surface preparation techniques before the GaAs buffer growth, which should avoid single-atomic steps on the surface that are the reason for the formation of anti-phase boundaries (APBs) leading to internal electric fields. Additionally, measurements of quantum dot (QD) samples fabricated on GaAs wafers were presented to illustrate advanced methods of QD density reduction and site-controlled nucleation.

8.1. Comparison of Sample Processes

GaAs Substrate

The plain GaAs substrate is an ideal material for the deposition of aluminum gallium indium phosphide (AlGaInP) barrier layers and indium phosphide (InP)-QDs. Standard growth receipts for InP-QDs are leading to a very high density of QDs on 6° miscut

wafers, suitable for light emitting diodes (LEDs) and lasers, but not single-QD spectroscopy. But the miscut allows doping of the structures and prevents an ordering of the barrier material.

Due to that, three approaches have been utilized within this work that enabled us to show single-photon emission from single QDs up to temperatures of 110 K.

Micro Pillar Sample The fabrication of micro-pillars (MPs) by focused ion beam (FIB) allowed access to single QDs, exhibiting triggered single-photon emission up to a temperature of 100 K with $g^{(2)}(0) = 0.34$ [43]. This temperature is still the highest published in literature [44, 103, 134, 137] for InP-QDs up to now. Luminescence of single QDs could be measured up to 130 K on this sample, with a $(Al_{20}Ga_{67})_{51}In_{49}P/(Al_{50}Ga_{67})_{51}In_{49}P$ hetero-confinement barrier. The MPs showed quality factors up to 6000 and allowed detailed radius dependent mode investigations with excellent agreement of experiment and theory [61].

Reduced Density Sample The appliance of a density reducing growth recipe allowed single QD measurements without the need of pre- or post-processing. On this sample we could even present single-photon emission, with refilling effect, up to 110 K with $g^{(2)}_{\text{deconv.}}(\tau = 0) = 0.41$, which is, at the time of writing this thesis, a new temperature record for InP-QDs. Luminescence from single QD could even be observed my micro-photoluminescence (µ-PL) measurements up to 130 K with a simple $(Al_{33}Ga_{67})_{51}In_{49}P$ barrier, in comparison to the micro-pillar sample discussed above.

The possibility to measure single QDs on an un-processed sample is a very important step forward. Unfortunately, this kind of recipe still has to be improved further to suppress the unwanted refilling effect.

Site-Controlled InP Nucleation The sample, pre-processed with a LANGMUIR-BLODGETT-process to create a regular pattern of nano-holes as nucleation sites, has been scanned for photoluminescence (PL). The resulting map showed a good corresponding between the processed pattern and the PL intensity. The found luminescence has its origin in InP-islands nucleated at the nano-holes. Unfortunately, this luminescence showed no anti-bunching behavior. In between these islands, single InP-QDs have been found.

This approach is extremely interesting due to the possibility to fabricate site-controlled QDs e.g. inside of micro-resonators of wave-guides. Further investigations to reduce the size of the nucleated islands have to be performed to achieve single-photon (SP) emission from these structures.

GaAs on Silicon Substrate

Two samples where investigated with the GaAs buffer directly deposited on the Si wafer, implementing indium arsenide (InAs)-QDs and a indium gallium arsenide (InGaAs)-super lattice (SL) to suppress the propagation of threading dislocations:

InAs QD-Strain-Layer The integration of five InAs-QDs layers, which should reduce the density of threading dislocations by bending or annihilation, still showed strong refilling effects of the InP-QD luminescence. It has a brighter ensemble luminescence than the sample with the InAs/GaAs-SL. The maximum temperature for µ-PL measurements of 100 K is slightly above average.

The missing indications for the identification of exciton (X) and biexciton (XX) and the very abrupt drop of luminescence intensity with temperature have to be further analyzed. To enhance the

suppression of defect propagation further, variations of the number and distance of the InAs-QD layers should be investigated in the future.

InGaAs/GaAs Super-Lattice The approach of InAs/GaAs-SL integration revealed the same amount of refilling as found for the InAs-QD strained sample described above. The maximum temperature of 140 K that still allowed single QD µ-PL measurements was the highest presented in this work. Clear signatures of X and XX luminescence have been demonstrated.

The origins of the observed blue-shift and the refilling effect have to be further investigated. The overall weak luminescence and the high amount of uncorrelated PL background with raising temperature did not allow for auto-correlation measurements at elevated temperatures.

GaAs on Germanium Virtual Substrate

The deposition of a germanium virtual substrate (GeVS) layer by molecular beam epitaxy (MBE), resulting in a smooth virtual substrate surface for the GaAs buffer on the Si-wafer, reduced the amount of threading dislocations very efficiently, as a consequence, no refilling effect has been observed.

Interestingly, the density of QDs was very low, which might be related to the low temperature used for the GaAs deposition in order to prevent the segregation of Ge, but leading to a non-optimal crystal quality.

Additionally, the single-QD luminescence was extremely weak, allowing a maximum temperature for µ-PL measurements of only 30 K. Consequently, auto-correlation measurements could only be performed at 4 K. Further, time resolved single-photon counting

measurements showed a mono-exponential decay time of 1.23 ns which is long in comparison to the other structures.

GaAs on GaP/Si

The integrated gallium phosphide (GaP)-layer, deposited on a specially prepared Si buffer exhibiting only atomic double-steps, provides a a very smooth and defect free surface for the GaAs buffer deposition. This structure avoids the formation of APDs, verified by atomic-force microscope (AFM) and scanning electron microscope (SEM) measurements [105].

Still the lattice mismatch is present and leads to the formation of threading dislocations within the subsequently grown GaAs buffer. Therefore a strong refilling effect was detected by time resolved µ-PL measurements.

Temperature dependent measurements revealed a decrease of the refilling effect at a temperature of 60 K and a maximum temperature of 80 K for single-QD µ-PL measurements.

Tuning of the excitation wavelength allowed the suppression of the refilling effect which nearly vanished at an excitation wavelength of 590 nm. Auto-correlation measurements at 4 K revealed $g^{(2)}(\tau = 0) = 0.035$ with an excitation wavelength of 597 nm.

Comparison

Some important properties of the investigated QDs on the different sample structures are assembled in Table 8.1. In this table it is obvious, that the X-full-width at half-maximum (FWHM) has its smallest values for InP-QDs fabricated on GaAs substrates and the sample with the thin and smooth GaP-layer. The samples with the strain layers and the GeVS reveal the largest X-FWHMs, which might be related to crystal defects, due to the incorporated

Sample	QD #	E (eV)	Γ (µeV)	$E_{\text{bind}}^{\text{XX}}$ (meV)	E_{flip} (meV)	t_1 (ns)	$T_{\text{max}}^{g^{(2)}}$ (K)
GaAs – MP	1	1.987	250	6.9	3.9	0.33	100
GaAs – red. density	18	1.894	200	4.1	6.9	0.88	110
	14	1.911	267	2			4
Si/InAs-QD	16	1.815	372	3.6			4
	19	1.781	417				4
Si/InGaAs-SL	1	1.725	686	5.13		0.7	4
	12	1.816	500	5.1			4
	11	1.828	339	6.2			4
	6	1.878	830	6.5			4
Si/GeVS	5	1.846	646	(3)		1.23	4
	6	1.894	460				4
	7	1.993	464				4
Si/GaP	20	1.958	240	6		1.23	4

Table 8.1.: Assembled optical properties of InP-QDs on the investigated sample structures.

strain and the low growth temperature for the buffer on the GeVS sample.

The XX binding energies are mostly between 5 and 7 meV, except for the reduced density sample, interestingly, on the GaP/Si-sample they are in the normal range, despite the usage of the reduced density recipe. The value in brackets for the GeVS indicates, that there the luminescence lines were not clearly identified.

The decay times shown in the table just reflect the short components of the decay, not any refilling effects. Here, the MP-sample has a very short decay time, maybe due to a small Purcell-enhancement. All other decay times are comparably slower than the typical decay times for InP-QDs, which are around 500 ps [62].

8.2. Refilling

Nearly all samples showed a strong refilling effect, which seems to arise from charge carrier traps. This traps are spatially located in the barrier, which could be shown by excitation wavelength dependent measurements. Their potential depth has been estimated to be ≈ 5–$9\,\mathrm{meV}$ on the basis of temperature dependent measurements.

The origin of these traps may also be found in a temporary problem of the used metal-organic vapor-phase epitaxy (MOVPE)-system, which, unfortunately, had a gas leakage in the reactor within the time the studied samples were fabricated. This assumption can be affirmed by the fact that MOVPE runs with identical receipts, where leading to refilling effects within the mentioned time frame, but not before.

8.3. Outlook

Excitation wavelength dependent measurements should be performed in detail to investigate the origin of the prominent refilling effect further. Due to the wavelength dependent electron–hole pair (e–h pair) generation efficiency, one could try to keep the µ-PL-spectra identical, while varying the wavelength in contrast to keep the excitation power density (EPD) constant.

The techniques, presented in this work, to implement strain into the buffer structure have to be studied more in detail, regarding the number and position of the strain incorporating layers and their composition.

The recipes for density reduced InP-QD samples have to be investigated regarding the prominent refilling effect. Additionally, the site-controlled process, performed on exactly oriented

substrates, should be investigated on miscut wafers to omit an ordering effect of the barrier material and to therefore enhance the carrier confinement.

A higher Al content in the barrier material is promising to enhance the maximum temperature for SP emission towards the Peltier cooling regime.

9. Modeling of Single-Photon Purity and Efficiency

Utilizing QDs for the generation of single-photons on demand at elevated temperatures gives raise to investigate the influence of the XX luminescence in the energetic region of the X luminescence line with respect to the purity of SP generation. A critical glance on the Poissonian-distribution (see Fig. 2.4) that describes the e–h pair generation at a given pump power, reveals an obvious problem. If one wants to have a high probability to generate just a single X-photon, the mean number of generated e–h pairs has to be $\ll 1$ and therefore the probability of not exciting the system is much higher than that of exciting exactly one or more e–h pairs. Therefore, the generation of more than one e–h pair is favorable, but results in a significant probability of XX recombination. At elevated temperatures the broadening of the luminescence lines can result in an energetic overlap of X and XX, increasing the probability of multi-photon events within the energetic region of the X luminescence. The scheme for the model is illustrated in Figure 2.3.

In this chapter, a model, realized in GNU Octave, will be presented which adopts fits to measured data points that are significant for the temperature dependence of the XX–X overlap and extrapolates them towards higher temperatures. From this extrapolation, luminescence spectra can be generated and analyzed for SP–purity and their generation efficiency within certain energetic regions of interest.

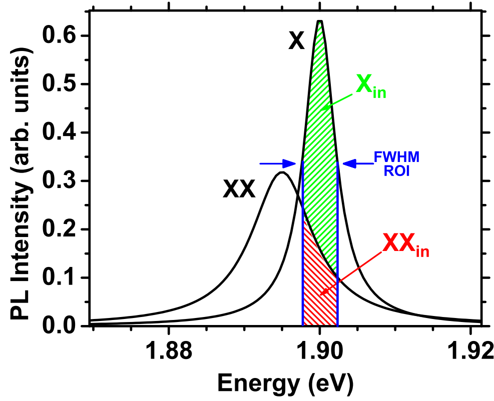

Figure 9.1.: Scheme for the XX–X overlap simulation.

Some parts of the program can be found in the Appendix A.2.1.

9.1. Modeling the carrier generation

The probability for the generation of a certain number of e–h pairs follows the POISSONIAN-distribution (2.5). The mean number λ of generated e–h pairs is a parameter that is proportional to the excitation power density. By varying this parameter the influence of the excitation power density on the spectrum can be investigated. The model limits the maximal e–h pair number to 8, the maximal number of e–h pairs that can be confined in the s- and p-shell. The development of the other parameters and their starting values at 4 K are derived from measurements of the corresponding quantum dot types.

9.2. Obtaining of System Parameters

For the modeling of the overlap behavior in the InP/AlGaInP material system the data presented in Section 4.1 was analyzed to obtain the needed parameters for the model.

9.2.1. Spectral Position

The spectral position of the X and XX, especially their energetic distance, was derived from the spectra shown in Figure 4.4(a). The XX binding energy of 6.9 meV was extended with the additional values of 5 and 10 meV for the calculations, in order to estimate the XX influence in the range of actually found XX binding energies for InP-QDs [43, 62, 71].

9.2.2. Linewidth

The thermal evolution of the linewidth of X and XX has been fitted to the data shown in Fig. 4.6(a) with the formula (2.36) described in Sec. 2.8.5. The resulting parameters were used to extrapolate the FWHM of the lines up to 200 K.

9.2.3. Temperature Induced Red-shift

To be able to generate correct temperature dependent luminescence spectra, the red-shift of the luminescence lines was included in the model by using Equation (2.35) up to 200 K with parameters derived from the data shown in Fig. 4.5(b).

9.2.4. Dark State Dynamics

The relative intensities of the X and XX luminescence strongly depends on the dark exciton state (DS)–bright exciton state (BS)

splitting energy, set to 5 meV for the model. Therefore, the populations of these states have been calculated with a temperature dependent rate equation model [143]. At the beginning of an excitation cycle, the X spin configuration has an equal probability to be in the DS or BS due to random spin flips during the relaxation process. Then temperature dependent spontaneous and stimulated spin flips into and out of the DS are happening, resulting in a temperature dependent lifetime of the X and also in a temperature dependent dynamic of the XX population probability due to the probability of a trapped e–h pair in the DS [62].

9.2.5. Thermal Quenching

The intensities of the X and XX luminescence shown in Fig. 4.5(a) have been analyzed with Arrhenius like fits to obtain activation energies that are leading to a loss of charge carriers out of the system and therefore to a quenching of the luminescence. The parameters of 96 meV for the X and 80 meV for the XX as activation energies have been derived from the data.

9.2.6. Spectral Region of Interest

An important parameter, which is freely selectable, is the spectral region of interest (ROI) from which the emitted photons of the single-photon source (SPS) are detected. Additionally to the scheme in Fig. 9.1, two more ROIs have been used within the model, which are shown in Fig. 9.2. The left one has a spectral width of half the FWHM of the X, while the right one has the double width of the X FWHM but shifted to the right. All the described ROIs are of course temperature dependent, they move spectrally with the peaks and change their widths according to the X linewidth.

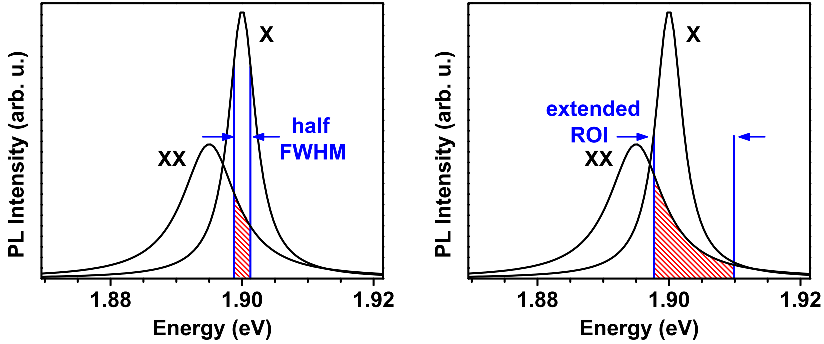

Figure 9.2.: Different ROI-schemes used in the model: (left) half XFWHM; (right) double X-FWHM extended to the high energy side.

9.3. Flowchart of the model

The calculation scheme of the model is displayed in Fig. 9.3. At the top of the flow chart, a pulse is generated. This results in probabilities for zero, one, and two e–h pairs, while higher numbers of generated e–h pairs than two are assumed to relax consecutively into the two–e–h pair state and their probabilities are therefore summed up. The one–e–h pair state represents the probability of just one e–h pair in the system. This results in a normalized probability of 1 for the mentioned three states per excitation cycle.

The calculated probabilities for the states are now 'thermally quenched' according to the derived activation energies (Sec. 9.2.5) for the X and XX. This 'quenched probabilities' are added to the *zero probability* like the zero–e–h pair probability itself, what preserves the normalization. For the un-quenched XX probability resulting from the two–e–h pair state, the probabilities for the emission into and out of the ROI are calculated (XX_{in} and $XX_{\mathbf{out}}$).

At this point, there are three probabilities for the existence of

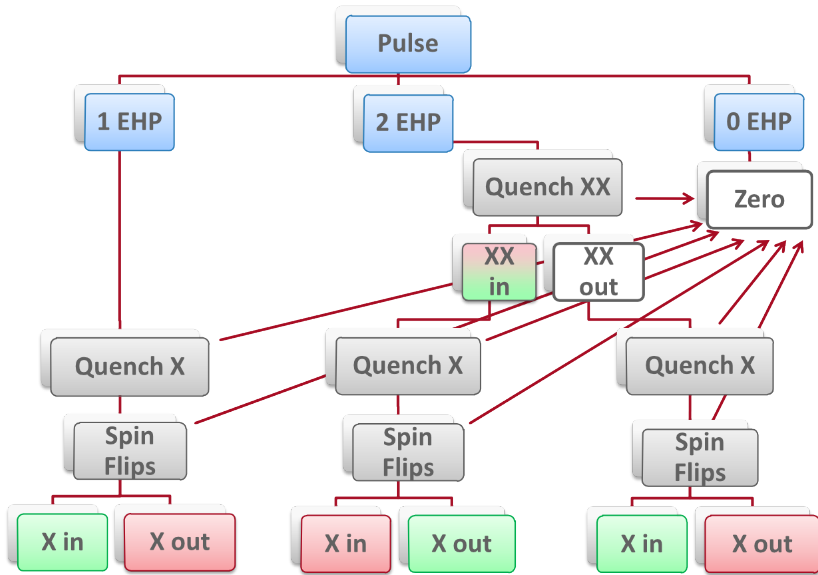

Figure 9.3.: PeakSim-FlowChart

an X state. These populations now undergo spin-flips, described in Sec. 9.2.4. The resulting probabilities for a populated DS are regarded as non-emitting and are therefore added to the *zero probability*. Finally the remaining probabilities for an X emission are distributed in photons emitted into and out of the ROI. While the left and right probabilities for X_{in} result in single X photons, the middle branch may result in two photons within the ROI per cycle or a single XX in the ROI: Therefore the XX_{in} field is shaded in red/green, because it may be a final state if the following X is quenched, flipped into the DS or emitted outside the ROI, what results in a single-photon event (green). If the following X is emitted within the ROI, the result is a two-photon event and is

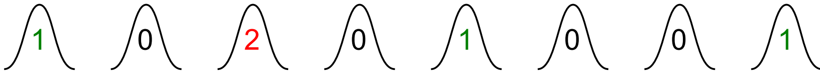

Figure 9.4.: Sequence of eight subsequent excitation cycles with the number of photons emitted within the ROI for each pulse.

therefore shaded in red.

All events resulting in a single-photon per pulse are shaded in green, while events resulting in none or two photons within the ROI are shaded in red.

9.4. Modeled Quantities

9.4.1. Photon Emission Probability Into the ROI

One value of interest is the probability of a photon to be emitted in a spectral ROI. The ROI can be chosen freely, one obvious region is, e.g., the FWHM of the X. With the model it is possible to calculate the probability of *at least one* photon to be emitted within this energetic region per excitation cycle. This value will be called *efficiency* ε in the following.

Fig. 9.4 shows an example for a photon distribution within eight subsequent excitation cycles. For this example the *efficiency* would be calculated as follows:

$$\varepsilon = \frac{4}{8} = \frac{1}{2} = 0.5 \tag{9.1}$$

9.4.2. Purity of Single-Photon Emission

A main goal of a SPS is to emit single-photons with a high purity. This value will be called φ and reflects the *ratio of single-photons*

per detection event. For the sequence given in Fig. 9.4 one would calculate:

$$\varphi = \frac{3}{4} = 0.75 \tag{9.2}$$

9.4.3. Single-Photon Efficiency

The SP-efficiency ξ, which is defined as the *probability of single-photons per excitation cycle in the ROI*, can now be defined as the product of *efficiency* ε and *purity* φ

$$\xi = \varepsilon \cdot \varphi \ .$$

For the values derived from the sequence displayed in Fig. 9.4 one would calculate:

$$\xi = \varepsilon \cdot \varphi = \frac{1}{2} \cdot \frac{3}{4} = \frac{3}{8} = 0.375 \ . \tag{9.3}$$

9.5. Results

9.5.1. Calculations Without Thermal Quenching

The input parameters λ, which is proportional to the EPD, and the sample temperature T of the model have been varied between 0.1–4 and 5–200 K, respectively. For the following results, the thermal quenching is disabled in the model, to analyze a thermally stable system.

Out of the calculated probabilities for photons from different branches of the flow chart (Fig. 9.3) to be emitted into and out of the X FWHM-ROI, the quantities efficiency ε and purity φ have been obtained and plotted in 2-dimensional plots, shown in Figure 9.5.

In the left plot, the *efficiency* ε is displayed color-coded versus λ and T. ε raises with temperature due to the thermalization of

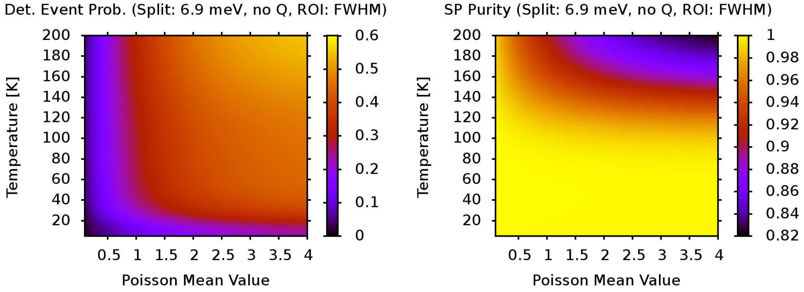

Figure 9.5.: (left) EPD and temperature dependent efficiency ε within the X-FWHM ROI. (right) EPD and temperature dependent purity φ, both for a BS–DS splitting energy of 6.9 meV without thermal quenching.

BS and DS leading to a maximum value of $\varepsilon \approx 0.5$ at maximal temperature and EPD.

However, in the right plot, the *SP-purity* ϕ shows the opposite behavior. At temperatures $T < 80\,\mathrm{K}$, the XX-X overlap is negligible, at higher temperatures its influence on the *SP-purity* raises. This XX influence is additionally depending on the EPD, which nicely can be seen at high temperatures, where the stronger XX luminescence, with raising EPD, gradually lowers the *SP-purity* to a minimum value of $\varphi = 0.82$.

By multiplying the plotted probabilities on the left and right side of Graph 9.5, the *single-photon efficiency* $\xi = \varepsilon \cdot \varphi$ can be obtained, which is shown in Fig. 9.6.

In this plot, ξ shows a high SP-efficiency $0.3 \leq \xi < 0.5$ for a broad range of temperatures $T > 60\,\mathrm{K}$, due to the BS–DS thermalization, and for $\lambda > 1.5$, allowing a sufficient e–h pair generation.

The limitation of $\xi < 0.5$ can be expanded by selecting a different ROI to collect more photons. In Graph 9.7 (right) three

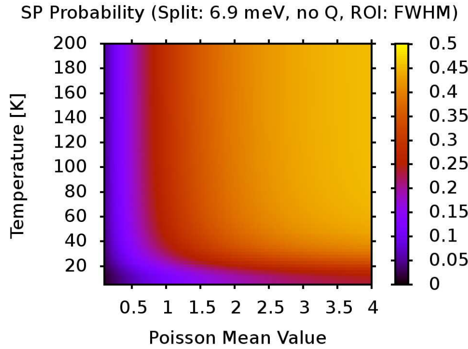

Figure 9.6.: EPD and temperature dependent SP-efficiency ξ within the X-FWHM ROI for a BS–DS splitting energy of 6.9 meV without thermal quenching.

different modeled ROIs are displayed. The upper one is doubled in its spectral width and expanded to the high energetic side to suppress the collection of XX photons. The left hand side shows the temperature dependence of SP-purity and efficiency, color coded for the different ROIs; black arrows indicate the evolution of the EPD. The red curves, corresponding to the expanded ROI, display an enhanced efficiency up to 70%, at the cost of a reduced purity. A better purity can be realized by reducing the ROI, this is shown in the lower scheme on the right, with blue curves representing a high purity $\varphi > 0.9$, and a reduced efficiency $\varepsilon < 0.3$. The scheme in the middle with corresponding green curves shows the already discussed X-FWHM ROI for comparison.

9.5.2. Calculations With Thermal Quenching

In order to investigate the XX influence for systems that show reasonable thermal quenching up to 200 K (like the reference data

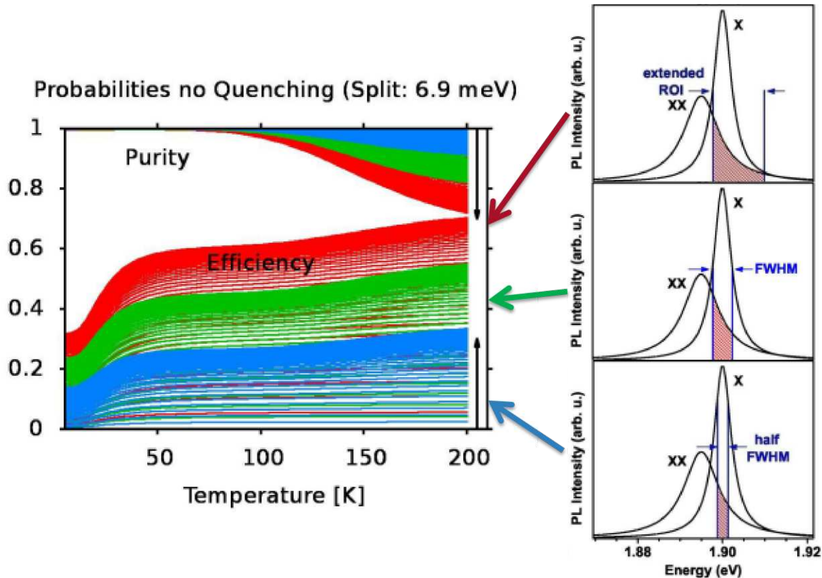

Figure 9.7.: Temperature dependency of SP-purity φ and efficiency ε for different ROIs (color coded) with raising EPD along black arrows.

in Fig. 4.4), calculations including the thermal quenching effect have been performed. The according results are plotted in Fig. 9.8.

In the left graph of Fig. 9.8 the efficiency ε is plotted, the maximum efficiency of $\approx 43\%$ is reached for a temperature of $T \approx 50\,\mathrm{K}$ and a high EPD, this temperature dependency results from the influence of the DS at low temperatures, which reduces the X luminescence. Contrary, the purity (shown in Fig. 9.8 (right)) is worst at the point of high temperature and high EPD, but mainly temperature dependent. It is visible, that for very low EPDs the purity is nearly perfect and stays very high due to the stronger quenching of the XX emission intensity and the low

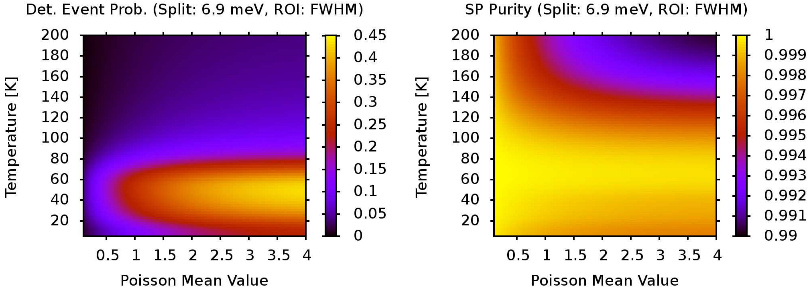

Figure 9.8.: **(left)** EPD and temperature dependent efficiency ε within the X-FWHM ROI. **(right)** EPD and temperature dependent purity φ, both for a BS–DS splitting energy of 6.9 meV.

efficiency of only $\approx 5\%$ at temperatures $T < 80\,\mathrm{K}$ shrinking down the probability of two photons emitted within the ROI in a single excitation cycle, comparable to the SP-generation with faint laser pulses [144].

By multiplying the plotted probabilities on the left and right side of Graph 9.8, the *single-photon efficiency* ξ can be obtained, which is shown in Fig. 9.9.

The high SP-purity, even at high temperatures, results from the strong quenching of the whole QD luminescence and especially from the stronger quenching of the XX, reducing its influence on the SP-purity. Consequently, ξ is nearly identical with ε.

Depending on the geometry and material system, QDs show different XX binding energies. To illustrate the influence of this parameter, tree different XX binding energies, 5, 6.9, and 10 meV, have been modeled. Figure 9.10 shows the SP-purity for these binding energies at different EPDs of $\lambda = [0.1, 1, 4]$. It is visible, that smaller XX binding energies enhance the negative impact on the SP-purity, furthermore, the onset of the overlap influence

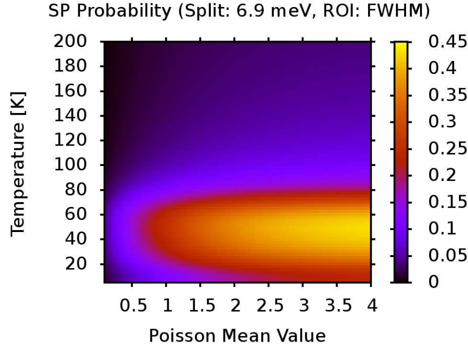

Figure 9.9.: EPD and temperature dependent SP-efficiency ξ within the X-FWHM ROI for a BS–DS splitting energy of 6.9 meV.

happens at lower temperatures and with an higher slope. At $\lambda = 4$ the difference between 5 and 10 meV XX binding energy on the SP-purity is $\Delta\varphi \approx 0.07$.

9.6. Conclusion & Outlook for the Model

The results obtained from the model are encouraging to use QDs as SPS. The influence of the XX spectral overlap still allows a high degree of SP-purity. By carefully selecting an spectral ROI one can find the right balance between purity and efficiency of the SPS.

In the best modeled case, a SP-efficiency of $\approx$60% with a SP-purity of $\approx$70% at $\lambda \approx 1.25$ with an XX binding energy of 10 meV and an extended ROI could be obtained at a temperature of 200 K, in case of no thermal quenching up to this temperature. This would allow the operation of a QD based SPS in the regime of Peltier-cooling.

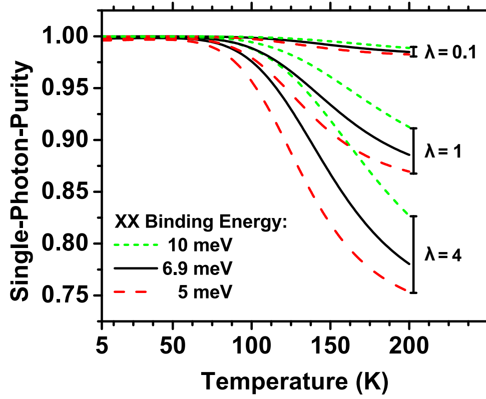

Figure 9.10.: Temperature dependence of the SP-purity for different XX binding energies of 5, 6.9, and 10 meV and different excitation parameters $\lambda = [0.1, 1, 4]$.

For further analysis of the overlap effect, the model could be enhanced to implement higher excited states, resulting in multi-photon events, and refilling effects from carriers in a reservoir. Also, a way to access the value of $g^{(2)}(\tau = 0)$ would be of high interest.

10. Summary & Outlook

The investigations on the luminescence of indium phosphide (InP)-quantum dots (QDs) on gallium arsenide (GaAs) substrates and on Si based structures revealed promising results regarding their operation as single-photon source (SPS). For InP-QDs on GaAs substrates new records for their operation as SPS at elevated temperatures have been achieved. For QDs embedded in micro-pillars (MPs), a suppression of multi-photon events down to $g^{(2)}(\tau = 0) = 0.34$ at 100 K with short decay times of 0.33 ns has been reached. The barrier material has a confinement energy of ≈ 90 meV, this has been confirmed by measurement of the activation energies for the charge carriers out of the QDs.

In this work, additionally several methods to address single QDs on GaAs substrates by reducing their density or controlling their nucleation sites have been investigated. For the density reduced sample, it was even possible to enhance the working temperature up to 110 K with $g^{(2)}_{\text{deconv.}}(\tau = 0) = 0.41$. This GaAs based sample structure, however, showed charge carrier refilling effects, which may be related to crystal defects in the barrier region, acting as potential traps for charge carriers. Further investigations on this effect are needed to optimize the quality of the QD barrier to allow triggered single-photon (SP) emission.

The possibility to reduce the density of the QDs itself is very promising, with this technique it may be possible to embed single InP-QDs within resonators or wave-guides.

The site-controlled nucleation of QDs was leading to the for-

mation of InP-islands. Their luminescence correlates well with the processed nucleation-site-pattern, which has been proven by two-dimensional micro-photoluminescence (µ-PL) scans. For their usage as SPS, the growth parameters have to be optimized to reduce their size down to a length scale of regular InP-QDs in order to achieve discrete energy levels for the charge carriers.

An important part of this work was the investigation of the luminescence of InP-QDs fabricated on complementary metal oxide semiconductor (CMOS)-compatible Si-substrates. The lattice mismatch between Si(001) substrates and the GaAs matrix demands special layer structures in order to prevent threading dislocations and anti-phase domains (APDs).

In this work, four different hetero-epitaxial approaches (realized by our epitaxy group) have been investigated to suppress the formation of APDs and threading dislocations. The threading dislocations in the GaAs buffer layer, deposited below the QD barrier layer, have been bend away from the growth direction by the implementation of strained layers. Therefore two techniques have been utilized to accomplish this. On the one hand side, five indium arsenide (InAs)-QD layers have been deposited within the GaAs buffer, on the other hand, an indium gallium arsenide (InGaAs)/GaAs-super lattice (SL) was utilized to implement strain into the structure. Both approaches still showed strong refilling effects of the QD luminescence, indicating a significant amount of remaining defects. The temperature stability of both samples allowed µ-PL-measurements on single QDs up to 100 K and 140 K, respectively. SP emission has been shown by both samples at low temperatures, while the weak luminescence intensity and a high amount of uncorrelated background prohibited autocorrelation (ACO)-measurements at elevated temperatures.

Additionally, a sample was prepared with a germanium virtual substrate (GeVS) on the Si-wafer (IHT, Uni Stuttgart). This

resulted in a very smooth virtual substrate surface and reduced the defect density efficiently. As a consequence, no refilling effects have been found, and the QD density was low due to a low number of nucleation sites. This allowed for single-QD spectroscopy, which unfortunately revealed only very weak QD luminescence up to a temperature of only 30 K. Still, time-resolved µ-PL-measurements have been performed at 4 K. Resulting in triggered SP emission with comparably long decay times of ≈ 1.2 ns (typically 500 ps). The weak luminescence of the sample may be related to a reduced crystal quality, arising from a lower growth temperature used for the buffer layer to prevent Ge segregation.

The formation of APDs, resulting from mono-atomic surface steps that are leading to stacking faults, has been efficiently suppressed by the implementation of a thin gallium phosphide (GaP) layer on top of a specially prepared Si wafer, revealing only atomic double-steps for the subsequent GaAs buffer matrix (realized by STRL, Philipps Uni Marburg). With this method, the lattice mismatch still remains and consequently time-correlated single-photon counting (TCSPC) measurements showed strong carrier refilling effects. A tuning of the excitation wavelength close to the barrier band gap energy, allowed a suppression of the refilling effect and allowed triggered SP generation at 4 K. While single-QD luminescence has been observed up to 80 K.

The various temperature and excitation power density (EPD) dependent exciton (X) and biexciton (XX) parameters obtained by the µ-PL-measurements, like activation energies of ≈ 90 meV, spectral linewidth dependence, dark exciton state (DS)–bright exciton state (BS) splitting of ≈ 5 meV and XX binding energies of ≈ 7 ± 3 meV have been used to model the X–XX system. With this model, one can extrapolate the temperature dependence of the spectral overlap between XX and X luminescence towards higher temperatures. Further, the temperature and EPD dependent

efficiency and purity of the generated SPs has been calculated with the model. The obtained results are promising for an InP-QD based SPS in the temperature regime of PELTIER-cooling.

To further enhance the temperature limits for InP-QDs as SPSs, the charge carrier confinement has to be raised. The quality of SP generation can be improved by an optimization of the growth parameters for the buffer- and barrier-layers. This will suppress refilling effects and non-radiative decay channels and therefore allows brighter and triggered single-photon emission. Investigations on phonon-QD coupling may then help to further extend the operation temperature of the SP generation, while an understanding of the manipulation of the E_{flip} energy can help to use of the X DS for further optimization.

Zusammenfassung und Ausblick

Die Untersuchungen zur InP-Quantenpunkt Lumineszenz auf GaAs Substraten und Silizium basierten Strukturen haben vielversprechende Ergebnisse für deren Einsatz als Einzelphotonenquellen ergeben. Für InP-QDs auf GaAs Substraten konnten neue Temperaturrekorde bei ihrem Einsatz als Einzelphotonenquellen erzielt werden. So konnte bei in Mikroresonatoren eigebetteten Quantenpunkten eine Unterdrückung von Mehrphotonenereignissen bis hinab zu einen Wert von $g^{(2)}(\tau = 0) = 0.34$ bei 100 K mit kurzen Zerfallszeiten von 0.33 ns erreicht werden. Die Barrierenstrukturen bieten eine Einschlussenergie von ≈ 90 meV, was durch die Bestimmung von Aktivierungsenergien für die Ladungsträger aus den Quantenpunkten heraus bestätigt werden konnte.

In dieser Arbeit wurden zudem mehrere Methoden zur Adressierung einzelner Quantenpunkte untersucht. Zum einen durch die Reduktion ihrer Dichte, zum anderen durch kontrollierte Positionierung ihrer Wachstumspunkte. Bei den dichtereduzierten Proben war es möglich, die Arbeitstemperatur auf 110 K bei $g^{(2)}_{\mathrm{deconv.}}(\tau = 0) = 0.41$ zu steigern. Diese GaAs basierte Struktur zeigte jedoch Ladungsträger-Nachfülleffekte, die wahrscheinlich von Kristallfehlern in der Barriere herrühren, welche als Potentialfallen für die Ladungsträger fungieren könnten. Weitere Untersuchungen zur Unterdrückung des Nachfülleffekts sind notwendig, um die Qualität der Quantenpunktbarriere zu verbessern und dadurch getriggerte Einzelphotonenemission zu erreichen.

Die Möglichkeit, die Dichte der Quantenpunkte selbst zu er-

niedrigen ist sehr vielversprechend, da so eine Möglichkeit zur Einbettung einzelner InP Quantenpunkte in Resonatoren und Wellenleiter eröffnet werden kann.

Das positionierte Wachstum von InP Quantenpunkten führte zur Bildung von InP-Inseln. Die Lumineszenz dieser Inseln konnte mit zweidimensionalen Mikro-Photolumineszenz Scans gut mit dem prozessierten Muster korreliert werden. Für die Nutzung dieser Inseln als Einzelphotonenquellen müssen jedoch die Wachstumsparameter weiter optimiert werden, um ihre Größe in den Bereich gewöhnlicher InP Quantenpunkte zu erniedrigen und somit diskrete Energieniveaus für die Ladungsträger zu erhalten.

Ein wichtiger Teil der Arbeit, ist die Untersuchung von InP Quantenpunkten, die auf CMOS kompatiblen Silizium Substraten hergestellt wurden. Die Gitterfehlanpassung zwischen Silizium(001) Substraten und der GaAs Matrix erfordert spezielle Schichtstrukturen, um Durchstoßversetzungen und Antiphasendomänen zu verhindern.

In dieser Arbeit wurden vier von unserer Epitaxiegruppe hergestellte heteroepitaktische Ansätze untersucht, um die Bildung von Antiphasendomänen und Durchstoßversetzungen zu unterdrücken. Es wurde versucht, die Durchstoßversetzungen in der GaAs Pufferschicht, unterhalb der Einschlussbarriere, durch die Einbringung von verspannten Schichten zum seitlichen Abknicken zu bringen. Dazu wurden zwei Techniken angewandt, zum einen wurden fünf InAs Quantenpunktschichten, zum anderen ein InGaAs/GaAs Übergitter als verspannendes System in die Pufferschicht eingearbeitet. Bei beiden Ansätzen wurden jedoch weiterhin starke Nachfülleffekte bei der Quantenpunktlumineszenz vorgefunden, was für eine hohe Restdichte an Defekten spricht. Die Temperaturstabilität beider Proben erlaubte Mikro-Photolumineszenzmessungen an einzelnen Quantenpunkten bis hinauf zu 100 bzw. 140 K. Einzelphotonenemission konnte bei niedrigen

Temperaturen auf beiden Proben gezeigt werden. Bei höheren Temperaturen machte die schwache Lumineszenz und der hohe Anteil an unkorrelierter Hintergrundlumineszenz Auotokorrelationsmessungen unmöglich.

Zusätzlich wurden Silizium Wafer mit einem virtuellem Germanium Substrat versehen (IHT, Uni Stuttgart). Dies führte zum einen zu einer sehr glatten Oberfläche, was die Defektdichte erheblich reduzierte und nachfülleffektfreie Lumineszenz ermöglichte. Zum anderen resultierte daraus eine niedrige Quantenpunktdichte, was Mikro-Photolumineszenzmessungen an einzelnen Quantenpunkten erlaubte. Diese zeigten jedoch nur sehr schwache Lumineszenz, die maximal bis zu einer Temperatur von 30 K nachgewiesen werden konnte. Dennoch war es möglich, zeitaufgelöste Messungen bei 4 K durchzuführen. Diese ergaben vergleichsweise lange Zerfallszeiten von ≈ 1.2 ns (typisch 500 ps). Die schwache Lumineszenz dieser Probe könnte auf eine schlechtere Kristallstruktur zurückzuführen sein, da die Pufferschicht bei niedrigeren Wachstumstemperaturen abgeschieden wurde, um eine Aufschwimmen des Germaniums zu vermeiden.

Die Bildung von Antiphasendomänen, die von einatomigen Oberflächenstufen herrühren, die zu Stapelfehlern der GaAs Matrix führen, wurden effizient unterdrückt. Dazu wurde eine dünne Gallium-Phosphid Schicht auf einen speziell behandelten Silizium Wafer aufgebracht, der nur doppelatomare Stufen aufwies (hergestellt von STRL, Philipps Uni Marburg). Bei dieser Methode bleibt jedoch das Problem der Gitterfehlanpassung bestehen was zu TCSPC Messungen führte die starke Nachfülleffekte zeigten. Ein Verschieben der Anregungswellenlänge, nahe zur Barrierenbandlückenenergie, erlaubte bei dieser Probe eine Unterdrückung des Nachfülleffekts und ermöglichte die Messung von getriggerter Einzelphotonenemission bei 4 K. Diese Beobachtung deutet an, dass die Ladungsträgerfallen im Barrierematerial lokalisiert sind.

Einzelpunktlumineszenz konnte bis 80 K erzielt werden.

Die verschiedenen temperatur- und anregungsleistungsabhängigen Exziton und Biexziton Parameter, wie Aktivierungsenergien von ≈ 90 meV, spektrale Linienbreitenabhängigkeit, exzitonische Hell-Dunkel-Zustands-Aufspaltung von ≈ 5 meV und Biexziton Bindungsenergien von $\approx 7 \pm 3$ meV wurden genutzt, um ein Exziton-Biexziton System zu modellieren. Mit diesem Modell kann die Temperaturabhängigkeit des spektralen Biexziton-Exziton-Überlapps zu höheren Temperaturen extrapoliert werden. Weiterhin kann die Reinheit und Effizienz der Einzelphotonenemission berechnet werden. Die daraus gewonnenen Ergebnisse sind vielversprechend für die mögliche Verwendung von InP Quantenpunkten als Einzelphotonenquellen im Temperaturbereich der PELTIER-Kühlung.

Um die maximale Arbeitstemperatur zu erweitern, ist eine Erhöhung der Ladungsträger Einschlussenergie notwendig. Die Qualität der Einzelphotonen kann durch Optimierung der Wachstumsparameter von Puffer- und Barrierenschicht weiter verbessert werden. Dies erlaubt eine Unterdrückung von Nachfülleffekten und nichtstrahlenden Übergängen, und somit hellere und deterministische Einzelphotonenemission. Untersuchungen zur Phonon-Quantenpunkt Kopplung können dann zu einer neuerlichen Erweiterung der Arbeitstemperatur der Einzelphotonenerzeugung führen. Ein tiefergehender Einblick in die Hell-Dunkel-Aufspaltung des Exzitons und deren gezielte Manipulation kann ebenfalls zu weiteren Verbesserungen für die Einzelphotonenezeugung führen.

A. Created Software

A.1. LabVIEW

With the graphical programming language LabVIEW™, several programs were developed to allow the measurements presented in this work. LabVIEW™ supports a large number of laboratory equipment and is therefore highly suited for the controlling of the measurement setup and for data collection and presentation. Two important programs for this thesis are briefly described below.

A.1.1. DotHunter

The DotHunter (DH) program was developed[1] to control the position and focus for µ-PL measurements. Its implementation utilizes the graphical programming language LabVIEW™. Due to the fact that most of the investigated samples contain self-assembled QDs which are randomly positioned, a scanning routine is implemented. This allows the generation of two-dimensional maps, by collecting of site dependent data from various sources, like avalanche single-photon detectors (ASPDs) or ccd-camera spectra (see. Sec. A.1.2) and helps to find interesting features on the sample, even in-situ.

Positions on the sample can be stored and commented in order to easily find them again, even in the case where the sample

[1] Special thanks to Matthias Heldmaier for partially rewriting and enhancing of the programm.

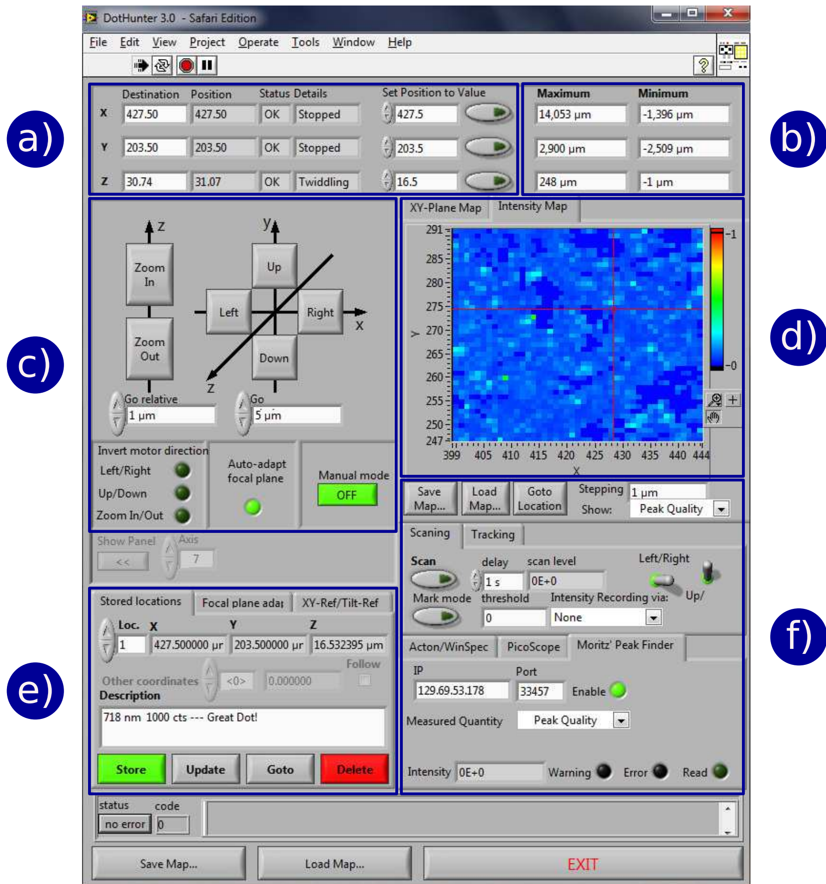

Figure A.1.: Screenshot of the *DotHunter* programm frontend.

is unmounted from the cryostat and remounted in a different orientation. To allow for that, the coordinate system can be rotated to fit the new sample orientation.

Samples are mostly not mounted exactly horizontally, therefore the focus is lost when the sample is moved beneath the objective, this can be compensated by the *focal plane adaption* feature. Here one defines a plane parallel to the sample surface by focusing on three spots on the sample. Afterwards, the focus is corrected for the sample tilt automatically, what allows the generation of maps over large areas and comfortable navigation on the sample.

Figure A.1 shows the frontend of the main program. The part labeled with **a)** allows the setting of a three dimensional coordinate. The region of interest (ROI) that is displayed in the map **d)** can be set in the frame **b)**, while the frame **c)** allows free movement and the setting of the step width. Additionally, the axis can be inverted and the *focal plane adaption* can be controlled. The *manual mode* allows manual operation by switching off the *hold current* of the motors. In part **e)** one can set the coordinates for the *focal plane adaption* and the *reference point* for the sample map. Additionally, locations can be stored and labeled in this frame. In the part named **f)**, various modules for data collection can be controlled in order to perform scans within the ROI.

A.1.2. PeakFinder

The *PeakFinder* is a program which acts as a source for the DH and is also written in LabVIEW™. It can be triggered to read out a ccd-spectrum and analyses it.

The analysis of the spectrum reveals its full integrated intensity (Fig. A.2 a)), the maximal peak height and its wavelength (Fig. A.2 b)), and it additionally calculates a value called *peak quality*. This value is obtained by shifting a *binning range* (marked

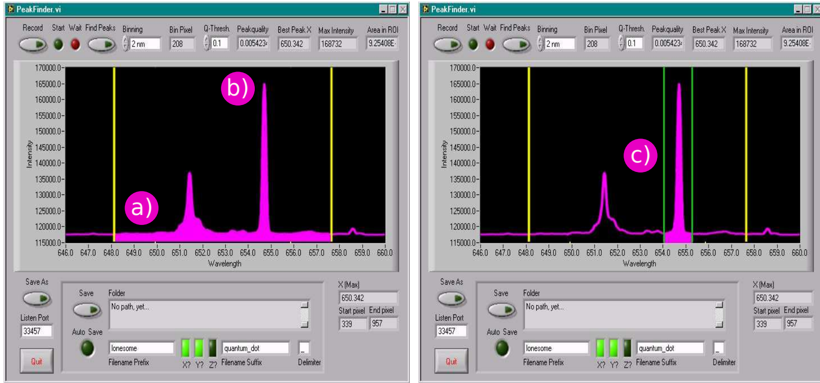

Figure A.2.: Screenshot of the *PeakFinder* programm frontend.

green in Fig. A.2 c)) with a configurable width along the spectrum, determining the wavelength of the first maximum (exceeding the *minimal peak height*) within it, then setting this wavelength as the new center of the *binning range* and checks if the maximum is still valid. In the case of a valid maximum in the center of the *binning range*, the maximum intensity is divided by the integrated intensity within the *binning range*. This ratio is called the *peak quality*. This procedure is then repeated for the whole spectrum. By setting the *binning range*, one can define a desired separation of a peak towards its spectral neighbors. In addition a larger *binning range* is also more background sensitive.

A.2. Octave

GNU Octave is a high-level language, primarily intended for numerical computations. It provides a convenient command line interface for solving linear and nonlinear problems numerically,

and for performing other numerical experiments using a language that is mostly compatible with Matlab. It may also be used as a batch-oriented language.

Octave has extensive tools for solving common numerical linear algebra problems, finding the roots of nonlinear equations, integrating ordinary functions, manipulating polynomials, and integrating ordinary differential and differential-algebraic equations. It is easily extensible and customizable via user-defined functions written in Octave's own syntax or using dynamically loaded modules written in C++, C, Fortran or other languages.

GNU Octave is also freely redistributable software. You may redistribute it and/or modify it under the terms of the GNU General Public License (GPL) as published by the Free Software Foundation.[2]

A.2.1. PeakSim

The following pages are parts of the code written for the XX–X overlap model and should give the reader an impression of the syntax and structure of the language. The full code is too large to be printed within this thesis.

[2]Copyright © 1998-2012 John W. Eaton. Verbatim copying and distribution is permitted in any medium, provided this notice is preserved.

Main Program File

```
#!/usr/bin/octave -qf

echo off

######################################################################
## Peak simulation based on a Poissonian excitation distribution
## (c) Moritz Bommer 2009-2010
######################################################################

## Debugging

ps_debug = debug_on_warning(1)

######################################################################
## System Parameters
######################################################################

global ps_states = 20;

## X-Axis

ps_x_low = 1900;
ps_x_high = 2050;

ps_x_step = 0.01;
[ps_x] = ps_x_low:ps_x_step:ps_x_high;

### Main Loop

for run = 1:3

######################################################################
## Peak definitions ("0 K"):
##
## Array: | Center: [meV]   |
##        | FWHM:   [meV]   |
##        | Type: X:1, XX:2 |
######################################################################

[ps_init_para_X] =  [1987.4,4E-1,1];

switch run
  case 1
```

```
    [ps_init_para_XX] = [1980.5,4E-1,2]; # 6.9 meV splitting
  case 2
    [ps_init_para_XX] = [1982.4,4E-1,2]; # 5 meV splitting
  case 3
    [ps_init_para_XX] = [1977.4,4E-1,2]; # 10 meV splitting
endswitch

ps_splitting = ps_init_para_X(1) - ps_init_para_XX(1);

## Ranges

ps_temp_step = 2.5;
[ps_temp] = 5:ps_temp_step:200;

for ps_fixpwr = 0.025:0.025:4
#for ps_fixpwr = 0.1:0.1:4

#######################################################################
## Filename parameter preparation:
#######################################################################


[ps_parameter] = ['_', num2str(ps_splitting),\
       'split_', num2str(ps_fixpwr,'%1.3f') ,\
       'lambda'];

[ps_parameterT] = ['_', num2str(ps_splitting),\
       'split_', num2str(ps_temp), '%1.2f K'];

[ps_parameterP] = ['_', num2str(ps_splitting),\
       'split_', num2str(ps_fixpwr,'%1.3f') ,\
       'lambda'];

[ps_parameterTP] = ['_', num2str(ps_splitting),\
       'split_', num2str(ps_fixpwr,'%1.3f') ,\
       'lambda_', num2str(ps_temp), '%1.2f K'];

#######################################################################
## Temperature dependent
#######################################################################

[ps_para_temp_X] = ps_Gen_Para_Temp(ps_init_para_X,
    [ps_temp],
    ps_fixpwr,
    ps_states
```

```
    );

[ps_para_temp_XX] = ps_Gen_Para_Temp(ps_init_para_XX,
     [ps_temp],
     ps_fixpwr,
     ps_states
     );

for i = 1:length(ps_temp)
    ps_intens_temp_zero(i) =  ps_Intensity(ps_temp(i),
   ps_fixpwr,
   0
   );
endfor

#######################################################################
## Generate Graphs:
#######################################################################

## Temperature dependent

for i = 1:length(ps_temp)

  ps_graph_temp_X(i,:) = ps_Lorentz(ps_para_temp_X(i,:),[ps_x]);
  ps_graph_temp_XX(i,:) = ps_Lorentz(ps_para_temp_XX(i,:),[ps_x]);

  ps_graph_prob_temp(i) = ps_Prob(ps_para_temp_XX(i,:)
  ,ps_para_temp_X(i,:)
  ,ps_temp(i),ps_fixpwr
  );

  ps_graph_prob_single_temp(i) = ps_Single_Prob(ps_para_temp_XX(i,:)
  ,ps_para_temp_X(i,:)
  ,ps_temp(i),ps_fixpwr
  );

endfor

#######################################################################
## Console Output
#######################################################################

## System Parameter

printf("\n#############################\n\
```

```
Splitting:\t%g meV\n\
Power:\t\t%g Lambda\n\
",ps_splitting,ps_fixpwr );
printf("############################\n")

######################################################################
## Plotting:
######################################################################

## 1D: FWHM

plot(ps_temp,ps_para_temp_X(:,3),"-2;FWHM of X;",
     ps_temp,ps_para_temp_XX(:,3),"-1;FWHM of XX;");
title("Linewidth vs. Temperature");
xlabel("Temperature (K)");
ylabel("Linewidth (meV)");
ps_Print('Linewidth_temp',ps_parameterP);
matrix = [ps_temp',ps_para_temp_X(:,3),ps_para_temp_XX(:,3)];
ps_Save('Linewidth_temp',ps_parameterP,matrix);


## 1D: Intensity

plot(ps_temp,ps_para_temp_X(:,2),"-2;X;",\
     ps_temp,ps_para_temp_XX(:,2),"-1;XX;",
     ps_temp,ps_intens_temp_zero,"3;Zero Photon Prob.;");
title("Intensity vs. Temperature");
xlabel("Temperature (K)");
ylabel("Intensity (Cts.)");
ps_Print('Intensity_temp',ps_parameterP);
matrix = [ps_temp',ps_para_temp_X(:,2),ps_para_temp_XX(:,2)];
ps_Save ('Intensity_temp',ps_parameterP,matrix);


## 1D: Redshift

plot(ps_temp,ps_para_temp_X(:,1),"-2;X;",\
     ps_temp,ps_para_temp_XX(:,1),"-1;XX;");
title("Redshift vs. Temperature");
xlabel("Temperature (K)");
ylabel("Energy (meV)");
ps_Print('Shift_temp',ps_parameterP);
matrix = [ps_temp',ps_para_temp_X(:,1),ps_para_temp_XX(:,1)];
ps_Save('Shift_temp',ps_parameterP,matrix);
```

```
## 1D: Probability

plot(ps_temp,ps_graph_prob_temp,"-1;Photon Emission;",
     ps_temp,ps_graph_prob_single_temp,"-2;Single Photon;",
     ps_temp,ps_intens_temp_zero,"3;Zero Photon Prob.;");
title(["Emission Probability vs. Temperature (Lambda: ",\
       num2str(ps_fixpwr),", Split: ",\
       num2str(ps_splitting)," meV)"]);
xlabel("Temperature (K)");
ylabel("Probability (per laser cycle)");
ps_Print('Prob_temp',ps_parameterP)
matrix = [ps_temp',ps_graph_prob_temp',ps_graph_prob_single_temp'];
ps_Save('Prob_temp',ps_parameterP,matrix);

endfor
endfor
```

Intensity Calculation

```
function Int = ps_Intensity (ps_temp,ps_pwr,ps_type)

  ## usage:  A = ps_Intensity (ps_temp,ps_pwr,ps_type)
  ##
  ## Calculate intensities within 6 ns after pulse
  ##
  ## Dark state correction a la PRB 90 257404
  ##
  ## Assuming: Gamma_L = 0 and etha_A = 1
  ##

  ## Parameters
  global ps_states;
  t_x  = 1200; # X lifetime [ps]
  t_fl = 600; # BS-DS OK spin flip time [ps]

  k_b = 0.086173422; # in meV
  E_Ph = 5; # BS <-> DS splitting [meV]

  TIME = 6000; # 6 [ns] Integration

  ## Arrhenius X/XX temp. dependence correction factor
  X_corr = ps_Quench(ps_temp,2);
  XX_corr = ps_Quench(ps_temp,1);
```

```
## p_x,p_xx,p_1 are poisson derived probabilities
p_0 = ps_Poisson(ps_pwr,0,0); # Poisson 0
p_1 = ps_Poisson(ps_pwr,1,1);  # Poisson 1
p_s = ps_Poisson(ps_pwr,2,ps_states); # Poisson Sum 2:ps_states

## excitation probabilities for X and XX
p_xx = XX_corr * p_s; # XX
p_x = X_corr * (p_1 + p_s); # X
p_Z = p_0 + (p_1 + p_s - p_x); # Zero

switch ps_type

  case {0,1}
    ## Probab. forX in BS and DS:  p_bs + p_ds = 1
    p_bs = (p_1 / 2 + p_s)/p_x; # X in BS

    ## for DS correction
    N_B = 1/(exp(E_Ph/(k_b*ps_temp))-1); # Phonon number
    t_s = 1 / (1/t_fl * (1 + 2*N_B)); # short decay time
    t_l = 1 / (1/t_x/2 - 1/t_x/2 \
          * tanh(E_Ph/(2*k_b*ps_temp))); # long decay time

    ## Normalized Integrated Intensity:
    int_c = ((1/t_x*N_B)/(1+2*N_B)) * t_l*(1 - exp(-TIME/t_l)) \
       + (1/t_x*(p_bs-N_B/(1+2*N_B))) * t_s*(1 - exp(-TIME/t_s));

endswitch

switch ps_type

case 0 # Zero Photon "intensity"  + dark excitons
    Int = p_Z + p_x * (1 - int_c);

  case 1 # X
    Int = p_x * int_c;

  case 2 # XX
    Int = p_xx;

  otherwise
    error("Unknown Peak type")

endswitch

##
```

```
  ## Temp depend.
  ##
  ## Intensity[A_, T_] := Module[{b = 28110.43401, Eph = 0.06905},
  ##   A/(1 + b*Exp[-Eph/(kB*T)])];
  ##

endfunction
```

List of Figures

2.1. Density of states for different dimensions. 25
2.2. Schematic shell structure of a QD. 26
2.3. Excitation scheme 28
2.4. Poisson distribution. 30
2.5. Bright and dark exciton spin configuration. 31
2.6. Biexciton spin configuration. 33
2.7. Phase-space portrait of the thermal state. 36
2.8. Phase-space portrait of the GLAUBER state. . . . 38
2.9. Phase-space portrait of the FOCK state. 39
2.10. Planar cavity luminescence. 42
2.11. POISSON-distribution probability for one and two electron–hole pairs (e–h pairs). 45
2.12. Dispersion relation of GaAs phonons. 47

3.1. Photo of the Aixtron 200 reactor. 56
3.2. Al dependence of the aluminum gallium indium phosphide (AlGaInP) band gap. 58
3.3. Al dependence of the AlGaInP phonon energies. . 59
3.4. Epitaxy map 60
3.5. Schematics of SK growth mode. 60
3.6. SEM image of micro pillars. 63
3.7. Photography of the He-flow cryostat. 66
3.8. Schematic µ-PL-setup. 67

3.9. Image and scheme of the Hanbury Brown and Twiss setup (HBT)-setup. 68

4.1. Schematic structure of the MP-sample. 72
4.2. Radius dependency of MPs-modes 74
4.3. Mode spectrum of a 2 µm diameter MP. 75
4.4. µ-PL-measurements on a MP 76
4.5. Temperature dependence of the intensity and emission energy of QD in a MP. 78
4.6. full-width at half-maximum (FWHM) and lifetime measurements on a QD in a MP. 79
4.7. Auto-correlation and on a single QD in a MP. . . . 80
4.8. Auto-correlation and on a single QD in a MP. . . . 81
4.9. Ensemble photoluminescence (PL)-measurement. . 84
4.10. Normalized EPD dependent µ-PL measurement at 4 K. 85
4.11. Power dependent intensity slopes of the X and XX. 86
4.12. Power and temp. dependent X and XX FWHM. . . 87
4.13. Temperature dependent µ-PL and decay time measurements. 88
4.14. SEM images of defects. 89
4.15. µ-PL-spectrum and auto-correlation measurement at 110 K. 89
4.16. Intensity map of and PL spectrum of a structured sample. 91
4.17. Height signal of an atomic-force microscope (AFM) scan on a site-controlled InP-islands sample. 92

5.1. Ensemble PL-measurement. 96
5.2. EPD dependent µ-PL measurement of a single QD. 97
5.3. Temp. dep. µ-PL spectra of a single QD. 98

5.4. ACO measurement at 4 K of a single QD luminescence line. 99
5.5. Ensemble PL-measurement. 100
5.6. EPD dependent spectra, intensity slopes and blue shift. 102
5.7. Temperature dependent µ-PL measurements on Si substrate with SL. 104
5.8. Temperature dependent FWHM of the X and XX. 105
5.9. Temperature dependent decay time measurements. 106
5.10. Excitation wavelength dependent X decay time measurements. 107
5.11. Auto-correlation histograms of the X. 108

6.1. Ensemble PL-measurement. 112
6.2. Power dependent µ-PL. 113
6.3. Double-logarithmic EPD dependent integrated peak and peak shoulder intensities. 114
6.4. Temperature dependent µ-PL spectra 115
6.5. Decay time measurements with exponential fits. . . 116
6.6. Auto-correlation measurement on the luminescence line in Fig. 6.4. 117

7.1. Ensemble PL-measurement. 120
7.2. EPD dependent µ-PL-spectra. 121
7.3. EPD dep. time resolved X intensity at 4 K under pulsed excitation. 122
7.4. Integrated intensity and FWHM over (inverse) temperature. 123
7.5. X decay times of the for diff. temps. 124
7.6. Normalized µ-PL-spectra of a single QD for diff. excit. wavelength. 125
7.7. Auto-correlation measurements on the X. 126

9.1. Scheme for the XX–X overlap simulation. 138
9.2. ROI-schemes. 141
9.3. PeakSim-FlowChart 142
9.4. Pulse sequence. 143
9.5. EPD and temp. dep. SPS efficiency. 145
9.6. EPD and temp. dep. SP-efficiency. 146
9.7. Temp. dep. SP-purity and efficiency for diff. ROIs 147
9.8. EPD and temp. dep. SPS efficiency. 148
9.9. EPD and temp. dep. SP-efficiency. 149
9.10. Temp. dep. of the SP-purity for diff. XX binding energies. 150

A.1. Screenshot of the *DotHunter* programm frontend. . 160
A.2. Screenshot of the *PeakFinder* programm frontend. 162

Glossary

CMOS A technology for constructing integrated circuits. Complementary metal oxide semiconductor (CMOS) technology is used in microprocessors, microcontrollers, static RAM, and other digital logic circuits. CMOS circuits use a combination of p-type and n-type metal–oxide–semiconductor field-effect transistors (MOSFETs) to implement logic gates and other digital circuits found in computers, telecommunications equipment, and signal processing equipment[3]. 1, 11, 53, 127, 150, 173

DH DotHunter, a µ-PL controlling program with features for scanning, tracking, and analyzing. 11, 81, 157

GNU Octave GNU Octave is a high-level interpreted language, primarily intended for numerical computations. It provides capabilities for the numerical solution of linear and nonlinear problems and for performing other numerical experiments. It also provides extensive graphics capabilities for data visualization and manipulation. Octave is normally used through its interactive command line interface, but it can also be used to write non-interactive programs. The Octave language is quite similar to Matlab, so that most programs are easily portable[4]. 135

[3] from http://en.wikipedia.org/wiki/CMOS

[4] from http://www.gnu.org/software/octave/

LabVIEW™ A graphical programming environment used by millions of engineers and scientists to develop sophisticated measurement, test, and control systems using intuitive graphical icons and wires that resemble a flowchart. It offers unrivaled integration with thousands of hardware devices and provides hundreds of built-in libraries for advanced analysis and data visualization – all for creating virtual instrumentation[5]. 157, 159, 174

PDC Parametric down-conversion: One Photon splits into two or more photons, while the total energy, momentum, and spin is conserved. 12

PF PeakFinder, a program for analyzing ccd camera spectra and transferring the data to the DotHunter program via TCP/IP. 12, 89

VI 'Virtual Instrument': A LabVIEW™ program or subprogram used to structure the program code. 13

[5] from http://www.ni.com/labview/whatis

Own Publications

[145] M. Wiesner, M. Bommer, W.-M. Schulz, M. Etter, J. Werner, M. Oehme, J. Schulze, M. Jetter, and P. Michler. Epitaxially Grown Indium Phosphide Quantum Dots on a Virtual Ge Substrate Realized on Si(001). *Applied Physics Express*, **5**, 042001 (March 2012).

[118] E. Koroknay, W.-M. Schulz, D. Richter, U. Rengstl, M. Reischle, M. Bommer, C. A. Kessler, R. Roßbach, H. Schweizer, M. Jetter, and P. Michler. Vertically stacked and laterally ordered InP and In(Ga)As quantum dots for quantum gate applications. *Physica Status Solidi (B)*, **249**, 737–746 (April 2012).

[43] M. Bommer, W.-M. Schulz, R. Roßbach, M. Jetter, P. Michler, T. Thomay, A. Leitenstorfer, and R. Bratschitsch. Triggered single-photon emission in the red spectral range from optically excited InP/(Al,Ga)InP quantum dots embedded in micropillars up to 100 K. *Journal of Applied Physics*, **110**, 063108 (September 2011).

[82] W.-M. Schulz, T. Thomay, M. Eichfelder, M. Bommer, M. Wiesner, R. Roßbach, M. Jetter, R. Bratschitsch, A. Leitenstorfer, and P. Michler. Optical properties of red emitting self-assembled InP/$(Al_{0.20}Ga_{0.80})_{0.51}In_{0.49}P$ quantum dot based micropillars. *Optics Express*, **18**, 12543 (May 2010).

[134] W.-M. Schulz, R. Roßbach, M. Reischle, G. Beirne, M. Bommer, M. Jetter, and P. Michler. Optical and structural properties of InP quantum dots embedded in $(Al_xGa_{1-x})_{0.51}In_{0.49}P$. *Physical Review B*, **79**, 35329 (January 2009).

[146] E. Koroknay, U. Rengstl, M. Bommer, M. Jetter, P. Michler. Site-controlled growth of InP/GaInP islands on periodic hole patterns in GaAs substrates produced by microsphere photolithography. *Journal of Crystal Growth*, **370**, 146–149 (May 2013).

Bibliography

[1] T. D. Ladd, F. Jelezko, R. Laflamme, Y. Nakamura, C. Monroe, J. L. O'Brien, *Nature* **464**, 45 (Mar. 2010).

[2] C. H. Bennett, F. Bessette, G. Brassard, L. Salvail, J. Smolin, *Journal of Cryptology* **5** (1992).

[3] R. Alléaume, F. Treussart, G. Messin, Y. Dumeige, J.-F. Roch, A. Beveratos, R. Brouri-Tualle, J.-P. Poizat, P. Grangier, *New Journal of Physics* **6**, 92 (July 2004).

[4] P. Michler, Ed., *Single Quantum Dots - Fundamentals, Applications and New Concepts*, (Springer-Verlag, Berlin, Heidelberg, New York, 2003).

[5] P. Michler, A. Kiraz, C. Becher, W. V. Schoenfeld, P. M. Petroff, L. Zhang, E. Hu, A. Imamoglu, *Science (New York, N.Y.)* **290**, 2282 (Dec. 2000).

[6] Z. Yuan, B. E. Kardynal, R. M. Stevenson, A. J. Shields, C. J. Lobo, K. Cooper, N. S. Beattie, D. a. Ritchie, M. Pepper, *Science (New York, N.Y.)* **295**, 102 (Jan. 2002).

[7] M. Oxborrow, A. Sinclair, *Contemporary Physics* **46**, 173 (May 2005).

[8] J. L. O'Brien, A. Furusawa, J. Vučković, *Nature Photonics* **3**, 687 (Dec. 2009).

[9] N. Gisin, R. Thew, *Nature Photonics* **1**, 165 (Mar. 2007).

[10] B. Lounis, M. Orrit, *Reports on Progress in Physics* **68**, 1129 (May 2005).

[11] C. Santori, D. Fattal, J. Vucković, G. S. Solomon, Y. Yamamoto, *Nature* **419**, 594 (Oct. 2002).

[12] T. Aichele, V. Zwiller, O. Benson, *New Journal of Physics* **6**, 90 (July 2004).

[13] N. Akopian, N. Lindner, E. Poem, Y. Berlatzky, J. Avron, D. Gershoni, B. Gerardot, P. Petroff, *Physical Review Letters* **96**, 7 (Apr. 2006).

[14] A. Dousse, J. Suffczyński, A. Beveratos, O. Krebs, A. Lemaître, I. Sagnes, J. Bloch, P. Voisin, P. Senellart, *Nature* **466**, 217 (July 2010).

[15] C. Santori, M. Pelton, G. Solomon, Y. Dale, Y. Yamamoto, *Physical Review Letters* **86**, 1502 (Feb. 2001).

[16] C. K. Hong, Z. Y. Ou, L. Mandel, *Physical Review Letters* **59**, 2044 (Nov. 1987).

[17] A. Musiał, G. Sek, A. Maryński, P. Podemski, J. Misiewicz, A. Löffler, *Acta Phys. Pol. A* **120**, 883 (2011).

[18] R. Hafenbrak, S. M. Ulrich, P. Michler, L. Wang, A. Rastelli, O. G. Schmidt, *New Journal of Physics* **9**, 315 (Sept. 2007).

[19] P. W. Shor, *SIAM Review* **41**, 303 (1999).

[20] N. Gisin, G. Ribordy, W. Tittel, H. Zbinden, *Reviews of Modern Physics* **74**, 145 (Mar. 2002).

[21] D. Bouwmeester, A. Ekert, A. Zeilinger, *The Physics of Quantum Information – Quantum Cryptography, Quantum Teleportation, Quantum Computation*, (Springer Berlin, 2000).

[22] C. H. Bennett, G. Brassard, *Proc. of the International Conference on Computers, Systems & Signal Processing, Bangalore (India)* **11**, 175 (1984).

[23] D. Stucki, M. Legré, F. Buntschu, B. Clausen, N. Felber, N. Gisin, L. Henzen, P. Junod, G. Litzistorf, P. Monbaron, L. Monat, J.-B. Page, D. Perroud, G. Ribordy, A. Rochas, S. Robyr, J. Tavares, R. Thew, P. Trinkler, S. Ventura, R. Voirol, N. Walenta, H. Zbinden, *New Journal of Physics* **13**, 123001 (Dec. 2011).

[24] Z. So, *Nature Letters* **431**, 1081 (2004).

[25] A. Politi, M. J. Cryan, J. G. Rarity, S. Yu, J. L. O'Brien, *Science (New York, N.Y.)* **320**, 646 (May 2008).

[26] Z. Mi, Y.-L. Chang, *Journal of Nanophotonics* **3**, 031602 (2009).

[27] M. Oehme, J. Werner, M. Jutzi, G. Wohl, E. Kasper, M. Berroth, *Thin Solid Films* **508**, 393 (June 2006).

[28] O. Thomas, Z. L. Yuan, J. F. Dynes, A. W. Sharpe, A. J. Shields. Efficient photon number detection with silicon avalanche photodiodes. http://arxiv.org/abs/1007.3570v1, (2010).

[29] K. Kuwabara, Y. Matsumoto, *Electronics and Communications in Japan (Part II: Electronics)* **87**, 10 (Dec. 2004).

[30] G. T. Reed, *Nature* **427** (2004).

[31] D. Miller, *Proceedings of the IEEE* **97**, 1166 (July 2009).

[32] D. Mathine, *IEEE Journal of Selected Topics in Quantum Electronics* **3**, 952 (June 1997).

[33] A. W. Fang, H. Park, O. Cohen, R. Jones, M. J. Paniccia, J. E. Bowers, *Optics Express* **14**, 9203 (Oct. 2006).

[34] A. L. Roest, M. A. Verheijen, O. Wunnicke, S. Serafin, H. Wondergem, E. P. A. M. Bakkers, *Nanotechnology* **17**, S271 (June 2006).

[35] M. Benyoucef, H. S. Lee, J. Gabel, T. W. Kim, H. L. Park, A. Rastelli, O. G. Schmidt, *Nano letters* **9**, 304 (Jan. 2009).

[36] D. Liang, J. E. Bowers, *Nature Photonics* **4**, 511 (July 2010).

[37] R. Chen, T.-t. D. Tran, K. W. Ng, W. S. Ko, L. C. Chuang, F. G. Sedgwick, C. Chang-Hasnain, *Nature Photonics* **5**, 170 (Feb. 2011).

[38] T. Wang, H. Liu, A. Lee, F. Pozzi, A. Seeds, *Optics Express* **19**, 11381 (May 2011).

[39] M. E. Groenert, C. W. Leitz, A. J. Pitera, V. Yang, H. Lee, R. J. Ram, E. a. Fitzgerald, *Journal of Applied Physics* **93**, 362 (2003).

[40] O. Kwon, J. J. Boeckl, M. L. Lee, A. J. Pitera, E. A. Fitzgerald, S. A. Ringel, *Journal of Applied Physics* **100**, 013103 (2006).

[41] V. Dixit, T. Ganguli, T. Sharma, R. Kumar, S. Porwal, V. Shukla, A. Ingale, P. Tiwari, A. Nath, *Journal of Crystal Growth* **293**, 5 (July 2006).

[42] Y.-k. Su, *Journal of Physics D: Applied Physics* **15**, 2325 (Nov. 1982).

[43] M. Bommer, W.-M. Schulz, R. Roßbach, M. Jetter, P. Michler, T. Thomay, A. Leitenstorfer, R. Bratschitsch, *Journal of Applied Physics* **110**, 063108 (2011).

[44] M. Reischle, G. J. Beirne, W.-M. Schulz, M. Eichfelder, R. Roßbach, M. Jetter, P. Michler, *Optics express* **16**, 12771 (Aug. 2008).

[45] K. Sebald, P. Michler, T. Passow, D. Hommel, G. Bacher, A. Forchel, *Applied Physics Letters* **81**, 2920 (2002).

[46] A. Tribu, G. Sallen, T. Aichele, R. André, J.-P. Poizat, C. Bougerol, S. Tatarenko, K. Kheng, *Nano letters* **8**, 4326 (Dec. 2008).

[47] R. Arians, T. Kümmell, G. Bacher, A. Gust, C. Kruse, D. Hommel, *Applied Physics Letters* **90**, 101114 (2007).

[48] O. Fedorych, C. Kruse, A. Ruban, D. Hommel, G. Bacher, T. Kümmell, *Applied Physics Letters* **100**, 061114 (2012).

[49] S. Kako, C. Santori, K. Hoshino, S. Götzinger, Y. Yamamoto, Y. Arakawa, *Nature materials* **5**, 887 (Nov. 2006).

[50] R. P. Mirin, *Applied Physics Letters* **84**, 1260 (2004).

[51] A. Polimeni, A. Patanè, M. Henini, L. Eaves, P. Main, *Physical Review B* **59**, 5064 (Feb. 1999).

[52] F. Bloch, *Zeitschrift für Physik* **52**, 555 (July 1929).

[53] C. Kittel, *Quantum Theory of Solids*, (John Wiley & Sons, 1987).

[54] N. N. Ledentsov, *Semiconductor Science and Technology* **26**, 014001 (Jan. 2011).

[55] T. Schwarzbäck, H. Kahle, M. Eichfelder, W.-M. Schulz, R. Roßbach, M. Jetter, P. Michler. Wavelength tunable red AlGaInP-VECSEL emitting at around 660 nm. In *Optik* (2011), pp. 79190B–79190B–10.

[56] M. Witzany, R. Roßbach, W.-M. Schulz, M. Jetter, P. Michler, T.-L. Liu, E. Hu, J. Wiersig, F. Jahnke, *Physical Review B* **83**, 1 (May 2011).

[57] V. Fock, *Zeitschrift für Physik* **47**, 446 (May 1928).

[58] I. Favero, G. Cassabois, C. Voisin, C. Delalande, P. Roussignol, R. Ferreira, C. Couteau, J. Poizat, J. Gérard, *Physical Review B* **71**, 3 (June 2005).

[59] A. Nazir, *Physical Review B* **78**, 153309 (Oct. 2008).

[60] R. Melet, V. Voliotis, a. Enderlin, D. Roditchev, X. Wang, T. Guillet, R. Grousson, *Physical Review B* **78**, 3 (Aug. 2008).

[61] W.-M. Schulz, Dissertation, Stuttgart, (2011).

[62] M. Reischle, *Quantum optical and electronic properties of InP/(Al,Ga)InP quantum dots in view of their potential in quantum information devices*, (Dr. Hut, Stuttgart, 2010).

[63] S. Lazić, R. Hey, P. V. Santos, *New Journal of Physics* **14**, 013005 (Jan. 2012).

[64] M. Bayer, G. Ortner, O. Stern, A. Kuther, A. Gorbunov, A. Forchel, P. Hawrylak, S. Fafard, K. Hinzer, T. Reinecke,

S. Walck, J. Reithmaier, F. Klopf, F. Schäfer, *Physical Review B* **65**, 195315 (May 2002).

[65] H. van Kesteren, E. Cosman, W. van der Poel, C. Foxon, *Physical Review B* **41**, 5283 (Mar. 1990).

[66] E. Poem, Y. Kodriano, C. Tradonsky, N. H. Lindner, B. D. Gerardot, P. M. Petroff, D. Gershoni, *Nature Physics* **6**, 993 (Nov. 2010).

[67] M. Reischle, G. Beirne, R. Roßbach, M. Jetter, P. Michler, *Physical Review Letters* **101**, 146402 (Oct. 2008).

[68] G. Sallen, A. Tribu, T. Aichele, R. André, L. Besombes, C. Bougerol-Chaillout, S. Tatarenko, K. Kheng, J.-P. Poizat. Dark exciton optical spectroscopy of a semiconducting quantum dot embedded in a nanowire. arXiv:0903.0497v1, (Mar. 2009).

[69] C. Santori, G. Solomon, M. Pelton, Y. Yamamoto, *Physical Review B* **65**, 2 (Feb. 2002).

[70] M. Wimmer, S. Nair, J. Shumway, *Physical Review B* **73**, 1 (Apr. 2006).

[71] G. Beirne, M. Reischle, R. Roßbach, W.-M. Schulz, M. Jetter, J. Seebeck, P. Gartner, C. Gies, F. Jahnke, P. Michler, *Physical Review B* **75**, 1 (May 2007).

[72] R. Glauber, *Physical Review* **131**, 2766 (Sept. 1963).

[73] J. R. Klauder, E. C. G. Sudarshan, *Fundamentals of Quantum Optics*, (Dover Publications, 1968).

[74] C. C. Gerry, P. L. Knight, *Introductory Quantum Optics*, (Cambridge University Press, 2005).

[75] R. Loudon, *The Quantum Theory of Light*, (Oxford Science Publications, 1983).

[76] M. O. Scully, M. S. Zubairy, *Quantum Optics*, (Cambridge University Press, 1997).

[77] A. Kiraz, S. Fälth, C. Becher, B. Gayral, W. Schoenfeld, P. Petroff, L. Zhang, E. Hu, A. Imamoğlu, *Physical Review B* **65**, 1 (Mar. 2002).

[78] A. J. Shields, R. M. Stevenson, R. M. Thompson, Z. Yuan, B. E. Kardynal. Generation of single photons using semiconductor quantum dots. in *Nano-Physics & Bio-Electronics: A New Odyssey*, T. Chakraborty, F. Peeters and and U. Sivan, Eds. Elsevier, (2002), ch. 4, pp. 111–146.

[79] C. J. R. Sheppard, *Pure and Applied Optics: Journal of the European Optical Society Part A* **4**, 665 (Sept. 1995).

[80] S. Reitzenstein, N. Gregersen, C. Kistner, M. Strauss, C. Schneider, L. Pan, T. R. Nielsen, S. Höfling, J. Mø rk, A. Forchel, *Applied Physics Letters* **94**, 61108 (2009).

[81] A. Löffler, J. P. Reithmaier, G. Sek, C. Hofmann, S. Reitzenstein, M. Kamp, A. Forchel, *Applied Physics Letters* **86**, 111105 (2005).

[82] W.-M. Schulz, T. Thomay, M. Eichfelder, M. Bommer, M. Wiesner, R. Roßbach, M. Jetter, R. Bratschitsch, A. Leitenstorfer, P. Michler, *Optics Express* **18**, 12543 (May 2010).

[83] A. M. Fox, *Optical Properties of Solids*, (Oxford University Press, 2001).

[84] E. del Valle, F. Laussy, *Physical Review A* **84**, 1 (Oct. 2011).

[85] E. Illes, S. Hughes, *Physical Review B* **81**, 1 (Mar. 2010).

[86] S. Reitzenstein, C. Hofmann, a. Löffler, a. Kubanek, J.-P. Reithmaier, M. Kamp, V. D. Kulakovskii, L. V. Keldysh, T. L. Reinecke, a. Forchel, *Physica Status Solidi (B)* **243**, 2224 (Aug. 2006).

[87] S. Weiler, A. Ulhaq, S. M. Ulrich, S. Reitzenstein, A. Löffler, A. Forchel, P. Michler, *Physica Status Solidi (B)* **248**, 867 (Apr. 2011).

[88] A. Ulhaq, S. Ates, S. Weiler, S. M. Ulrich, S. Reitzenstein, A. Löffler, S. Höfling, L. Worschech, A. Forchel, P. Michler, *Phys. Rev. B* **82**, 45307 (July 2010).

[89] S. Ates, S. M. Ulrich, a. Ulhaq, S. Reitzenstein, a. Löffler, S. Höfling, a. Forchel, P. Michler, *Nature Photonics* **3**, 724 (Nov. 2009).

[90] A. Imamoglu, *Optics and Photonics News* **13**, 22 (Aug. 2002).

[91] G. Sallen, A. Tribu, T. Aichele, R. André, L. Besombes, C. Bougerol, M. Richard, S. Tatarenko, K. Kheng, J.-P. Poizat, *Nature Photonics* **4**, 696 (July 2010).

[92] M. Abbarchi, T. Kuroda, T. Mano, K. Sakoda, C. Mastrandrea, A. Vinattieri, M. Gurioli, T. Tsuchiya, *Physical Review B* **82** (Nov. 2010).

[93] B. Szafran, F. M. Peeters, S. Bednarek. Stark effect on the exciton spectra of vertically coupled quantum dots: horizontal field orientation and non-aligned dots. aps.arxiv.org/list/cond-mat/0612253, (2006).

[94] M. Sabathil, S. Hackenbuchner, S. Birner, J. A. Majewski, P. Vogl, J. J. Finley, *phys. stat. sol. (c)* **0**, 1181 (2003).

[95] S.-S. Li, J.-B. Xia, *Journal of Applied Physics* **88**, 7171 (2000).

[96] C. Y. Jin, H. Y. Liu, S. Y. Zhang, Q. Jiang, S. L. Liew, M. Hopkinson, T. J. Badcock, E. Nabavi, D. J. Mowbray, *Applied Physics Letters* **91**, 021102 (2007).

[97] Y. Varshni, *Physica* **34**, 149 (May 1967).

[98] K. P. O'Donnell, X. Chen, *Applied Physics Letters* **58**, 2924 (1991).

[99] Landolt-Börnstein, *Numerical Data and Functional Relationships in Science and Technology, New Series Group III, Volume 41*, (Springer-Verlag, Berlin, Heidelberg, New York, 1998).

[100] R. Roßbach, Dissertation, Stuttgart, (2007).

[101] G. Wen, J. Lin, H. Jiang, Z. Chen, *Physical Review B* **52**, 5913 (Aug. 1995).

[102] G. Ortner, D. Yakovlev, M. Bayer, S. Rudin, T. Reinecke, S. Fafard, Z. Wasilewski, A. Forchel, *Physical Review B* **70**, 1 (Nov. 2004).

[103] A. Nowak, E. Gallardo, D. Sarkar, H. van der Meulen, J. Calleja, J. Ripalda, L. González, Y. González, *Physical Review B* **80**, 161305 (Oct. 2009).

[104] S. Arrhenius, *Zeitschrift fuer physikalische Chemie* **4**, 226 (1889).

[105] M. Wiesner, Disstertation, Stuttgart, (2012).

[106] T. Suzuki, A. Gomyo, S. Iijima, *Journal of Crystal Growth* **99**, 60 (Jan. 1990).

[107] J. Dong, S. J. Chua, Y.-J. Wang, H.-R. Yuan, *Journal of Crystal Growth* **269**, 408 (Sept. 2004).

[108] M. Kawabe, T. Ueda, *Japanese Journal of Applied Physics* **26**, L944 (June 1987).

[109] I. Vurgaftman, J. R. Meyer, L. R. Ram-Mohan, *Journal of Applied Physics* **89**, 5815 (2001).

[110] L. Francesio, P. Franzosi, M. Caldironi, L. Vitali, M. Dellagiovanna, A. DiPaola, F. Vidimari, S. Pellegrino, *Il Nuovo Cimento D* **18**, 975 (Aug. 1996).

[111] T. Hofmann, G. Leibiger, V. Gottschalch, I. Pietzonka, M. Schubert, *Physical Review B* **64**, 155206 (Sept. 2001).

[112] S. Bednarek, B. Szafran, K. Lis, J. Adamowski, *Physical Review B* **68** (Oct. 2003).

[113] I. N. Stranski, L. Krastanow, *Monatshefte für Chemie* **71**, 351 (Dec. 1937).

[114] H. Lohmeyer, J. Kalden, K. Sebald, C. Kruse, D. Hommel, J. Gutowski, *Applied Physics Letters* **92**, 011116 (2008).

[115] M. C. Petty, *Langmuir-Blodgett Films: An Introduction*, (Cambridge University Press, 1996).

[116] P. Atkinson, S. Kiravittaya, M. Benyoucef, a. Rastelli, O. G. Schmidt, *Applied Physics Letters* **93**, 101908 (2008).

[117] W. Wu, D. Dey, O. G. Memis, A. Katsnelson, H. Mohseni, *Nanoscale Research Letters* **3**, 123 (Mar. 2008).

[118] E. Koroknay, W.-M. Schulz, D. Richter, U. Rengstl, M. Reischle, M. Bommer, C. A. Kessler, R. Roßbach, H. Schweizer, M. Jetter, P. Michler, *Physica Status Solidi (B)* **249**, 737 (Apr. 2012).

[119] K. Pötschke, L. Müller-Kirsch, R. Heitz, R. Sellin, U. Pohl, D. Bimberg, N. Zakharov, P. Werner, *Physica E: Low-dimensional Systems and Nanostructures* **21**, 606 (Mar. 2004).

[120] R. Hanbury Brown, R. Q. Twiss, *Nature* **178**, 1447 (1956).

[121] A. Ulhaq, S. Ates, S. M. Ulrich, S. Reitzenstein, A. Löffler, A. Forchel, P. Michler, *Journal of Physics: Conference Series* **210**, 012058 (Feb. 2010).

[122] U. Hohenester, *Phys. Rev. B* **81**, 155303 (Apr. 2010).

[123] M. Kaniber, a. Neumann, a. Laucht, M. F. Huck, M. Bichler, M.-C. Amann, J. J. Finley, *New Journal of Physics* **11**, 013031 (Jan. 2009).

[124] S. Ates, S. M. Ulrich, A. Ulaq, S. Reitzenstein, A. Löffler, S. Höfing, F. Forchel, P. Michler, *Nature Photonics* **3**, 724 (2009).

[125] C. Schneider, T. Heindel, A. Huggenberger, P. Weinmann, C. Kistner, M. Kamp, S. Reitzenstein, S. Höfling, A. Forchel, *Applied Physics Letters* **94**, 111111 (2009).

[126] A. Badolato, M. Winger, K. Hennessy, E. Hu, A. Imamoglu, *Comptes Rendus Physique* **9**, 850 (Oct. 2008).

[127] A. Badolato, K. Hennessy, M. Atatüre, J. Dreiser, E. Hu, P. M. Petroff, A. Imamoglu, *Science (New York, N.Y.)* **308**, 1158 (May 2005).

[128] F. Laussy, E. del Valle, C. Tejedor, *Physical Review Letters* **101**, 83601 (Aug. 2008).

[129] J. Wiersig, N. Baer, P. Gartner, M. Benyoucef, S. M. Ulrich, P. Michler, A. Forchel, *OSA Trends in Optics and Photonics Series* **97**, 675 (2004).

[130] J. P. Reithmaier, G. Sek, A. Löffler, C. Hofmann, S. Kuhn, S. Reitzenstein, L. V. Keldysh, V. D. Kulakovskii, T. L. Reinecke, A. Forchel, *Nature* **432**, 197 (Nov. 2004).

[131] S. Ates, S. M. Ulrich, A. Ulhaq, S. Reitzenstein, A. Löffler, S. Höfling, A. Forchel, P. Michler, *Nature Photonics* **3**, 724 (Nov. 2009).

[132] F. Findeis, A. Zrenner, G. Böhm, G. Abstreiter, *Solid State Communications* **114**, 227 (Mar. 2000).

[133] P. Hawrylak, *Physical Review B* **60**, 5597 (Aug. 1999).

[134] W.-M. Schulz, R. Roßbach, M. Reischle, G. Beirne, M. Bommer, M. Jetter, P. Michler, *Physical Review B* **79**, 35329 (Jan. 2009).

[135] M. Bayer, A. Forchel, *Physical Review B* **65**, 1 (Jan. 2002).

[136] L. Besombes, K. Kheng, L. Marsal, H. Mariette, *Physical Review B* **63**, 155307 (Mar. 2001).

[137] A. Nowak, E. Gallardo, D. Sarkar, D. Sanvitto, H. van der Meulen, J. Calleja, J. Ripalda, L. González, Y. González,

Physica E: Low-dimensional Systems and Nanostructures **42**, 2509 (Sept. 2010).

[138] K. Zieger, *Heteroepitaxie von Halbleitern mit unterschiedlicher Gitterkonstante: Untersuchungen am Materialsystem GaAs/Si*, (Shaker Verlag, 1997).

[139] H. Tanoto, S. F. Yoon, K. L. Lew, W. K. Loke, C. Dohrman, E. A. Fitzgerald, L. J. Tang, *Applied Physics Letters* **95**, 141905 (2009).

[140] M. Oehme, J. Werner, O. Kirfel, E. Kasper, *Applied Surface Science* **254**, 6238 (July 2008).

[141] H. Döscher, T. Hannappel, B. Kunert, A. Beyer, K. Volz, W. Stolz, *Applied Physics Letters* **93**, 172110 (2008).

[142] H. Döscher, S. Brückner, A. Dobrich, C. Höhn, P. Kleinschmidt, T. Hannappel, *Journal of Crystal Growth* **315**, 10 (Jan. 2011).

[143] O. Labeau, P. Tamarat, B. Lounis, *Physical Review Letters* **90**, 257404 (June 2003).

[144] F.-G. Deng, G. L. Long, *Physical Review A* **70** (July 2004).

[145] M. Wiesner, M. Bommer, W.-M. Schulz, M. Etter, J. Werner, M. Oehme, J. Schulze, M. Jetter, P. Michler, *Applied Physics Express* **5**, 042001 (Mar. 2012).

[146] E. Koroknay, U. Rengstl, M. Bommer, M. Jetter, P. Michler, *Journal of Crystal Growth* **370**, 146 (May 2013).